UCLA
UCLA Electronic Theses and Dissertations

Title

Calcium Imaging of Cortical and Hippocampal Neurons During Learning and Decision Making

Permalink

Author

Blair, Garrett James

Publication Date

2021

Peer reviewed|Thesis/dissertation

UNIVERSITY OF CALIFORNIA

Los Angeles

Calcium Imaging of Cortical and Hippocampal Neurons during Learning and
Decision Making

A dissertation submitted in partial
satisfaction of the requirements for the degree
Doctor of Philosophy in Psychology

by

Garrett James Blair

2021

ABSTRACT OF DISSERTATION

Calcium Imaging of Cortical and Hippocampal Neurons
during Learning and Decision Making

by

Garrett James Blair
Doctor of Philosophy in Psychology
University of California, Los Angeles, 2021
Professor Hugh T. Blair, Chair

Studies of the neural basis of memory and decision making have utilized rats as a model organism for decades. Place cells in the hippocampus were first described fifty years ago, and our understanding of the cellular mechanisms of episodic memory and spatial navigation have been primarily based on the rat as a model organism. Modern calcium imaging techniques now allow researchers to monitor hundreds of cells simultaneously, and this has been a boon to brain research. However, until my first publication, calcium imaging in the freely behaving rat had not been demonstrated, and emerging research using calcium imaging in the mouse hippocampus conflicted with decades of rat literature. An intellectual gap was widening, and it was unclear whether differing results stemmed from differences in species or methodology. Therefore, we sought to apply calcium imaging to the rat to demonstrate its feasibility and utility. The research presented in this dissertation is a demonstration of both my efforts developing rat calcium imaging within the Miniscope open-science project, as well as applying these methods to specific hypotheses. Chapter 2 details our most recent experiment, studying the effect of aversive learning on hippocampal place cells and the role of cholinergic signaling. Chapter 3 summarizes collaborative work on the technical development and imaging capabilities of the Large Field of View miniature microscope utilized in the previous chapter. Chapter 4 presents my first co-authored publication where we demonstrated the first usage of single photon calcium imaging in the freely behaving rat, studying how cortical neurons reflect choice utility during effortful decision making.

The dissertation of Garrett Blair is approved.

Michael Fanselow

Peyman Golshani

Alicia Izquierdo

Andrew Wikenheiser

Hugh T. Blair, Committee Chair

DEDICATION

This dissertation is dedicated to my friends, family, and mentors who have helped and

guided me throughout life, as well as the rats who gave their lives so that we may better

understand our universe.

TABLE OF CONTENTS

List of Figures

List of Tables

ACKNOWLEDGEMENTS

BIOGRAPHICAL SKETCH

NAME: Garrett Blair
POSITION TITLE: Graduate student (PhD)
EDUCATION/TRAINING

INSTITUTION AND LOCATION	DEGREE (if applicable)	Start Date MM/YYYY	Completion Date MM/YYYY	FIELD OF STUDY
University of California, Irvine, CA	BS	09/2011	06/2015	Cognitive Science
University of California, Irvine, CA	BA	09/2011	06/2015	Spanish Literature
University of California, Los Angeles, CA	MA	09/2015	03/2017	Psychology
University of California, Los Angeles, CA	PhD	09/2015	In Progress	Psychology

A. Personal Statement

My senior year at UC Irvine, I took a course on the neurobiology of learning and memory, which focused on brain circuits underlying the formation of memories. The methods and experiments presented in this course taught me how much can be learned from animal models and research, and although I had no experience with this particular domain, I knew that I wanted to pursue research in this field. During my time at UCLA as a graduate student, I have acquired a wide variety of neuroscience research skills thanks to my amazing mentor, Tad Blair. Calcium imaging has been the main focus of my work, and with this skill I have been able to collaborate with labs across the campus and the country. The miniscope research consortium at UCLA is advancing an open-science model and helping labs worldwide, and I am proud to have made my own contributions to that cause. Hopefully you'll find my work as interesting and cool as I have.

B. Positions and Honors

ACTIVITY/ OCCUPATION	BEGINNING DATE (mm/yyyy)	ENDING DATE (mm/yyyy)	FIELD	INSTITUTION/ COMPANY	SUPERVISOR/ EMPLOYER
Undergraduate Research Assistant	06/2013	06/2015	Cognitive science	UC Irvine	Dr. Charles Wright
Undergraduate Research Assistant	01/2014	01/2015	Cognitive neuroscience	UC Irvine	Dr. Michael D'Zmura
Graduate researcher	09/2015	current	Behavioral neuroscience	UCLA	Dr. Hugh T. Blair

Academic and Professional Honors

2011-2015	University of California, Irvine Dean's Honor List
2011-2015	University of California, Irvine Campuswide Honors Program
2015	Undergraduate Research Opportunities Program fellowship
2015	Cognitive Science (BS) Magna Cum Laude
2015	Spanish Literature and Culture (BA) Cum Laude
2015	UCLA Alumni Fellowship
2016	UCLA Graduate Research Summer Mentorship award

Memberships and Professional Activities

Vision Science Society (2015)
Society for Neuroscience (2016-current)

C. Contributions to Science - Graduate Research

My interest concerning brain-computer interface capabilities that I became familiar with in Dr. D'Zmura's lab led me to an interest in animal neuroscience labs for my doctoral work. I began my research in Dr. Hugh Blair's lab with this shared interest, and learned the intricacies of electrophysiological studies in the rodent hippocampus. Under Dr. Blair's guidance I learned so much more than I could ever forget about the brain. During my second year in his lab, we sought to address the literature gap that had began to arise between rat ephys studies and mouse calcium imaging, and I worked to adopt this novel imaging method to rats while working with Dr. Peyman Golshani. This methodological development led to multiple presentations at the Society for Neuroscience conferences (see below). I was also able to assist the UCLA miniscope project by sharing our methods and procedures for translating calcium imaging to rats. I've led workshops at UCLA and Johns Hopkins University (Knierim lab) through this work, and taught imaging methods to both the Izquierdo and Adhikari labs at UCLA which have led to collaborative publications with both. My first co-authored paper (Hart, Blair et al. J. Neuro 2020) was the first paper to demonstrate single-photon calcium imaging in freely behaving rats.

G.J. Blair[*], E.E. Hart[*], T.J. O'Dell, H.T. Blair, A. Izquierdo. *Chemogenetic modulation and single-photon calcium imaging in anterior cingulate cortex reveal a mechanism for effort-based decisions*. Journal of Neuroscience, 15 July 2020, 40 (29) 5628-5643; DOI: https://doi.org/10.1523/JNEUROSCI.2548-19.2020

P.J. Schuette, F.M.C.V. Reis, S.M. Pereira, M.H. Chakerian, A. Torossian, **G.J. Blair**, W. Wang, H.T. Blair, J.C. Kao, A. Adhikari. *Long-term characterization of hippocampal remapping during contextual fear acquisition and extinction*. Journal of Neuroscience, 21 October 2020, 40 (43) 8329-8342; DOI: https://doi.org/10.1523/JNEUROSCI.1022-20.2020

Z. Chen, **G.J. Blair**, H.T. Blair, J. Cong. *CANSEE: Customized Accelerator for Neural Signal Enhancement and Extraction from the Calcium Image in Real Time*. FPGA 2020: 318; DOI: https://doi.org/10.1145/3373087.3375358

Z. Chen, **G.J. Blair**, H.T. Blair, J. Cong. *BLINK: bit-sparse LSTM inference kernel enabling efficient calcium trace extraction for neurofeedback devices*. ISLPED 2020: 217-222; DOI: https://doi.org/10.1145/3370748.3406552

G.J. Blair, , A.G. Howe, P. Golshani, & H.T. Blair (2018) *Long-term population recordings of hippocampal place cells via Ca^{2+} imaging in the rat*. UCI Learning and Memory 2018 conference.
G.J. Blair, A.G. Howe, D. Aharoni, S. Flores, T. Shuman, P. Golshani, & H.T. Blair (2016) Calcium Imaging of Hippocampal Cell Activity in Behaving Rats. Neuroscience 2016 Annual Meeting.

CHAPTER 1: Background and Introduction

1.1 INTRODUCTION

The experiments and data presented in this dissertation were designed to investigate the neural basis of learning, memory, and decision making by performing in-vivo calcium imaging experiments in freely behaving rats. The experiments were done using an implantable microendoscope device (the UCLA miniscope) to perform cellular resolution imaging of neural population activity. When I first adopted this technique for my experiments in 2015, endoscopic in-vivo calcium imaging was still a new technology. Several published studies had reported findings from endoscopic imaging studies in freely behaving mice, but such experiments had never been done in behaving rats. So, before carrying out my experiments, it was first necessary to adapt the endoscopic imaging methodology for rats. Consequently, a major objective of this dissertation work was to apply an existing technique to a novel animal model in which it had not previously been used. I had valuable assistance in these technology development efforts from other UCLA investigators, including Peyman Golshani, Daniel Aharoni, and Alcino Silva, who were leaders of the original team that initially created the UCLA miniscope. The technology that I have developed to carry out my thesis project has not only allowed me to pursue my own scientific hypothesis, but it has also been disseminated more broadly to enable other researchers to apply these techniques in their own research.

In this introductory chapter, I shall first provide some background on the use of calcium imaging technology to study the neural basis of behavior (section 1.2). I will then introduce the scientific questions that laid the foundations for my thesis experiments investigating how neural activity in the hippocampus contributes to learning and memory (section 1.3), and how neural activity in the frontal cortex regulates decision making (section 1.4).

1.2 IN-VIVO CALCIUM IMAGING

Cellular-level optical imaging remains a relatively new method for recording neural activity. This technique involves introducing an indicator dye into neurons that causes them to fluoresce when they are active, but not when they are quiescent. Voltage-sensitive fluorescence indicators change their brightness as a function of the cell's membrane voltage, whereas calcium fluorescence indicators change brightness as a function of the cell's intracellular calcium concentration. Early pioneering experimenters injected indicator dyes into cells and then recorded optical responses using fluorescence microscopes or photodiode arrays. Using such methods, it was possible to reveal large neural circuit features in the brain, such as topographic somatosensory maps in rat barrel cortex (Orbach, Cohen, and Grinvald 1985) and orientation selective globs that tile the visual space in cats (Bonhoeffer and Grinvald 1991). Today, modern optical imaging experiments rely upon genetically encoded indicators that are transfected into targeted cell populations. For example, genetically encoded calcium indicators (GECIs) such as GCaMP consist of a green fluorescent protein (GFP, derived from the jellyfish Aequorea) conjugated with the calcium-binding protein calmodulin (Miyawaki et al. 1997; T.-W. Chen et al. 2013; Dana et al. 2019). (Figure 1.2) A neuron expressing GCaMP will emit green photons when stimulated by blue light; this fluorescence becomes significantly enhanced when the intracellular calcium concentration increases after the cell fires an action potential. Hence, calcium fluorescence provides an indirect way to measure spiking activity in neurons.
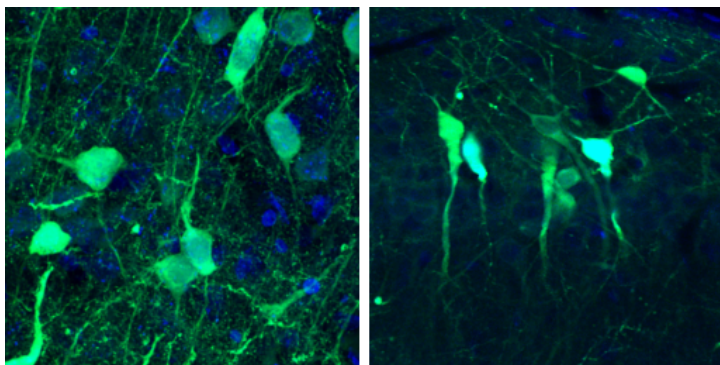
Figure 1.2. Example histology slice of neurons expressing GCaMP (green) in the cortex (left) and hippocampal CA1 (right). Neurons are stained with DAPI (blue) to highlight nuclei. During calcium imaging experiments, these cells fluoresce green when the neuron fires action potentials. Images taken at 63x and 20x, respectively.

1.2.1 Calcium imaging versus electrophysiology

For any method of observing neural activity, there are trade-offs between temporal and spatial resolution that must be taken into account. Prior to the advent of calcium imaging technology, electrophysiological recording was the dominant method for recording single unit activity of neurons. Compared with electrophysiology methods, calcium imaging has several advantages but also some disadvantages.

1.2.1.1 Population size

One major benefit of in-vivo calcium imaging is that it provides single-cell spatial resolution (1-5 microns) to simultaneously observe neural activity within a large volume of tissue ranging from 0.5 mm^3 (e.g., imaging hundreds of cells with low-resolution single-photon methods) to as much as 5 mm^3 (e.g., imaging thousands of cells with the highest resolution two-photon methods). By contrast, in-vivo electrophysiological recording methods are limited to recording from a few dozen (e.g., using small tetrode bundles) up to several hundred (e.g., using silicon probe arrays) neurons at the same time, from bands or sheets of tissue that lie along the path of implanted electrode shanks. This significant increase in population size allows researchers to understand how neurons coordinate across a network rather than in isolation.

1.2.1.2 Longitudinal recordings

Another benefit of in-vivo calcium imaging is that the imaging plane is nearly identical during every experimental session, and this makes it possible to perform longitudinal studies where the same neural cells and populations can be recorded across many days, so that the activity of individual cells and populations can be compared over weeks or even months (Ziv et al. 2013; Cai et al. 2016; Gonzalez et al. 2019). By contrast, it is very difficult for in-vivo

electrophysiology probes to record the same neurons from one session to the next, because even the slightest movement of the probes between sessions (by a few microns) can dramatically change the signal waveforms, making it impossible to tell whether a cell recorded from a probe on one is the same as a cell recorded from that same probe on another day. The ability to probe cellular activity within the same large neuronal population across long timescales with calcium imaging has led to a number if important discoveries that would not have been possible using electrophysiological methods (Grewe et al. 2017; Gründemann et al. 2019; Kondo et al. 2018; Mau et al. 2018; Kinsky et al. 2018; Kinsky et al. 2020; Shuman et al. 2020).

1.2.1.3 Temporal resolution

Calcium imaging is not without its downsides of course. Most electrophysiological recording methods have a sub-millisecond time resolution (sample rates in the thousands of Hertz are common), whereas most calcium imaging methods have considerably lower time resolution (sample rates in the tens of milliseconds, or 20-60 Hz, are common). There are two main reasons for this. First, calcium fluorescence is a chemical process that takes place on a timescale that is inherently slower than action potential generation. When a neuron spikes and calcium channels open, calcium must diffuse through the cytoplasm before it reaches and binds to GCaMP molecules on a timescale of a few milliseconds (exact binding rates differ among indicators but are typically in the range of 10 ms or less). Once calcium is bound, GCaMP will continue to fluoresce until calcium unbinds, which occurs on a time scale of tens to hundreds of milliseconds (again, depending upon the indicator). The rate of GCaMP unbinding is typically an order of magnitude or more greater then the rate of binding, so it is possible for GCaMP to become saturated with calcium during periods of high activity, and this can reduce sensitivity.

1.2.2 Two-photon versus one-photon methods

A primary distinction among calcium imaging methods is between two- and single-photon experiments. This refers to the necessary excitation energy for the fluorophore to emit a photon, and to the physics of light delivery and detection.

Single-photon imaging experiments rely upon simple traditional methods of fluorescence microscopy. Consider a calcium indicator that absorbs blue light with wavelengths around 450-495 nanometers, and emits green light with wavelengths around 515 nm (Dana et al. 2019). A light source is needed to provide the blue excitation photons, and in a one-photon experiment, this can be provided by a simple light emitting diode (LED) with a blue emission filter of the appropriate wavelength. The light source can stimulate the entire field of view during imaging, which does not require a high degree of precision. A simple CMOS camera sensor, focusing mechanism, and green emission filter set are all that is then required to detect the fluorophore and construct a working single-photon microscope (Ghosh et al. 2011; Cai et al. 2016). Using modern miniaturized optics and electronics, a single photon microscope can be made so small that it can be worn on the head of a freely behaving animal as small as a mouse (Ghosh et al. 2011; Ziv et al. 2013; Mau et al. 2018; Kinsky et al. 2018). For my thesis experiments, I used the UCLA miniscope (Cai et al. 2016; Shuman et al. 2020), an open-source miniaturized microscope for single photon imaging in freely behaving animals.
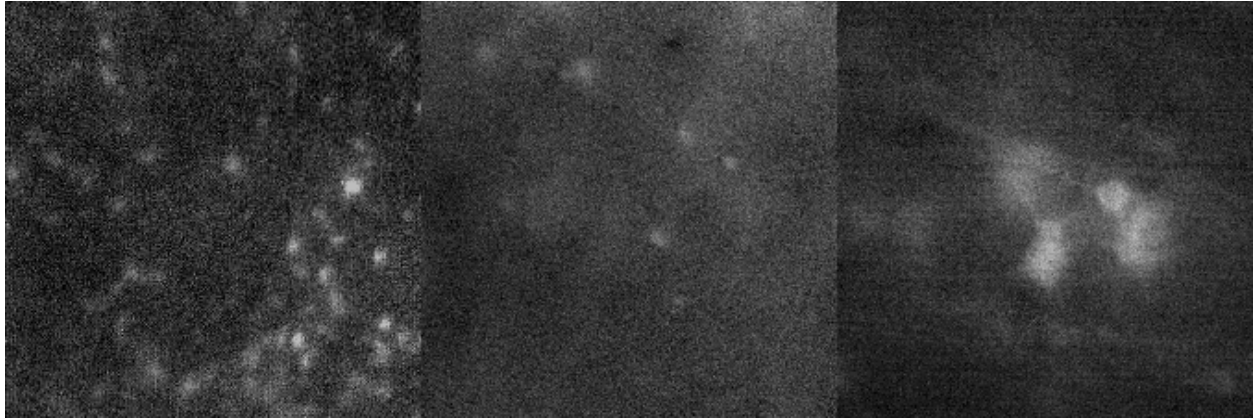
Figure 1.2.1.1. Example single-photon calcium imaging recording. Recordings of rat CA1 (left), mouse cortex (center), and rat Anterior Cingulate Cortex (right) performed for data reported in Chapters 2, 3, and 4 respectively. Recordings have been motion corrected, background subtracted, and sped up for visualization.

Although single-photon imaging is relatively simple compared to two-photon imaging, it also suffers from limitations. For example, excitation photons are easily scattered and do not penetrate deeply into the tissue, so it is difficult to image below the surface of thick tissue samples. Because the entire field of view is illuminated, single-photon imaging also suffers from large background fluorescence caused by neurons outside of the focal plane.

Two-photon imaging circumvents these issues by using a laser scanning microscope to deliver pairs of interfering photons to a single point in the field of view (Stosiek et al. 2003; Dana et al. 2019). Interference between coincident photons results in excitation at half the wavelength of the individual photons. Hence, if a blue excitation wavelength is desired for a green indicator, then each individual photon is delivered at twice the desired excitation wavelength (e.g., in the infrared range of 800-930 nm). The depth of optical excitation is greatly increased by using focused, higher energy photons instead of diffuse, lower energy photons. This results in less tissue scattering, and also yields a much clearer imaging by minimizing out of focus excitations. However, this technique necessitates very precise delivery of photon pairs at a fast rate over a wide area. Typical two-photon scanning laser microscopes operate at 80-MHz with <100 femtosecond pulse widths to achieve this. Two-photon microscopy can yield highly detailed subcellular resolution images of somatic (Dombeck et al. 2010; Dalmay et al. 2019), dendritic

(Svoboda et al. 1997; Zong et al. 2017), and synaptic bouton activity (Grutzendler and Gan 2006; Bass et al. 2017). However, two photon microscopes are bulky and expensive, and because they are so large, they cannot easily be worn on the head. Most two-photon imaging experiments are done on head-fixed animals, which limits the range of behaviors that can be studied and hypotheses that can be addressed by two-photon imaging. Some studies have demonstrated feasibility of unrestrained two-photon imaging in behaving animals (Helmchen et al. 2001; Zong et al. 2017; Ozbay et al. 2018) but such devices are still not widely available.
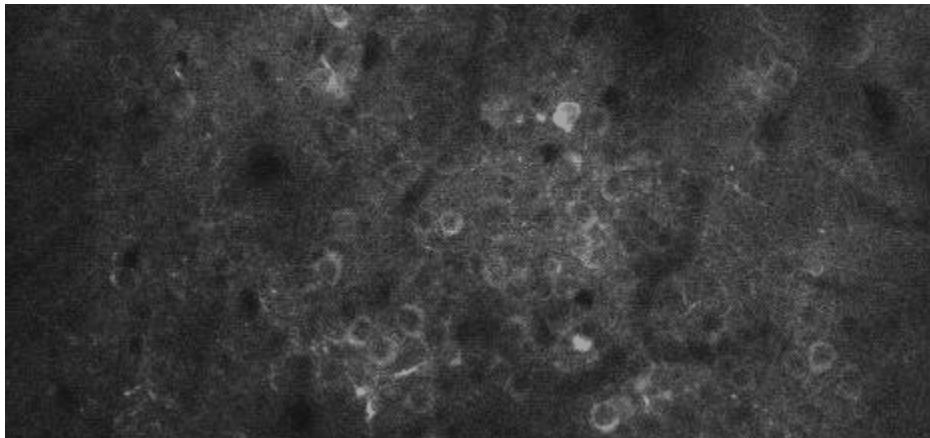
Figure 1.2.2.2. Example two-photon imaging recording courtesy of Dr. Megha Seghal, with the help of Dr. Josha Trachtenberg. Layer 2-3 neurons in the mouse retrosplenial cortex expressing GCaMP under a head-fixed cranial window.

1.2.3 Imaging in different species

In-vivo calcium imaging can image almost the entire nervous system of animals with sufficiently small brains, such as C. elegans (Tian et al. 2009), fruit flies (J. W. Wang et al. 2003), and zebrafish (Muto et al. 2011). In larger animals such as mice, it is not possible to image the whole nervous system but it is possible to simultaneously image up to tens of thousands of neurons with two-photon methods, and thousands with single photon methods (Ziv et al. 2013; Cai et al. 2016; Aharoni and Hoogland 2019). Mice also have the advantage that a wide range of mutants and genetic tools are available to facilitate genetic targeting of calcium

indicators to specific cell populations (Q. Chen et al. 2012). But the disadvantage of working with mice is that for some questions, it is harder to make comparisons with prior data from the electrophysiological recording literature. For example, a major goal of my thesis work was to perform calcium imaging of place cells in the hippocampus of rats. Electrophysiological studies of place cells have been conducted for decades, primarily in rats. To compare my findings with this existing rat literature, I decided to do my calcium imaging experiments in rats rather than mice. But in-vivo calcium imaging studies had not yet been published with freely behaving rats at the time I started my experiments (until our first publication *Hart, Blair et al. 2020*, Chapter 4), so I had to develop some of the necessary methods, as described in Chapter 3.

1.3 EPISODIC MEMORY AND THE HIPPOCAMPUS

Memory is an integral part of our daily experience. Humans constantly utilize previous experiences to guide our future behavior. Interest and philosophical ponderings of memory have been present since Aristotle (c. 300 B.C.), who described in *De Memoria et Reminiscentia* the first distinction between two different types of memory: the "Affection of Conception'' and "Affection of Perception" (Herrmann 1982). This distinction between concepts and percepts still exists in modern memory research today, known as semantic and episodic memories (Tulving 1972; Squire 1986). However, while memory has been a subject of philosophical interest for centuries, it wasn't until the 20th century that psychologists and neuroscientists began to understand the biological basis of memory at the level of circuits, cells, and synapses.

1.3.1 Early Beginnings

The first known reference to the hippocampus (from the Greek hippos ["horse"] and kampos ["sea monster"]) appeared in Julius Caesar Aratius' 1578 book of surgical anatomy, *De*

Humano Foetu Liber (Alex 1893; Bir et al. 2015). Three centuries later, Camillo Golgi developed a staining method which allowed for incredibly detailed descriptions of cellular architecture when applied to thin tissue sections and viewed under a light microscope. Santiago Ramón y Cajal applied this technique to image brain tissue, including the hippocampus, and famously illustrated his findings. These provided an outstanding level of detail about how brain regions are constructed from interconnected neurons, establishing the neuron as the unitary functional cell of the brain, and yielding Ramón y Cajal and Golgi to the 1906 Nobel prize in medicine (despite their intense rivalry).

In the 1950s, patient Henry Molaison (H.M.) underwent surgical removal of brain tissue in the medial temporal lobe (including the hippocampus) to ameliorate severe epileptic seizures. Although his seizures were cured by this treatment, Molaison suffered a profound memory impairment after his surgery (Scoville and Milner 1957). Studies of H.M. revealed that his remote memories (i.e. childhood memories, the neighborhood he grew up in, etc.) were intact, but his more recent episodic and semantic memories were impaired in a temporally graded fashion (with the most recent memories prior to surgery being the most severed impaired), and he now lacked the ability to create new episodic memories of events that occurred after surgery. He could not remember the doctors who he met with every day, and easily forgot recently given information if he was distracted. H.M. did maintain the ability to learn procedural memories and motor skills, such as learning to copy an image when looking through a mirror (N. J. Cohen and Squire 1980). This initial research implicated the hippocampus and medial temporal lobe in the formation and consolidation of episodic memories (Squire, Stark, and Clark 2004), and was followed by decades of research on the hippocampus and memory which continues to this day.

1.3.2 Evidence from rodent models

Spurred by evidence from human lesion patients, researchers began using animal models including rodents, rabbits, and primates to investigate the role of the hippocampus in memory. Here, I will focus on reviewing major findings from the rodent literature, since my thesis experiments were conducted using rats.

1.3.2.1 Lesion and inactivation studies

Many studies have relied upon selective hippocampal ablations using aspiration (Schmaltz and Theios 1972), electrolytic (Winocur, Rawlins, and Gray 1987), or excitotoxic (Winocur, Rawlins, and Gray 1987; J. Kim and Fanselow 1992) lesion methods . One early animal model for learning and memory studies was eye-blink conditioning in rabbits (Fanselow and Wassum 2016), a form of Pavlovian conditioning where a conditioned stimulus (CS), typically a light or tone, is presented just before an unconditioned stimulus (UR), typically a shock or air puff to the eye. Animals learn to respond to the CS by blinking (the conditioned response, or CR) in anticipation of the US. When the US begins before the CS terminates ("delay conditioning"), the hippocampus isn't required for learning (Oakley and Russell 1972). However, when there is a time delay between the offset of the CS and onset of the US ("trace conditioning"), the hippocampus becomes necessary (Moyer, Deyo, and Disterhoft 1990; Weiss and Disterhoft 2015). This suggests that the hippocampus may play a role in maintaining a memory of the prior CS occurrence throughout the trace period. CS-evoked spike responses emerge within the CA1 pyramidal layer during learning of the CS-US association (Berger, Alger, and Thompson 1976), and this neural activity may support the role of the hippocampus in trace conditioning. Similarly, in a novel object recognition task, where an object within an environment is replaced by a novel one, the hippocampus appears necessary only when a sufficient delay is imposed between the sample and test sessions (S. J. Cohen and Stackman 2015).

The hippocampus has also been shown to be necessary in more complex memory tasks as well. The Morris water maze is a spatial learning task where the rat learns to find a hidden platform in a pool of opaque water (Morris et al. 1982). Rats are placed in the pool and swim until they find the hidden platform, where they can sit and rest. Rats use external room cues in order to orient themselves within the environment and learn where the platform is located, and hippocampal lesions severely reduce their ability to learn the platform location. If the rat can see the platform, hippocampal lesions do not interfere with learning or performance. This spatial learning role of the hippocampus has been demonstrated in many tasks, such as the cheeseboard maze (Dupret et al. 2010), the radial arm maze (McDonald and White 2013), spatial alternation tasks with imposed delays (Zhang et al. 2021), etc. Therefore it seems that the hippocampus provides a mechanism for binding distinct sensory stimuli into a cohesive relational structure in space (a "context"), and maintains this structure even in the absence of the stimuli.

The behavioral paradigm of contextual fear conditioning (CFC) has become a popular rodent model for studying the role of the hippocampus in memory. This form of learning depends upon the hippocampus, and recapitulates key features of human hippocampal amnesia, such as the retrograde gradient (J. Kim and Fanselow 1992). In a typical CFC experiment, a rat or mouse is exposed to two contexts with saliently different stimuli (wall color, shape, sounds, smells) and given a few minutes to explore each. Then they are given unsignaled shocks in only one context. Subjects will freeze upon re-exposure to the shock context, yet they will freeze much less in the non-shocked context (assuming it is sufficiently distinct from the shocked context), showing that the animal remembers being shocked in one context and not the other. Inactivating the dorsal hippocampus (during either the shock conditioning or the retrieval session) impairs CFC but not fear conditioning to a tone (Anagnostaras et al. 1999). Presumably, this is because forming a memory of a familiar context (but not of a tone) requires

11

the hippocampus. Supporting this interpretation, pre-exposure to the context is also necessary

for CFC, since giving the shock within the first minute of introduction to a novel context will yield

greatly reduced freezing in the retrieval session, known as the immediate shock deficit (Wiltgen

et al. 2001). Consistent with this finding, the hippocampus takes about a minute to form stable

"place cells" (see section 1.3.2.2) when a rat is first introduced into an environment (Hill 1978;

Wilson and McNaughton 1993; Frank, Stanley, and Brown 2004), and this may correspond to

the time it takes to form a stable memory representation of the context. Recent optogenetic

studies have demonstrated that activity within the dentate gyrus of the hippocampus is both

necessary and sufficient for contextual fear learning (Liu et al. 2012; Ramirez et al. 2013;

Redondo et al. 2014).

1.3.2.2 Electrophysiological recording studies

It wasn't until the 1970's that the first recordings of neurons within the hippocampus of a

behaving animal were feasible. Initial studies reported pyramidal cells within the dorsal

hippocampus had spatially modulated firing fields, meaning these cells would fire action

potentials when the animal was moving through a specific location within an environment, thus

earning them the name "place cells" (J. O'Keefe and Dostrovsky 1971; John O'Keefe 1976).

Different place cells fire in different locations, apparently uniformly distributed throughout a

context, and will change their preferred firing locations when the animal is placed in a different

context (S. Leutgeb et al. 2005; J. K. Leutgeb et al. 2005) or when there is a dramatic valence

change within the same environment (Moita et al. 2004; Moita et al. 2003; M. E. Wang et al.

2015) Due to this context specific code, it is believed that this hippocampal place cell population

represents a cognitive map (John O'Keefe and Nadel 1978), an earlier theory of learning and

memory developed by Edward Tolman (Tolman 1948).

In Tolman's experiments during the 1930's and 1940's (summarized in his book

Cognitive maps in Rats and Men, 1948), his lab utilized a wide variety of complex mazes and

tasks for studying what strategies rats use to solve problems. Among the many was one dubbed the sun burst maze. Rats were trained to run a particular circuitous path to receive reward. After they became proficient, experimenters blocked the learned path and the rat was presented with 18 different possible paths radiating out from the starting point. Rats initially tried the original route, and when the blockade was discovered, rats strongly preferred the secondary route that pointed directly to the learned goal location, though this route had never been associated with reward. Tolman believed that this novel route taking ability had to be supported by the construction of a cognitive map within the animals mind, within which all of the elements of an environment are bound in a relational structure of space. This type of model based learning was antagonistic to the stimulus-response learning paradigm dominating the learning literature of the time, pioneered by behaviorists such as Pavlov and Skinner.

The discovery of place cells within the hippocampus was a boon to the cognitive map theory, providing an apparent neural code for allocentric space. In subsequent decades, further discovery of spatial features in the hippocampus and entorhinal cortex of rats (grid cells, border cells, speed cells, object-vector cells, ect.) bolstered the evidence for map-like representations encoded within the brain (Sargolini et al. 2006; Solstad et al. 2008; Kropff et al. 2015; Deshmukh and Knierim 2011; Moser, Rowland, and Moser 2015; C. Wang, Chen, and Knierim 2020). This led many to understand the hippocampus as a brain region for spatial navigation. Indeed, hippocampal lesion studies of rats demonstrated a profound reduction in spatial navigation ability (Sutherland, Whishaw, and Kolb 1983; Morris et al. 1982; Vorhees and Williams 2014). However, this conflicted with much of the existing lesion studies from humans, where the hippocampus and surrounding cortices were believed to primarily serve episodic memory functions.

For most of the 20th century, there existed a large divide between hippocampal literature from humans and rodents. But as neural recording technologies improved, and behaviors better

refined, rodent and human literature have converged together. Recent research demonstrates

multiple forms of spatial representations within the human hippocampus and medial entorhinal

cortices (Herweg and Kahana 2018; Aghajan et al. 2019). Place cells within the hippocampus of

rodents also show tuning properties for non-spatial dimensions (Aronov, Nevers, and Tank 2017;

Pastalkova et al. 2008; Weible et al. 2012), the dorsal hippocampus appears necessary for

complex tasks with abstract associative features in (Fortin, Wright, and Eichenbaum 2004;

Bradfield et al. 2020; Miller, Botvinick, and Brody 2017), and activity within the dorsal

hippocampus appears sufficient for the creation and expression of learned contextual

associations (Ramirez et al. 2013; Redondo et al. 2014; Ramirez et al. 2015; Roy et al. 2017;

Josselyn and Tonegawa 2020).

1.3.2.3 Calcium Imaging

Results from calcium imaging studies of place cells have in many ways confirmed

findings from electrophysiological studies, and the ability to image hundreds or thousands of

place cells at once have led to new discoveries. Some of these discoveries have contradicted

earlier assumptions about place cells derived from electrophysiology studies. For example,

hippocampal research supporting the cognitive map hypothesis supported the idea that the

place cells and place fields active in an environment should remain relatively stable over long

periods of time, reflecting a stable memory substrate (Wills et al. 2005). Placing an animal in an

environment activates a particular subset of place cells, and returning the animal into the same

environment some time later should reactivate those same cells, reflecting attractor states for

memory within a context (Wills et al. 2005; Guzowski, Knierim, and Moser 2004; Han et al.

2007; Dupret et al. 2010). It was long assumed that only salient changes within an environment

such as altering its shape (J. K. Leutgeb et al. 2005; S. Leutgeb et al. 2005) or delivering a

motivationally significant stimulus (Cressant, Muller, and Poucet 2002; Moita et al. 2004; Muzzio

2018) should cause memory updating and changes in place cell firing. However, this hypothesis

was difficult to test with electrophysiology because recordings of the same cell are very difficult to maintain for multiple days or weeks (even very small tissue movement relative to the recording probes can lead to loss of individual units). By contrast, with calcium imaging, researchers can record the same large population of place cells over multiple days or weeks..

Very few ephys studies have reported recording of the same place cell for more than a week, and these demonstrate stability of place cells within the same context (Lever et al. 2002). However, shorter term studies (over a few hours) suggested that place cell firing might change simply with the passage of time, even in the absence of environmental changes or salient events (Mankin et al. 2012). Long term calcium imaging studies of place cells in mice further supported this, showing that across long time scales (5-30 days) the spatial tuning of place fields is stable, but participation in population activity is unstable (Ziv et al. 2013). Hence, individual place cells represent the same location within the environment across days, but the likelihood that a place cell is active in two different sessions decreases with the time between sessions. This leads to episodes within a context that occur nearby in time sharing a larger proportion of hippocampal CA1 cells than episodes that occur far apart in time. Further research suggests that this may serve a functional purpose by linking events which occur close in time and separating those far apart (Cai et al. 2016; Mau, Hasselmo, and Cai 2020). Therefore, calcium imaging enables longitudinal experiments to investigate the stability of place cells across time, and thereby probe their role in encoding long term episodic memories.

1.3.3 Effect of Scopolamine on episodic memory

Evidence suggests that cholinergic projections to the hippocampus are necessary for storing new memories of novel experiences, but are less important for retrieving previously stored memories of familiar experiences (Green et al. 2005; Hasselmo 2006). Supporting this view, manipulations that impair cholinergic neurotransmission have been found to selectively

impair memory storage but not retrieval of semantic information (Atri et al. 2004; Hasselmo and McGaughy 2004) or fear memories (Huang et al. 2011). However, cholinergic disruptions can block retrieval of a learned spatial memory and disrupt working memory in a spatial task (Huang et al. 2011; Zhang et al. 2021). Conversely, drugs that enhance cholinergic neurotransmission have been found to improve memory capabilities (Buccafusco et al. 2005; Levin, McClernon, and Rezvani 2006; Shim et al. 2008; Echeverria and Zeitlin 2012), and while acetylcholine receptors are reduced in patients with Alzheimer's disease (Shimohama et al. 1986), drugs that upregulate acetylcholine are routinely prescribed to treat Alzheimer's patients due to its reduction of neuroinflammation (Lombardo and Maskos 2015).

Previous research has showed that administration of scopolamine, either systemically or via direct injection into the dorsal hippocampus, severely disrupts memory encoding (Anagnostaras, Maren, and Fanselow 1995; Saucier et al. 1996; Anagnostaras et al. 1999; Wallenstein and Vago 2001), place cell activity (Brazhnik et al. 2004; L. A. Newman and Gold 2016; E. L. Newman et al. 2017; Sun, Unnithan, and French 2021), and grid cells in the medial entorhinal cortex (E. L. Newman, Climer, and Hasselmo 2014). Yet while muscarinic blockade disrupts encoding and consolidation of spatial and fear memories (Huang et al. 2011), it does not change the avoidance of shock during the learning event itself (Kramis, Vanderwolf, and Bland 1975). Furthermore, scopolamine disrupts retrieval of a learned spatial task, but does not disrupt retrieval of a learned fear (Huang et al. 2011).

Recordings of place cells under the effects of scopolamine show an increased out-of-field firing probability (Brazhnik et al. 2004) and a disruption of theta phase precession (E. L. Newman et al. 2017). Sun et al. recently performed calcium imaging in mice before and after scopolamine administration and showed a decrease in recorded cells, reduced spatial information, and a broadening of place fields along the linear track (Sun, Unnithan, and French 2021). From this previous evidence, it is assumed that this disruption of place cell encoding

16

underlies the memory encoding failure caused by muscarinic blockade, but most research only addresses either the behavioral effects, or the physiological effects without a learning component. In Chapter 2, we sought to bridge this research gap and evaluate how scopolamine administration disrupts place cells, and how this disruption correlates with future memory retrieval performance after aversive learning.

1.4 PREFRONTAL CORTEX AND DECISION MAKING

1.4.1 Introduction

The prefrontal cortex ("PFC") of the brain has been shown to be critical for higher cognitive processes such as decision making and outcome evaluation. Previous experiences are utilized to predict possible outcomes, so it is no surprise that the PFC regions are heavily interconnected with memory regions such as the medial temporal lobe and hippocampus (Preston and Eichenbaum 2013). The hippocampus has bidirectional connectivity with multiple PFC subregions, including the anterior cingulate cortex ("ACC") (Jones and Wilson 2005; D. V. Wang and Ikemoto 2016). The ACC is a cortical region, and has been shown to be necessary in memory retrieval and effortful decision making (Wirt and Hyman 2019; Hart et al. 2017). In the final Chapter of this dissertation, I will present work done in collaboration with Dr. Evan Hart and Dr. Alicia Izquierdo where we evaluated how cells within the ACC encoded effortful behaviors using chemogenetic manipulations and in-vivo calcium imaging.

1.4.2 Neural basis of effort-based choice

Every day we make many decisions that involve evaluating the relative costs and potential outcomes of available options. For instance, when preparing dinner, I could choose to heat up a frozen meal with relatively little effort, or choose to exert more time and energy to prepare and cook chicken adobo. One option is easy and has little reward, while the latter is

more effortful yet much more rewarding. Understanding how this evaluative process occurs within the brain has been of interest for decades as it could provide further understanding for neural diseases that affect willingness to exert effort, such as depression.

The striatum, specifically the mesolimbic dopamine circuitry (J. D. Salamone et al. 1991; John D Salamone et al. 2017), has been the primary region of research due to its involvement in rewarded outcome representations (Ljungberg, Apicella, and Schultz 1992; Schultz 2016). Recently more research has also demonstrated relevant activity of the ACC during effortful decision making (Walton et al. 2003). Neurons within the ACC reflect the relative value of outcomes (Lapish et al. 2008; Azab and Hayden 2017; Hunt and Hayden 2017) and also signal a reward prediction error signal as seen within the striatum (Hayden, Pearson, and Platt 2009; Kennerley, Behrens, and Wallis 2011).

Recent research using excitotoxic NMDA lesions within the ACC further demonstrated its necessity during an effortful choice-based decision making task (Hart et al. 2017). However, these lesions disrupt not only the principal neurons of the injected region, but also axons that pass through that area. Excitotoxic lesions are also an irreversible inactivation technique that is hard to pinpoint the exact extent of inactivation. Given these methodological issues, researchers have begun to use a novel manipulation technique called DREADDs. This method can target specific neurons within a region, is reversible, and has a fluorescent label for ex-vivo localization. Using DREADDs, we evaluated how temporary excitation or inhibition of ACC excitatory neurons affected effortful decision making. In a separate cohort, we then recorded neural activity of these neurons via calcium imaging and related their firing activity to different phases of the effortful choice behavior.

1.4.3 Chemogenetics - "DREADDs"

Chemogenetics is a modern neuroscience research tool that allows scientists to manipulate the excitability of cells (Armbruster et al. 2007; Alexander et al. 2009). This method is commonly referred to as *DREADDs*, or "Designer Receptors Exclusively Activated by Designer Drugs (Smith et al. 2016). As the name implies, it involves the introduction of exogenous metabotropic receptors into specific cells that only respond to an exogenous ligand (Roth 2016). This technique allows for researchers to target specific cells within one region (Stolyarova et al. 2019) or across the entire brain (Alexander et al. 2009). DREADDs can be used to either make these neurons more or less excitable depending on the chosen DREADD, referred to as G_q- (excitable) and G_i-DREADDs (inhibitory) (Pei et al. 2008). In addition to encoding the receptor, the viral delivery mechanism also encodes for a fluorescent tag, allowing researchers to confirm the location of excitation/inhibition.

1.5 SUMMARY

The hippocampus has been an extensively studied brain region involved in memory formation. Most of this work had been performed with electrophysiology in rats, laying the groundwork for our understanding of place cells in learning and memory. With the explosive growth of calcium imaging applied in mice during the past decade, there developed a wide-gap between findings from mouse imaging studies and previous rat studies. To address this gap of knowledge, I adapted calcium imaging to the rat so that researchers can begin to directly compare these differences. We present these methodological advances, as well as select applications of the technique and how they expand our understanding of the brain.

Work presented in this dissertation spans multiple brain regions and lab collaborations, all with the goal of improving our understanding of how learning and decision making occur within the brain. My primary tool for this work has been in-vivo single photon calcium imaging, a relatively nascent technique for modern neuroscience that I developed for application to the rat. Chapter 2 will present our most recent data, recording from the hippocampus of rats as they learn an aversive association, and how scopolamine affects aversive learning and its associated neural response. The possibility of this work is thanks, in part, to novel imaging capabilities developed at UCLA. Chapter 3 summarizes collaborative work developing a novel Large Field of View Miniscope. This camera was developed for larger mammals, capable of recording thousands of neurons simultaneously at single cell resolution. Finally, Chapter 4 summarizes published work on our recordings of ACC neurons during an effortful decision making task. This collaboration was the first demonstration of single-photon calcium imaging in freely behaving rats, and revealed how different neurons are related to the initiation of effortful behaviors or reward receipt.

CHAPTER 2: Hippocampal Imaging during Learning

2.1 INTRODUCTION

In this study, we investigated cholinergic modulation of memory at the cellular level by performing *in-vivo* calcium imaging of neurons in the hippocampal CA1 layer while administering systemic injections of scopolamine (a muscarinic acetylcholine antagonist) to freely behaving rats as they performed an avoidance learning task.

The rodent hippocampus contains spatially tuned neurons called *place cells* that fire selectively when the animal visits a given location within a familiar environment ((J. O'Keefe and Dostrovsky 1971; John O'Keefe 1976). A population of many place cells can form a distributed memory representation--or *cognitive map*--of a spatial environment (O'Keefe & Nadel, 1978), and place cells will change their firing field adjacencies will moved between different environments (a process known as "remapping") (S. Leutgeb et al. 2005). Thus, each familiar location is labelled with a unique "codeword" represented by a specific pattern (or *population vector*) of active place cells. This cognitive map is believed to represent an internal memory representation of the external spatial environment's geometry that supports memory and model-based planning during navigational decision making. Hence, at the population level, retrieving a memory of a familiar spatial location thus corresponds to activating a specific place cell population vector pattern that has previously been stored as a codeword for that location, and research has shown that activation of this contextual code is causal to behavioral performance (Ramirez et al. 2013; Redondo et al. 2014; Ramirez et al. 2015).

In addition to retrieving stored memories of familiar spatial locations, the hippocampus is also necessary for storing new episodic memories. Prior studies have shown that aversive events can alter the location-specific tuning properties of hippocampal place cells, and thereby modify spatial memory representations of environments where danger has occurred, generating

a novel population vector codeword (Moita et al. 2003; Moita et al. 2004; M. E. Wang et al. 2012; Schuette et al. 2020). However, it is not well understood why place cell remapping occurs in response to aversive events, or how this contributes to learning and behavior. For what reason do aversive experiences alter spatial memory representations, and in what ways might aversively-induced place cell remapping facilitate better navigational decisions during subsequent model-based planning? To investigate these questions, we performed in-vivo calcium imaging of CA1 place cells while freely behaving rats acquired and extinguished a shock avoidance. To address the nature of this remapping, we blocked aversive learning with systemic scopolamine (a muscarinic acetylcholine antagonist) to demonstrate that the remapping effects are specific to encoding.

Acetylcholine is one of the most prevalent neurotransmitters in the brain, and one of the primary neurotransmitters within the hippocampus (Everitt and Robbins 1997; Solari and Hangya 2018; Maurer and Williams 2017). Prior studies have shown that scopolamine can disrupt the spatial firing of place cells (Brazhnik et al. 2004; E. L. Newman et al. 2017; Sun, Unnithan, and French 2021), impairs place remapping (Douchamps et al. 2013), and blocks aversive and spatial learning (Blokland, Honig, and Raaijmakers 1992; Wallenstein and Vago 2001; Huang et al. 2011). Here, we report that systemic scopolamine impairs avoidance learning while minimally disrupting the spatial firing patterns of place cells and significantly disrupts place cell remapping caused by normal aversive learning.

2.2 METHODS

2.2.1 Subjects

17 Long-Evans rats (7M, 7F; *Charles River*) were used in this experiment at 3 months of age at the start of surgical procedures before behavioral training.

2.2.2 Surgical procedure

Subjects were given two survival surgeries prior to behavior training in order to record fluorescent calcium activity from hippocampal CA1 cells. During the first surgery, rats were anesthetized with 5% isoflurane at 2.5 L/min of oxygen, then maintained at 2-2.5% isoflurane while a craniotomy was made above the dorsal hippocampus. Next, 1.2 uL of AAV9-Syn-GCamp7s (*AddGene*) was injected just below the pyramidal layer (-3.6 AP, 2.5 ML, 2.6 DV) via a 10uL Nanofil syringe (*World Precision Instruments*) mounted in a Quintessential Stereotaxic Injector (*Stoelting*) controlled by a Motorized Lab Standard Stereotax (*Harvard Apparatus*). Left or right hemisphere was balanced across all animals. One week later, the rat was again induced under anesthesia and 4 skull screws were implanted to provide stable hold for the implant. The craniotomy was reopened to a diameter of 1.8 mm, and cortical tissue and corpus callosal fibers above the hippocampus were aspirated away. Following this aspiration, and assuring no bleeding persisted in the craniotomy, a 1.8mm diameter Gradient Refractive INdex lens ("GRIN lens", *Edmund Optics*) was implanted over the hippocampus and cemented in place with methacrylate bone cement (Simplex-P, *Stryker Orthopaedics*). The dorsal surface of the skull and the bone screws were cemented with the GRIN lens to ensure stability of the implant, while the surface of the lens was left exposed.

Two to three weeks later, rats were again placed under anesthesia in order to cement a 3D printed baseplate above the lens. First a second GRIN lens was optically glued (Norland Optical Adhesive 68, *Edmund Optics*) to the surface of the implanted lens and cured with UV light. The pitch of each GRIN lens is .25, so implanting 2 together provides a .5 pitch.This half pitch provides translation of the image at the bottom surface of the lenses to the top while maintaining the focal point below the lens. This relay implant enables access to tissue deep below the skull surface. Magnification of the image is performed by the miniscope (see X.XX Miniscope Design). The miniscope was placed securely in the baseplate and then mounted to

the stereotax to visualize the calcium fluorescence and tissue. The baseplate was then cemented in place above the relay lenses at the proper focal plane and allowed to cure. Once rats had been baseplated, they were placed on food restriction to reach a goal weight of 85% *ad lib* weight and then began behavioral training.

2.2.2.1 Histology

Following the end termination of the experiment, rats were anesthetized with isoflurane, intraperitoneally injected with 1ml of pentobarbital, then transcardially perfused with 100mL of 1x PBS followed by 200mL of 4% PFA in 1x PBS to fix the brain tissue. Brains were sectioned at 40 micron thickness on a cryostat (Leica), mounted on slides, then imaged on a confocal microscope (Zeiss) to confirm GFP and GRIN lens placement.

2.2.3 Calcium imaging

Single-photon calcium imaging was performed throughout the behavioral training to monitor population activity from hippocampal CA1. We utilized a novel UCLA miniscope design (miniscope.org) designed for larger mammals, such as non-human primates and rats (for more on design, see Chapter 3). Imaging sessions lasted for 15 minutes every other day, and from 20 to 60 days. For most rats, the imaging field of view was stable throughout the recording. However, some rats had noticeable changes between some sessions, so matching cellular activity across these sessions for certain rats was not possible. Imaging parameters (LED power, focal plane, and digital gain) for each rat were established prior to the first recording session and were kept constant as long as possible. In few cases, some sessions required increased LED power or slight focal plane adjustments in order to keep the recording quality as consistent between sessions. Imaging was captured at 22Hz, with low or medium digital gain (1x or 4x) within an LED power range of 4-40.

2.2.4 Data processing

Imaging videos were recorded with the miniscope software alongside a behavior camera and were timestamped in a common time base relative to the start of the recording. After the recording session, custom python code concatenated all of the session videos into one tiff stack and cropped the image to the lens size, typically about 700x700 pixels. The video was downsampled temporally by a factor of 2, normally yielding about 10,000 8-bit frames per 15 minute recording.

2.2.4.1 Cell extraction and spike inference

These cropped tiff stacks were then processed in python using the CaImAn data processing pipeline ("CAlcium IMage ANalysis, CaImAn, (Giovannucci et al. 2019)). First, the video was motion corrected using the included non-rigid motion correction algorithm ,which is particularly necessary for large field imaging due to inhomogeneous motion artefacts (Pnevmatikakis and Giovannucci 2017). Source extraction was then performed on this motion corrected video in order to identify cells after accounting for the background fluorescence artefacts inherent in single-photon endoscopic imaging (Zhou et al. 2018). Spatial contours and fluorescent traces for each cell were saved and subsequently processed in MATLAB (*Mathworks, 2016*). Raw calcium traces were first low-pass filtered (pass band=.3, stop band = .4), and then deconvolution of these traces was performed using the OASIS method from the Matlab CNMF-E package (Pnevmatikakis et al. 2016). This deconvolution accounts for the slow rise and decay of fluorescence from calcium indicators to infer spike times underlying the calcium signal. Deconvolved calcium activity was next normalized for each cell within the session. Deconvolved calcium activity will be used to compare neural activity to behavior, and will be interchangeably referred to as "spikes" throughout the remainder of this chapter.

2.2.4.2 Behavior tracking and segmentation

A webcam mounted in the behavior room tracked a red LED located on the top of the miniscope and this video was saved alongside the calcium imaging via the miniscope software. These behavior video files were initially processed by custom python code, where all the session videos were concatenated together into one tiff stack, then the median of the stack was subtracted from each image, and finally they were all rescaled to the original 8-bit range to yield the same maximum and minimum values pre subtraction. Background subtracted behavior videos were then processed in MATLAB. The rat's position in each frame was determined using the location of the red LED on the camera. Extracted positions were then rescaled to remove the camera distortion and convert the pixel position to centimeters according to the maze size. Positional information was then interpolated to the calcium imaging time frame to align behavior with extracted cell activity.

Position was then segmented to determine path selection and direction of travel. In the initial cohort of animals, the orientation chip on the miniscope was unreliable, so BNO orientation information was not used. We established behavioral epochs when the rat ran between the reward zones without stopping and turning around, called "beelines". There are four types of beelines, segregated by which path and direction they occur on (Short vs Long, Leftwards vs Rightwards), so each cell has four tuning curves within a given session.

2.2.4.3 Place cell classification

Place fields for each cell were constructed for each beelines separately by computing the sum of the deconvolved calcium transients per bin along that trajectory divided by the time spent in each bin. For each place field, we calculated the spatial information and the within session field correlation. Spatial information for each place field trajectory was calculated according to (Skaggs et al. 1993), for each of the four trajectories. Within session place field

correlation was computed by randomly resampling beelines within a trajectory into two halves, computing a tuning curve for each, then correlating these split tuning curves. This was performed 200 times for each cell along each trajectory. Place cells were required to have a median within session significance value of p≤0.05, an average transient rate >=1 along a trajectory, and have tuning curves occupying <70% of the trajectory length. This selects for cells that are consistently stable within a session, so that we can compare how these manipulations influences place field stability.

2.2.4.4 Event Induced Remapping Index: EIRI

To measure place cell remapping induced by shocks or barriers, we computed an *event-induced remapping index* (EIRI) that quantified the degree to which an event altered the between-session correlations between place cell population vectors. The basic reasoning behind this measurement was that if an event induces remapping of place cells, then between-session place cell population vector correlations should be lower for pairs of sessions that straddle the event than for pairs of sessions that do not straddle the event.

The first step in deriving the EIRI was to derive four different population vector correlation matrices: M_{LR}^{pre}, M_{RL}^{pre}, M_{LR}^{post}, and M_{RL}^{post}. Fig. 2.2.4.4 illustrates this process using example data from one rat in the drug-free shock condition. As shown in the figure, each of the four matrices was derived in the same manner (by correlating the columns of one tuning curve heatmap against the columns of another) from a different between-session pair of tuning curve heatmaps.. The M_{LR}^{pre} matrix correlates columns from the pre-shock versus shock session heatmaps for left-to-right journeys; this matrix was derived only from cells that met the place tuning criterion during left-to-right journeys at least in one of the two sessions. The M_{RL}^{pre} matrix was computed in the same way from cells that met the place tuning criterion during right-to-left

27

journeys. Likewise, M_{LR}^{post} correlates columns from the shock versus post-shock session

heatmaps during left-to-right journeys, whereas M_{RL}^{post} does the same for right-to-left journeys.

It has previously been shown that shock-induced place cell remapping tends to occur

mainly in "unsafe" regions of an environment where shock has been encountered, and not in

"safe" regions where shock has not occurred. Therefore, to separately analyze remapping within

safe versus unsafe regions of the short path, three subsets of pixels (marked by black outlines

in the correlation matrices of Fig. 2.2.4.4) were extracted from near the diagonal in each of the

four correlation matrices (see Methods). These three sets of pixels shall be referred to as the left

(*L*) zone set (n=13 pixels per matrix), center (*C*) zone set (n=23 pixels per matrix), and right (*R*)

zone set (13 pixels per matrix). The *L* and *R* pixel sets were combined to form the "safe zone" of

the short path (13+13=26 pixels per matrix), since shocks never occurred at either end of the

maze. Conversely, the *C* pixel set constituted the "unsafe zone" of the short path where shocks

were delivered (exact locations of shock delivery depended upon each rat's behavior, so the

center zone was selected by an algorithm that was identical for all event analyses; see

Methods). To derive separate EIRI measurements for the safe and unsafe zones along the short

path, two Wilcoxon signed-rank tests were performed on the correlation matrix pixels sets. The

safe zone EIRI was derived by making a paired comparison between the combined safe zone

pixels (n=52) from M_{LR}^{pre} and M_{RL}^{pre} against the combined safe zone pixels from M_{LR}^{post} and M_{RL}^{post},

whereas the unsafe zone EIRI was derived by making a paired comparison between the

combined unsafe zone pixels (n=46) from M_{LR}^{pre} and M_{RL}^{pre} versus the combined unsafe zone

pixels from M_{LR}^{post} and M_{RL}^{post}.

The EIRI was computed as $log_{10}(p) \times sign(d)$, where *p* denotes the p-value from the Wilcoxon test, and *d* is the sign of the median difference between paired elements of the compared pixel sets. Significant event-induced remapping of place cells at the .01 level was considered to occur if EIRI<-2, because $log_{10}(.01) = 2$, and a negative median difference indicates lower population vector correlations between pairs of sessions that straddle the event than between pairs of sessions that do not. Conversely, significant event-induced stabilization of place cells was considered to occur if EIRI>2, since a positive median difference indicates higher population vector correlations between pairs of sessions that straddle the event than between pairs of sessions that do not. Within the range -2<EIRI<2, the event was considered to have no significant effect upon the stability of place cell population vectors.
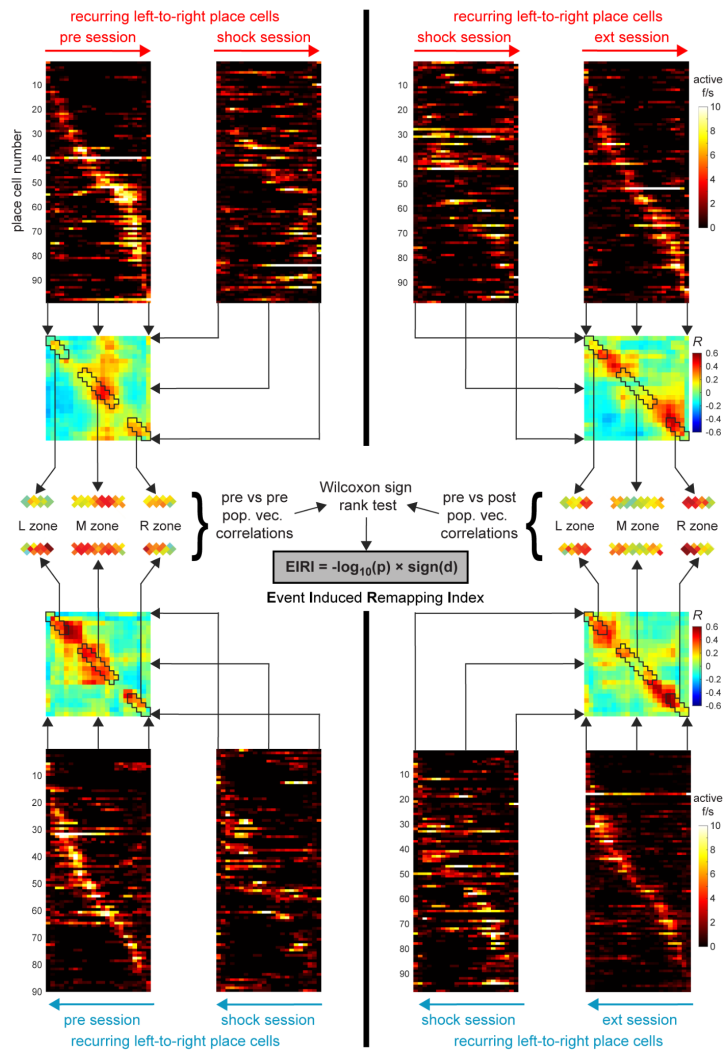
Figure 2.2.4.4. Demonstration of EIRI calculation. For each manipulation group, we correlate the population vector along the track either before (left panels) or after (right panels) the learning event. Population vectors for the manipulation session are constructed from all data before introduction of the manipulation. This population vector correlation matrix (middle) is then divided into either the left, center, or right bins along the track. We then compare the extent of remapping in the middle (manip. Zone, "unsafe") and the ends (left and right combined, "safe") using a Wilcoxon sign-rank test. The probability of this test is then $\log_{10}$ scaled, maintaining the sign of the magnitude difference (post - pre), to yield the EIRI for each manipulation. EIRI values >2 indicate significantly increased correlation, and <-2 indicate significant decorrelation caused by the manipulation.

2.2.4.5 Across session cell registration

Contours computed from CaImAn were normalized by their own max value then

thresholded at .5 to generate compact contours for all cells. Then each session was manually

aligned using the contours and vasculature simultaneously using custom MATLAB scripts. In

addition to linear translations, It was sometimes necessary to radially scale this data as well to account for slight differences induced by camera placement and different focal positions from the electrowetting lens. Matching across sessions close in time (+/- 4 sessions) was possible for all rats, but it proved difficult to match sessions far across in time due to slow shifts of tissue or focal plane beneath the lens. Therefore we compared cell activity before and after our manipulations, but since each manipulation was spaced out to accommodate extinction time we did not compare a cell's response to different manipulations

Contour alignment was performed using CellReg to register cells across all sessions of interest based on their centroid distances and spatial contour correlations (Figure 2.2.4.5A) (Sheintuch et al. 2017). Distributions of centroid distances and spatial correlation for all cell pairs within 24 microns were computed, yielding a two-dimensional distribution that can be modeled and given a probability threshold to match cell pairs (Figure 2.2.4.5B). Cell pairs with a probability >.5 for both the centroid and correlation distributions were matched (low centroid distance and high spatial correlation), which is expected when recording the same cell. Examples of this modelling and matched cells for one animal are presented in Figure 2.2.4.5.
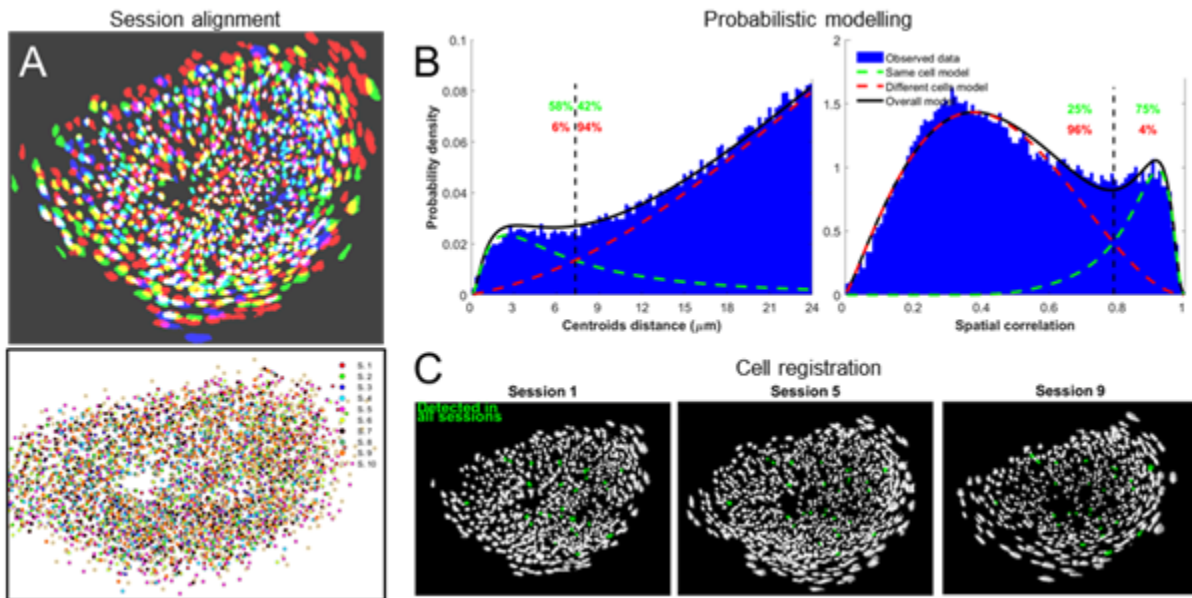
Figure 2.2.4.5 Demonstration of the across session cell registration method (A) First, contours are aligned using a non-rigid alignment method to align their spatial contours (top) and compute the centroid locations of these contours (bottom). (B) A windowed (24 micron, 12 pixel) distribution is computed for each cell for all other cells detected near it in the other sessions. This allows us to classify cells that are within the same location (left) and have a similar spatial contour (right). (C) Using a .5 probability of both the spatial contour and centroid joint distributions, we classify each cell as a match or not across the recorded sessions (in this example 9 sessions, or 16 days).

2.2.1 Behavior: Two-Armed Bandit Task

The task used in this experiment is essentially a linear alternation track with two arms connecting the reward locations. One arm (2.5 meters) directly connects the reward locations, while the other arm is indirect and twice as long (5 meters). Holistically these arms form a 2.5 by 5 meter rectangle with the reward locations at the corners of one long side (Fig. 2.2.1) and is elevated 1 meter off the ground. The paths are 10 cm wide spanned by small metal bars along the entirety of the short and long paths. The reward zones are coated wood, 14 cm wide, 20 cm long, at a 45 degree angle with the two paths. The entire maze has a short 1cm wall in order to provide a safe graspable ledge in case the rat loses its footing. The outer perimeter of the short path has a slightly taller wall angled 45 degrees away from the path to protect the wiring connected to the short path bars. 20mg chocolate sucrose pellets are delivered through a metal tube at the end of the reward zone via an automated hopper.

32

Rewards are delivered at the opposite reward location from their previous reward as the rat passes through the center of either path. Both paths yield delivery of 2 pellets, and there is no time out period after delivery. The rat must enter the most recent reward delivery location before the opposite side will be rewarded, forcing an alternation behavior. The rats are allowed to choose either path, and since they are equally rewarded, they demonstrate a preference for the short path over the long path after only a few sessions. Rats are given 15 minute recording sessions every 48 hours in order to minimize potential photobleaching of the calcium indicator. Once a rat demonstrated a consistent short path preference and sufficient running behavior (>2 short paths per minute and a 2:1 short:long ratio in the first 10 minutes for two consecutive sessions) we introduced a manipulation in the subsequent session. All manipulations were spaced out with at least 3 regular sessions in between, and while the rat has performed at criterion for at least 3 sessions.
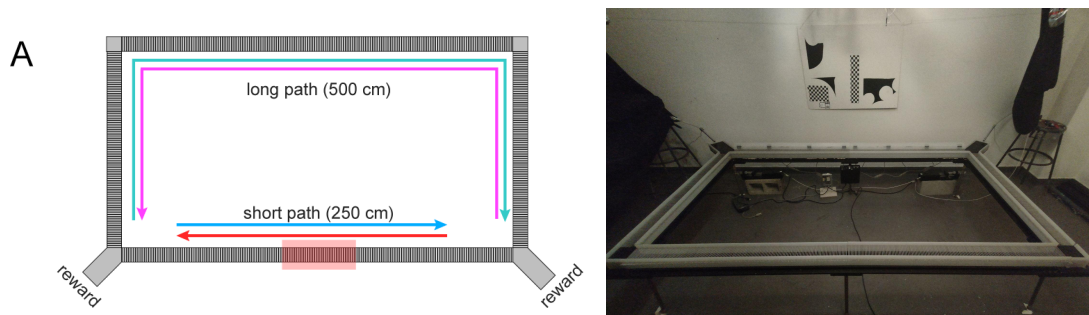
Figure 2.2.1. (Left) Diagram of maze depicting trajectories, triggerable shock zone, and reward zones. (Right) Picture of maze.

2.2.1.1 Quantification of behavior

Task performance during each session was quantified by measuring the short path reward rate (R_S, defined as the mean number of rewards earned per minute by taking the short path throughout the session) and the short path reward probability (P_S, defined as the number of rewards earned by choosing short path divided by the total number of rewards earned in the session). Figure 2.3.1.1 shows that rats took 3-6 days of training to reach a criterion level of

performance for earning rewards via the short path (see Methods). Rats then began receiving

four types of experimental manipulations: *shock avoidance training* (SAT), *barrier obstacle*

control (BOC) sessions, *systemic scopolamine injections* (SSI), and shock avoidance training

with a systemic scopolamine injection (SAT+SSI). Table 2.3 summarizes the order in which

these four manipulations were given to each of the rats in the study.

2.2.1.2 Shock Avoidance Training (SAT)

After rats reached short preference criteria, the next session was a shock session in

order to evaluate how aversive learning altered the hippocampal representation of the

environment. All 14 rats received at least one drug-free SAT session during the experiment, but

only 6 rats received the SAT session as their first manipulation after initially reaching criterion for

preferring the short path (see Table 2.3 and Figure 2.3.1.1 for a full breakdown). The first 10

minutes of the session proceeded as normal. Then, while the rat was occupying one of the two

rewarded corners, a 1.0 mA grid-scrambled current was switched on to electrify a 50 cm length

of the maze track located in the center of the short path (Fig 2.2.1). No signals were given to

indicate the shock grid was on, nor were there any markings indicating its location (wires were

connected along the entirety of the short path, but only the central portion was connected to the

shock grid scrambler). Exposure to the shock was entirely self-initiated, and this shock was left

active for the rest of the session until the rat was removed. Consequently, during the final 5

minutes of the SAT session, the rat received a mild footshock whenever it passed through the

center of the short path. There was no visual or tactile cue on the floor to identify which portion

of the track was electrified, because all four straight sections of the maze were identically

constructed from evenly spaced metal grid bars.

After receiving 1-2 shocks on the short path, rats subsequently avoided the short path for

the remainder of the session, either by taking the long path instead, or by disengaging from the

task and remaining in a safe region of the maze (usually at one of the two rewarded corners;

see example in Fig. 2.3.1.1). Hence, the SAT manipulation prevented rats from taking the short

path during most of the final 5 minutes of the session, by introducing a novel aversive stimulus

(footshock) at the center of the short path. When rats disengaged from earning rewards, they

typically became engaged in other behaviors such as grooming or peering frequently over the

edge of the maze. However, they did not spend a significant amount of time freezing in a

crouched posture, as rats typically do in classical contextual fear conditioning studies, where

they are confined to a small chamber and thus not able to move away from the location where

footshock was delivered. After the SAT session, most rats continued to avoid the short path

during subsequent sessions. Thus, rats showed long-term retention of shock avoidance

behavior that gradually extinguished over time.

However, multiple things occur during this aversive learning: 1) the rat learns to avoid the

shock zone, 2) the rat avoids that portion of the environment and reduces behavioral experience

there, 3) there is a sudden novel stimulus introduced to the context. So in order to control for

these later two confounds and isolate the effect of aversive learning, we employed a Barrier

Obstacle Manipulation.

2.2.1.3 Barrier Obstacle Control (BOC)

After rats reached short preference criteria, 6 rats received a BOC session as their first

manipulation after initially reaching criterion for preferring the short path. During BOC sessions,

the rat performed the standard alternation task for the first 10 minutes of the session. Then,

while the rat was occupying one of the two rewarded corners, the experimenter entered the

room and placed a clear plexiglass barrier in the center of the short path. Consequently, during

the final 5 minutes of the BOC session, the rat could no longer traverse the short path between

the two reward locations (see Fig. 2.3.1.1). While the barrier was in place, rats persisted in

trying to take the short path on most trials, and then took the long path instead after

encountering the barrier. Hence, similar to SAT sessions, the BOC manipulation prevented rats

from taking the short path for the final 5 minutes of the session, and also introduced a novel stimulus (the barrier) at the center of the short path. But unlike SAT sessions, there was no aversive stimulus presented during BOC sessions. Rats did not avoid entering the short path during the final 5 minutes of BOC sessions (as they did during SAT sessions), and showed no avoidance of the short path on subsequent days after the barrier was removed. Thus any effects seen in the shock manipulation and not in the barrier manipulation can be attributed to aversive learning and not because of forced experiential avoidance.

2.2.1.4 Shock Avoidance Training with Systemic Scopolamine Injection (SAT+SSI)

One outstanding question from the aversive learning experiment is whether the learning is causal to any remapping effects. In order to address this, we used scopolamine to block shock acquisition in some animals to compare to shock acquisition sessions. 10 rats were given an intraperitoneal injection of scopolamine (1 mg/kg) prior to a SAT session. 6 rats received this treatment before their first shock experience (SSI+SAT1) and 4 rats received this treatment before their second shock experience (SSI+SAT2). 30 minutes after the injection (to allow for the time course of systemic scopolamine to affect the hippocampus), the rat performed the SAT task described above, where the shock grid was turned on at minute 10.

2.2.1.5 Systemic Scopolamine Injection (SSI) control

Finally, to demonstrate that scopolamine administration alone was not responsible for any effects seen in the SSI+SAT manipulation, 3 rats were given an intraperitoneal injection of scopolamine (1 mg/kg) 30 minutes prior to the session to systemically block muscarinic acetylcholine receptors with no further manipulation.
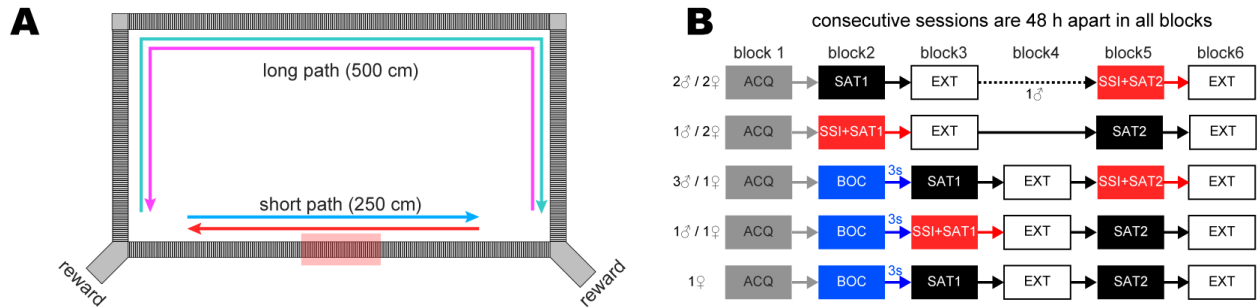
Figure 2.2.2. Manipulation Summary (**A**) Another maze image highlighting the possible trajectories and shock/barrier location (red shaded area) (**B**) Manipulation order for the different groups. SAT = Shock Avoidance Training (½ indicates if this is the first or second shock received); SSI+SAT = Systemic Scopolamine Injection prior to SAT session; BOC = Barrier Obstacle Control

	Gender	SAT	BOC	SSI	SAT+SSI
Hipp6	F	1			
Hipp7	M	1			
Hipp8	M	1			
Hipp9	F	1			
Hipp12	M	2	1		3
Hipp13	M	2	1		3
Hipp15	F	1	2		3
Hipp18	F	2	1		3
Hipp30	M	3, 4	1	5	2
Hipp31	M	1, 2		3	4
Hipp32	M	3, 4		1	2
Hipp34	F	3	1		2
Hipp35	F	2, 3	1		
Hipp36	F	3		1	2

Table 2.3. Manipulation Order and gender for all subjects. The first four rats were unable to complete the planned manipulations due to limitations caused by COVID-19. SAT = Shock Avoidance Training (½ indicates if this is the first or second shock received); SSI+SAT = Systemic Scopolamine Injection prior to SAT session; BOC = Barrier Obstacle Control

2.3 RESULTS

2.3.1 Shock induced aversion is blocked by Scopolamine

Rats quickly learned to prefer the short path, all reaching performance criterion within 3-6 sessions (Fig 2.3.1.1C, D). Shock Avoidance Training ("SAT"), Systemic Scopolamine Injection with SAT ("SSI+SAT"), and Barrier Obstacle Training ("BOC") manipulations all significantly reduced short path reward rate (R_s) compared to the 10 minute baseline period (Fig. 2.3.1.1E, F; Wilcoxon Signed-Rank test; SAT R_s pre>post, p=0.00024; SSI+SAT R_s pre>post, p=0.0039; BOC R_s pre>post, p=0.0313). Scopolamine administration also impaired behavioral performance during the first 10 minutes (Figure 2.3.1.1E), but reduction of R_s was not different between the drug vs non-drug group (effect of drug: Wilcoxon rank-sum test ΔR_s SSI+SAT>SAT, p=0.3184). To test for retrieval effects of aversive learning we compared the behavior performance for the retrieval session 48 hours later with performance 48 hours before the manipulation. This avoids the impact scopolamine had on baseline performance and comparing drug vs non-drug states. SAT caused a significant reduction in R_s in the subsequent session (Fig. 2.3.1.1G, H; Wilcoxon Signed-Rank test SAT R_s pre>post, p=0.00073). Conversely, scopolamine administration prior to shock training eliminated this avoidant retrieval effect (Fig. 2.3.1.1G, H; Wilcoxon Signed-Rank test SSI+SAT R_s pre>post, p=0.125). This effect was true regardless of the order of shock and drug experience (Fig. 2.3.1.1H; effect of drug: Wilcoxon rank-sum test ΔR_s SSI+SAT>SAT, p=0.0295; effect of order: Wilcoxon rank-sum test ΔR_s 1st>2nd, p=0.2829). Exposure to scopolamine alone (SSI manipulation) did not produce subsequent avoidance (Signed-Rank test SSI R_s pre>post, p=.25). Additionally, BOC caused a moderate but significant increase in R_s (Fig. 2.3.1.1G, H; Wilcoxon Signed-Rank test BOC R_s pre>post, p=0.0313); likely because this manipulation was performed first for all in the group and they had not yet reached their running asymptote.
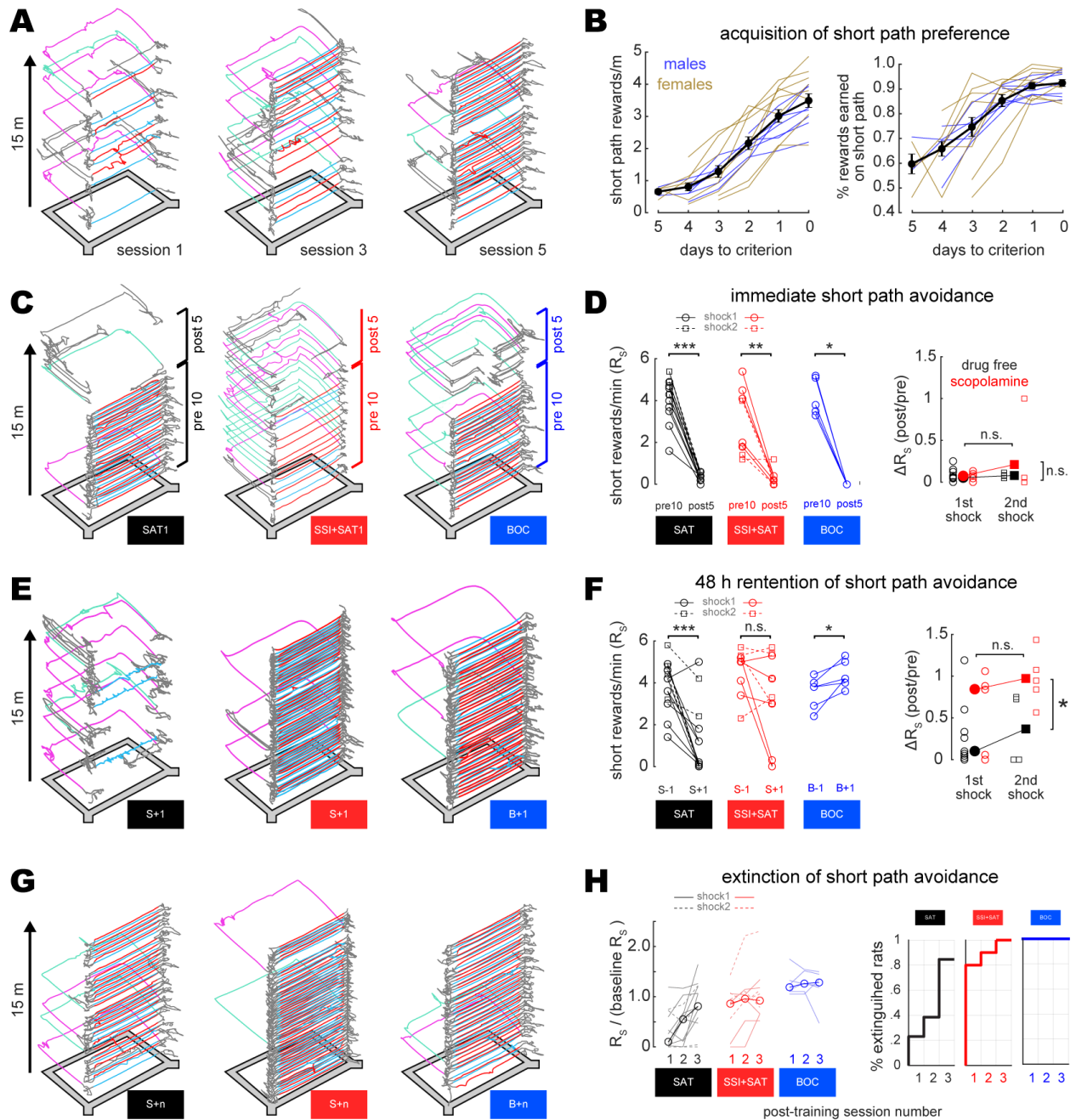
Figure 2.3.1.1. Behavioral acquisition of the Two-armed bandit task and effect of manipulations. (**A**) Example path plot of one rat's short path preference development during their first, third, and fifth session (where criterion was met) within the maze. (**B**) Acquisition curves for males (blue) and females (yellow) for their number of rewards along the short path (left) and proportion of total rewards earned along the short (right) before their first manipulation. (**C**) Example path plots from (left to right) SAT, SAT+SSI, and BOC manipulation sessions, where the manipulation is introduced after 10 min. (**D**) (left) Effect of manipulations on behavior during the manipulation session on the number of rewards/min along the short path and (right) change from baseline (first 10 min of session), separated by shock experience. (**E**) Example path plots from the session immediately following (left to right) SAT, SAT+SSI, and BOC sessions. (**F**) (left) Effect of manipulations on behavior 48 hours later on the number of rewards/min along the short path and (right) change from baseline, separated by shock experience. SAT manipulation had a significant reduction of short reward rate that was not present in SAT+SSI.

39

2.3.2 Shock induced remapping is blocked by Scopolamine

We utilized calcium imaging of hippocampal CA1 pyramidal cells to monitor population activity in response to various learning events. Utilizing a novel Large Field of View Miniscope ("LFOV Miniscope", Chapter 3), we simultaneously recorded activity from hundreds of cells expressing GCaMP7s before, during, and after learning took place (Figure 2.3.2.1). We specifically evaluated place cells since they reflect a cognitive spatial map within a context. Place field remapping is believed to be correlated with learning (Cressant, Muller, and Poucet 2002; Alvernhe, Save, and Poucet 2011; Sanders, Wilson, and Gershman 2020), especially aversive learning (Moita et al. 2003; Moita et al. 2004; M. E. Wang et al. 2012; E. J. Kim et al. 2012; E. J. Kim et al. 2015; M. E. Wang et al. 2015; Cai et al. 2016; Schuette et al. 2020).
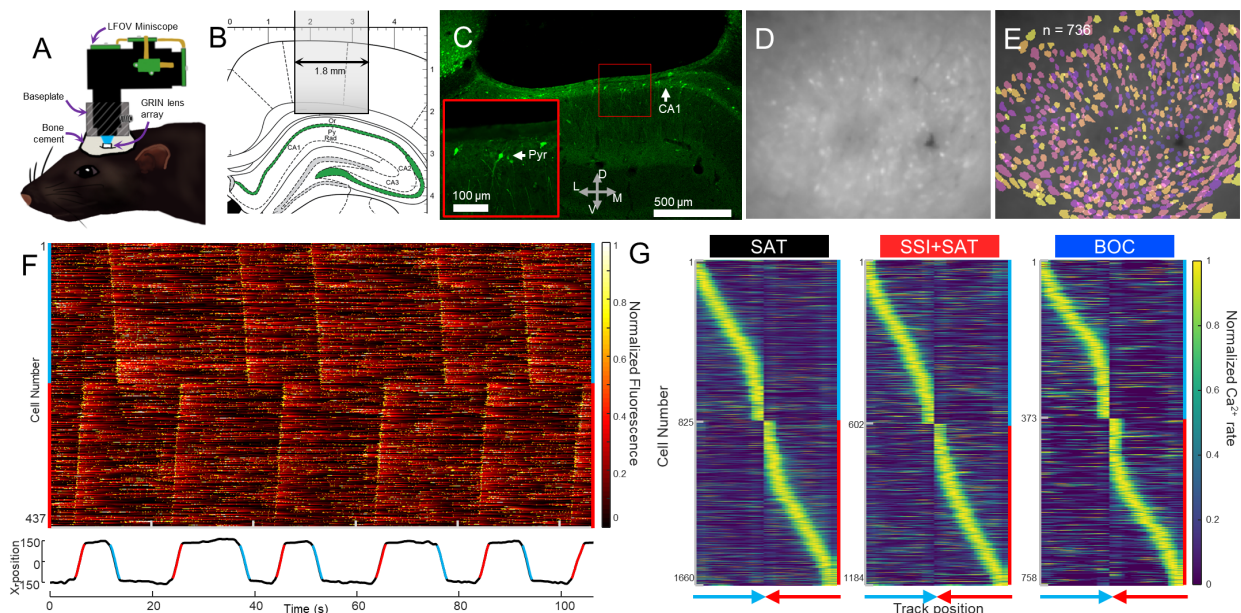
Figure 2.3.2.1 Calcium imaging during linear linear behavior. (**A**) Depiction of a rat with the Large-Field of View (LFOV) Miniscope. (**B**) Schematic of GRIN lens implantation above the CA1 pyramidal layer, highlighted in green (image modified from Paxisnos and Watson 6th edition) Cross-section of the LFOV Miniscope used for calcium imaging. (**C**) Example histological verification of GCamp7s expression and lens placement above CA1. (**G**) Inset of F detailing gfp expression in the pyramidal layer of CA1 (**D**) Example mean frame from a rat after motion correction. (**E**) Pseudo-colored contours extracted from the same recording as in C. (**F**) (Top) normalized calcium activity (deconvolved transients + denoised calcium trace) of 437 place cells from the recordings in D alongside (bottom) x-position of a rat running along the short path, either in the rightwards (red) or leftwards (blue) direction. Cells are sorted by their preferred firing location along the track and preferred direction of travel. (**G**) Normalized place fields of place cells in SAT (left), SSI+SAT (middle), and BOC (right) sessions across all animals, using place cells that recur between the day of interest and one of the pre/post sessions. Place fields within each manipulation group are sorted separately by each cell's preferred position and movement direction.

We developed an Event Induced Remapping Index (EIRI, see Figure 2.3.2.2) to quantify the extent of hippocampal remapping caused by the manipulations (shock or barrier introduction). This measures the magnitude of the decorrelation of the population vector across different locations of the maze. We specifically analyzed EIRI values for the unsafe location (the middle of the maze where shock/barrier was presented) from the safe location (where no manipulation occurs).

The degree to which place cell remapping was induced by shock and barrier presentations is shown in Fig. 2.3.2.2A, which plots EIRI values for the safe end regions of the short path (open symbols) and the unsafe center region of the short path (filled symbols). In the drug-free shock condition, the mean unsafe zone EIRI was significantly less than zero (t_{10}=-4.16; p=.002), and of the 11 individual rats that received drug-free shocks, 8 showed significant shock-induced remapping in the unsafe zone (defined as EIRI<-2), whereas zero showed significant shock-induced remapping in the safe zone. Interestingly, although the mean safe zone EIRI did not differ significantly from zero (t_{10}=1.78; p=.11), 4 rats showed significant drug-free shock-induced stability in the safe zone (defined as EIRI>2), whereas none of these rats showed shock-induced remapping in the unsafe zone. Place cell remapping in the unsafe zone could not be attributed simply to reduced traversal of the short path during the shock session, because the barrier manipulation (which also blocked traversal of the short path) did not produce similar levels of place cell remapping: the mean barrier EIRI did not differ significantly from zero in the unsafe (t_{5}=-.52; p=.62) or safe (t_{5}=1.42; p=.21) zones, and no individual rats exhibited significant barrier-induced remapping in either zone (although one rat showed significant barrier induced stability in the safe zone). These results indicate that drug-free shocks induced remapping of place cells in the unsafe but not the safe zone of the short path, consistent with findings from prior studies.
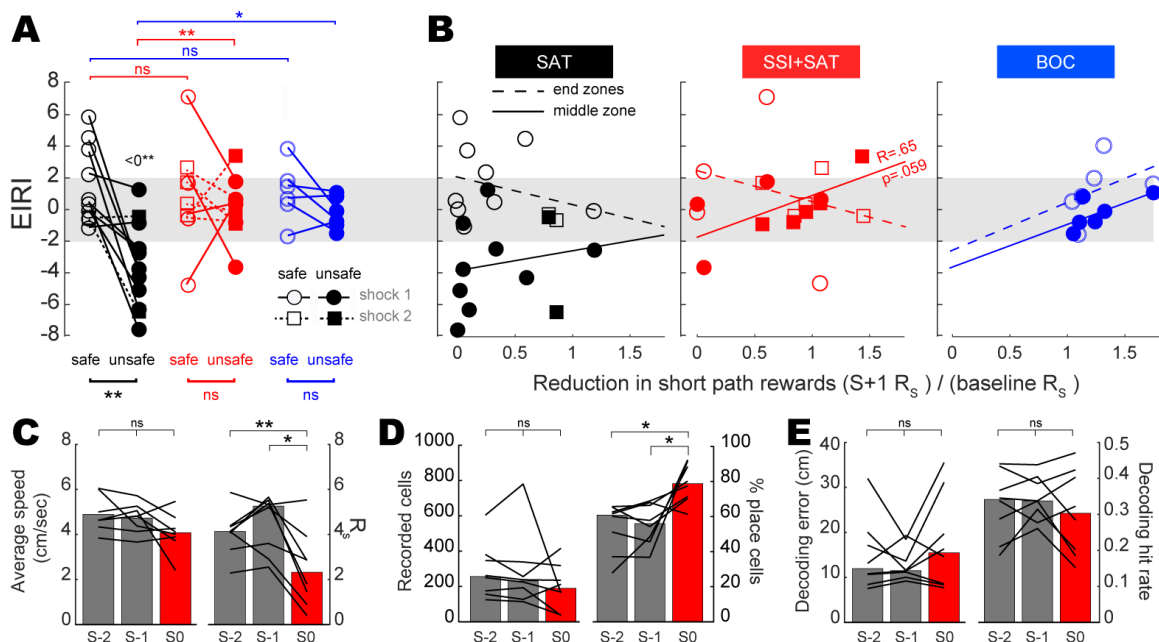
Figure 2.3.2.2. Scopolamine blocks the remapping effects of aversive learning while sparing spatial coding within the session. (A) Event Induced Remapping Index for all manipulations, split by location along the track (safe==ends, unsafe==middle). Significant decorrelation of the population vector in the unsafe zone was only seen in the drug-free shock manipulation. (B) EIRI scores in (A) regressed against short reward rate (R_s) in the session 48 hours after each manipulation. (C) Data from 8 rats on their first exposure to scopolamine (S0, red), as well as the 2 sessions prior (S-2 and S-1). (left) Effect of scopolamine on running and (right) R_s. (D) Number of recorded cells and percent of those cells classified as place cells after downsampling behavior to match the scopolamine session. (E) Within session decoding performance, showing the median distance (right) and classification accuracy for position bin (right).

Shock-induced place cell remapping was blocked by scopolamine. The mean EIRI did not differ significantly from zero in the unsafe (t_8=.18; p=.86) or safe (t_8=.76; p=.46) zones after shocks under scopolamine. Only 1 out of 9 rats showed significant shock-induced remapping after being shocked on scopolamine, and interestingly, this was one of the two rats for which scopolamine failed to block 48 h retention of shock avoidance (see Fig. 1h). Indeed, when the degree of shock-induced place cell remapping in the unsafe zone was regressed against 48 h retention of shock avoidance, rats that were shocked under scopolamine showed a strong trend toward a significant linear correlation (p=.059; Fig. 2.3.2.2B, center), suggesting that the degree to which scopolamine impaired remapping was correlated with the degree to which it impaired

avoidance learning. This correlation between 48 h avoidance retention and remapping did not approach significance in either zone (safe or unsafe) for any of the other event conditions.

Condition	safe	unsafe
SAT	R=-.3, p=.36	R= .18, p=.59
SSI+SAT	R=-.29, p=.44	R= .65, p=.059
BOC	R= .42, p=.40	R= .68, p=.13

Table 2.3.2 Full set of regression values for the safe and unsafe locations for all manipulations

A 3x2 ANOVA with event as an independent factor (drug-free shock, scopolamine shock, barrier) and zone as a repeated factor (safe versus unsafe) yielded a significant interaction effect ($F_{1,23}$=10.22, p=.0352). Post-hoc comparisons revealed that in the drug-free condition, the mean EIRI for the unsafe zone was significantly lower than for the safe zone (t_{10}=-4.16; p=.002), and this was not the case for the scopolamine shock (t_8=.56; p=.59) or barrier (t_5=1.71; p=.15) conditions. Moreover, the mean EIRI for the unsafe zone of the drug-free shock condition was significantly lower than for the unsafe zone of the scopolamine shock (t_{18}=-3.28; p=.004) or barrier conditions (t_{15}=-2.74; p=.015). A chi square test revealed that the proportion of rats showing significant shock-induced remapping was contingent upon drug condition (drug free vs scopolamine) in the unsafe center zone of the maze, χ^2(20)=7.6, p=.006.

All of these findings convergently support the conclusion that drug-free shocks (but not blocking the short path with a barrier) induced place cell remapping in the unsafe zone (but not in the safe zone), and that scopolamine blocked the ability of shocks to induce place cell remapping in the unsafe zone.

2.4 DISCUSSION

Here we have demonstrated that shock avoidance learning produces remapping of hippocampal place cell population vectors near the shock location, in agreement with prior studies that have shown place cells can remap their firing fields near locations where an aversive experience has occurred (Moita et al. 2003; Moita et al. 2004; M. E. Wang et al. 2012; M. E. Wang et al. 2015; E. J. Kim et al. 2015; Schuette et al. 2020). We also found that pre-training administration of systemic scopolamine blocked avoidance learning, in accordance with prior findings (Decker, Tran, and McGaugh 1990; Huang et al. 2011; Zhang et al. 2021), and concurrently blocked place cell remapping. A prior study has presented evidence that scopolamine can impair the formation of new place fields in a novel environment (Douchamps et al., 2013), but to our knowledge, the present study is the first to show that learning-induced place cell remapping is blocked by scopolamine. Within-session metrics of place cell fidelity--such as spatial information content, proportion of spatially tuned hippocampal cells, and within-session position decoding--were not significantly disrupted by scopolamine. Hence, scopolamine impaired remapping despite the fact that it spared many of the basic spatial tuning properties of hippocampal neurons. This supports existing theories and evidence (Green et al. 2005; Hasselmo 2006) that cholinergic projections to the hippocampus are necessary for storing new memories of novel experiences (which may occur during place cell remapping), but are less important for retrieving previously stored memories of familiar experiences (which may be reflected by stable spatial tuning of place cells).

2.4.1 Role of Acetylcholine in memory

Manipulations that impair cholinergic neurotransmission have been found to selectively impair memory storage but not retrieval of semantic information (Atri et al. 2004; Hasselmo and McGaughy 2004) or fear memories (Decker, Tran, and McGaugh 1990; Huang et al. 2011). Conversely, drugs that enhance nicotinic acetylcholine transmission have been found to improve memory capabilities (Buccafusco et al. 2005; Levin, McClernon, and Rezvani 2006; Shim et al. 2008; Echeverria and Zeitlin 2012), and drugs that upregulate acetylcholine are routinely prescribed to treat Alzheimer's patients (Lombardo and Maskos 2015).

Here, we found that pre-training scopolamine injections impaired 48 hour retention of shock avoidance learning, consistent with prior findings that scopolamine disrupts memory encoding (Saucier et al. 1996; Anagnostaras et al. 1999; Wallstein and Vago 2001). We also found that scopolamine-injected rats were able to avoid the short path during the immediate time period after receiving shocks, in agreement with prior evidence that scopolamine does not impair the avoidance of shock during the learning event itself (Kramis et al. 1975). In addition to disrupting encoding of avoidance learning, scopolamine also impaired expression of the rats' previously learned preference to take the short path between reward zones. It is unclear whether this deficit was attributable to an impairment of retrieval for a previously encoded memory that the short path is the best route between rewards, or instead to a motivational or attentional deficit of some kind. Cholinergic disruptions were previously shown to block retrieval of spatial memory in the Morris maze, and to disrupt working memory in a spatial task (Huang et al. 2011; Zhang et al. 2021). Hence, it is possible that while scopolamine tends to impair encoding more than retrieval for fear learning and avoidance tasks, it may impair memory retrieval (as well as encoding) for certain kinds of spatial navigation tasks.

2.4.2 Effects of scopolamine on hippocampal activity

Prior studies have shown that place cells in the hippocampus(Brazhnik et al. 2004; L. A. Newman and Gold 2016; E. L. Newman et al. 2017; Sun, Unnithan, and French 2021) and grid cells in the medial entorhinal cortex (E. L. Newman, Climer, and Hasselmo 2014) are mildly disrupted by scopolamine injections. Electrophysiological recordings of place cells under the effects of scopolamine show an increased out-of-field firing probability (Brazhnik et al. 2004) and a disruption of theta phase precession (E. L. Newman et al. 2017). Sun et al. recently performed calcium imaging in mice before and after scopolamine administration and showed a decrease in recorded cells, reduced spatial information, and a broadening of place fields along the linear track (Sun, Unnithan, and French 2021). Here, we recorded place cells from rats and observed rather different effects of scopolamine on place cells. We are currently looking into the precise differences, but initial results do not appear to show a decrease in spatial information, nor we do not see decreased decoding accuracy on scopolamine compared to off (Fig. 2.3.2.2E). Like previous research, we do not see a decrease in running speed, but we do see an impact on task performance (Figure 2.3.2.2C). Since scopolamine has been shown to impair retrieval for some spatial memories (Huang et al. 2011), effects of scopolamine on place cells may mirror its effects on memory retrieval and depend on task demands. Since our task does have spatial learning and decision making components (a dual choice at each lap start), it likely engages hippocampal circuitry more than typical linear alternation tasks (E. L. Newman et al. 2017; Sun, Unnithan, and French 2021).

From this previous evidence, it is assumed that this disruption of place cell encoding underlies the memory encoding failure caused by muscarinic blockade, but most research only addresses either the behavioral effects, or the physiological effects without a learning component. Here, we sought to bridge this research gap and evaluate how scopolamine

administration disrupts place cells, and how this disruption correlates with future memory retrieval performance after aversive learning.

2.4.3 Summary and conclusions

The hippocampus is only one of several memory-related brain structures that receives dense cholinergic projections. The amygdala (especially the basal nucleus) and striatum are also densely targeted by cholinergic projections. Since scopolamine was delivered systemically in the present study, drug-induced behavioral deficits may have resulted from impaired cholinergic transmission in several of these regions, in addition to (or instead of) the hippocampus. However, there is reason to expect that scopolamine's actions on the hippocampus were at least partly responsible for the impairments we observed.

CHAPTER 3: Miniaturized Microscope Development

Note: Chapter 3 is a manuscript in preparation from a collaboration between the Blair and Aharoni labs (Dr. Changliang Guo and Dr. Daniel Aharoni) at UCLA.

We present a wire/wire-free large field of view (LFOV), open-source miniature microscope (Miniscope) platform aimed at extending the capabilities of microendoscopy imaging approaches in large rodents and non-human primates, such as rats, marmosets, and macaque monkeys. The system can image a 3.2 mm × 2.5 mm FOV with ~2 μm resolution at 11 frames per second (fps)(~4 μm at 23fps), has an electrically adjustable focal length of ±150μm using an electrowetting lens, incorporates an absolute head-orientation sensor, and weighs only 14 grams. This system is capable of multiple imaging configurations including deep brain imaging using one or multiple implanted optical probes with 1.85mm working distance objective module, and cortical imaging through a cranial window with 3.5mm working distance objective module. Our large FOV Miniscope has been validated in freely behaving rats by imaging GCaMP7s expressing neurons in the CA1 layer of the hippocampus through two quarter GRIN lenses with 1.8mm diameter and cortical imaging through a 4×4 mm cranial window on head fixed mice. The LFOV Miniscope platform has also been extended for use in wire-free operation with an optional, on-board wire-free data acquisition expansion board and a 400mAh on-board, single-cell lithium-polymer battery. With a greater than 10-fold increase in FOV and detectable neurons than previous generation Miniscopes, we expect this imaging platform for freely behaving animals to generate qualitatively and quantitatively new data for neuroscience applications.

3.1 INTRODUCTION

Understanding how populations of neurons and the circuits they create give rise to complex behavior remains a key endeavor of systems neuroscience. Novel imaging tools combined with the development of new Ca^{2+} indicators have advanced the field by introducing the ability to monitor large populations of neurons simultaneously and track identified neurons for extended periods of time. Decades of neuroscience research has led to the development and refinement of optical techniques, such as two-photon microscopy (W Denk, Strickler, and Webb 1990; Winfried Denk and Svoboda 1997; R. Lu et al. 2020), light sheet microscopy (Keller, Ahrens, and Freeman 2015; Voleti et al. 2019), etc., to image the structures and functions of large neuronal networks with cellular or subcellular resolutions. However, such imaging devices are bulky and can only be used on restrained animals in head-fixed experiments, typically within virtual reality based environments (N. T. M. Robinson et al. 2020; Dombeck et al. 2010). This constrains experiments from being conducted in more naturalistic environments, which is particularly important for brain regions related to spatial navigation that depend on both sensory and proprioceptive information (Aghajan et al. 2015; Acharya et al. 2016; Ravassard et al. 2013). Single photon epifluorescence miniature microscopy (Ziv et al. 2013; Cai et al. 2016; Aharoni et al. 2019; Aharoni and Hoogland 2019; Shuman et al. 2020; Skocek et al. 2018; Liberti et al. 2017; Barbera et al. 2016; Jacob et al. 2018) circumvents this constraint while still achieving single cell resolution, and been used extensively to conduct neuronal imaging in freely behaving animals to reveal neural activity from learning and memory to neurological disorders and social interactions (Liang et al. 2018; Kingsbury et al. 2019).

Open-source head-mounted miniaturized epifluorescence microscopes, such as UCLA Miniscopes (Cai et al. 2016; Aharoni et al. 2019; Skocek et al. 2018; Aharoni and Hoogland 2019; Shuman et al. 2020; Kingsbury et al. 2019; Hart et al. 2020) and counterparts miniscopes (Liberti et al. 2017; Barbera et al. 2016; Jacob et al. 2018), have shown that wide-field

epifluorescence imaging could be achieved with miniaturized microscopes that are light enough to be mounted on the head of a rodent, and the neural signals can be extracted by further analytical techniques (Giovannucci et al. 2019; Zhou et al. 2018; Friedrich, Zhou, and Paninski 2017). Developments over the past decade have enabled these imaging techniques to be applied in unrestrained, freely behaving animals, expanding the repertoire of behavioral assays that can be used in conjunction with neural imaging.

However, the off-the-shelf commercial and open-source miniaturized microscopes designed for cellular imaging only have a smaller field of view (FOV≤1 mm^2) (Aharoni and Hoogland 2019; Groot et al. 2020; Düring et al. 2020), or have a large FOV at the cost of resolution performance, which is incapable of investigating the neural activities with cellular scale. This limitation precludes their applications in terms of monitoring multiple cortical areas, investigating the correlations and interactions between far away neurons (Sofroniew 2017; Rynes et al. 2021), and the neuronal activities that support sensory coding and motor output (Stirman et al. 2016), etc. In addition, the current miniature mesoscopic devices lack configurations for wire-free/wireless operation, hindering the conduct of experiments in terms of recording multiple animals in a group housing setting or recording on flying birds or bats (Barbera et al. 2019; Yartsev 2013; Yartsev and Ulanovsky 2013; Bollimunta et al. 2021).

Here we report a head-mounted Large Field of View (LFOV) Miniscope based on UCLA Miniscope platform, allowing widefield imaging of CA1 in hippocampus of the rat using 2mm/1.8mm gradient refractive index (GRIN) relay lenses (FOV=~3.14 mm^2) and of cortex of mice (FOV=~8 mm^2) with single cell resolution (~ 2 μm). This Miniscope has an electrically adjustable working distance (WD) +/-150 μm using an electrowetting lens (EWL) (Corning Arctic 58N, Varioptics/Corning), and incorporates an absolute head-orientation sensor (Bosch BNO055). The whole body is around 35mm tall and weighs around 14 grams. With two WD configurations (WD of 1.85mm and 3.5mm) this device can be easily swapped by just changing

the objective module of the miniscope, which is attached to the emission module by screws. Swapping between the two WD configurations, this device enables multiple applications including cortical imaging through a cranial window and deep brain imaging using one or multiple implanted optical probes, such as a relay optics made of Gradient-Index (GRIN) lenses. Furthermore, we also developed a small, wearable wire-free data acquisition (DAQ) expansion board (wire-free DAQ, ~3g) which adds wire-free capabilities to any standard wired Miniscopes. The wire-free DAQ is battery powered by an on-board, single-cell lithium-polymer battery (3.7V 400mAh, ~7g) and logs imaging and head-orientation data onto an on-board MicroSD card. This wire-free DAQ can be mounted directly onto the LFOV Miniscope's housing or be worn as a backpack. Power, video streams and I2C commands transmission between the miniscope and wire-free DAQ are connected with a shot coaxial cable with two Hirose U.FL Connectors (U.FL-PR-SMT2.5-1(10)) on the ends.

The large FOV Miniscope has been validated in freely behaving rats by imaging GCaMP7s expressing neurons in the CA1 layer of the hippocampus on a linear track (wired recording) and open field circular maze (wire-free recording). The 3.5mm WD setup is validated with cortical imaging on head-fixed mice. With a greater than 20-fold increase in FOV and detectable neurons than previous generation Miniscope (700×450 μm), we expect this imaging platform for freely behaving animals to enable immense opportunities for new neuroscience applications. Increasing the yield of neurons recorded simultaneously continues to generate novel discoveries about brain function, particularly when activity is encoded within a small, specialized subset of the population (Harvey, Coen, and Tank 2012; Gauthier and Tank 2018; Mau et al. 2018; Rubin et al. 2019; Hart et al. 2020). With the added benefit of low-cost (compared to bulky microscopes) and open-access resourcing, this device enables broad and easy access by new users, groups, and labs with limited funding support. Importantly, the LFOV Miniscope builds on the already widely adopted open-source UCLA Miniscope ecosystem, and

51

has the potential applications for large-scale recordings of neurons in bigger animals, such as rats, bats, and non-human primates (Ebina et al. 2018; Kondo et al. 2018; Sarel et al. 2017).

3.2 RESULTS

3.2.1 System Design

The miniscope (Fig. 1a) consists of three structured modules, i.e., objective module, emission module, and sensor module, to hold the optical components and custom circuit boards. The modules are designed in Autodesk Fusion 360 (education version) and printed with black resin (FLGPBK04) by a 3D printer (Form 3, Formlabs) to produce lightweight, compact, and low-cost assembly. The circuit schematic and pcb layout are designed using Kicad, a free software suite for electronic design automation (EDA). The circuit module consists 4 PCB circuits, i.e., LED PCB, which has two LEDs capable of independent or synchronized illumination into the brain, BNO055&EWL driver PCB for head orientation collections and electrowetting lens tunings, imaging sensor PCB for collecting neuronal imaging data, and serializer PCB (Fig. 1a, b). The four PCBs are connected by flex PCBs. Integrated with a head orientation chip (BNO055, Bosch Sensortec), the LFOV Miniscope enables the collection of quaternions of the head movement, euler angles, rotation vector, linear acceleration, and gravity, etc., which helps to investigate head orientation related neural mechanisms (Angelaki et al. 2020; Sargolini et al. 2006; Gerlei et al. 2020; Solstad et al. 2008).

The objective module (Fig. 1c) has 3 chromatic lenses in it and the emission modules (Fig. 1d) holds the excitation filter, dichroic mirror, emission filter, one aspherical lens and a concave lens. The sensor module is designed for holding the electrowetting lens and CMOS sensor (Fig. 1b). The main modules are screwed together with two types of screws, M1 thread-forming screws (96817a704, McMaster-Carr) and 18-8 Stainless Steel Socket Head Screw, 0-80 Thread Size (92196A052, McMaster-Carr).
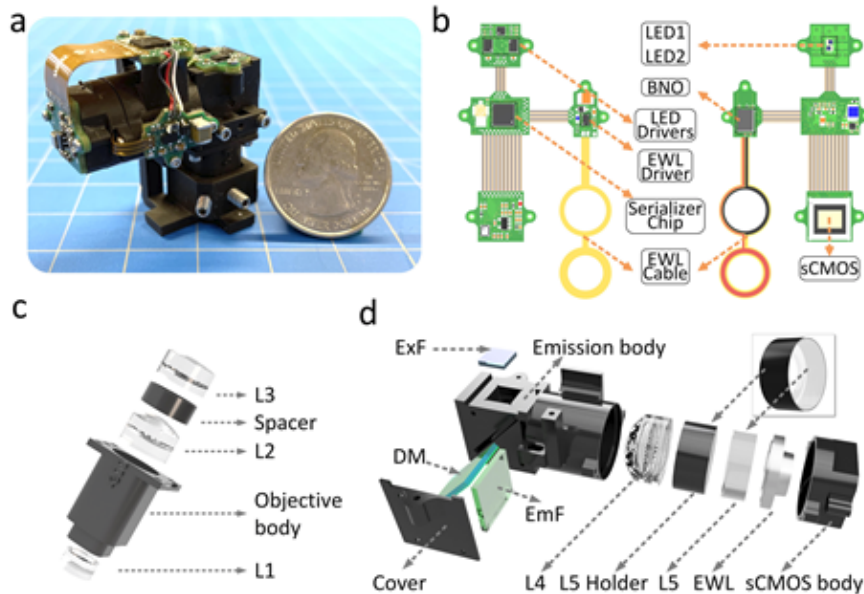
Figure 3.2.1. Design of Large FOV miniscope. (a) Photograph of LFOV miniscope with baseplate. (b) Electronic PCBs of LFOV miniscope includes CMOS senor, serializer, dual-LED, and EWL&BNO boards with rigid flex pcb connected for I2C command and data transmission. Circuit module consists of four main pcb boards, LED pcb, EWL&BNO pcb, sCMOS pcb, and Serializer pcb. Two leds are soldered on to led pcb board driven by two led drivers and I2C digital potentiometer for brightness adjustment. EWL&BNO pcb has EWL driver, with EWL cable holding the EWL, to adjust the focus of the EWL and BNO head orientation chip for collecting head orientation data. 5M sCMOS sensor (MT9P031) is soldered on the sCMOS pcb for Ca++ fluorescence image capturing. Serializer chip on the serializer board transfers the parallel data set from sCMOS to serial data with a coaxial connector soldered to communicate with UCLA DAQ board. (c) Objective module of the miniscope. Objective module contains a 3D printed body to hold the components and three achromatic lenses (L1, L2, and L3) with a spacer between the second and the third lens on the top. (d) Emission module of miniscope. Emission module consists of 3D printed bodies (a cover, a L5 lens holder, and a CMOS holder) to hold the filters, lenses and CMOS sensor, and optics components. Optics group refers to filters (excitation filter (ExF), dichroic mirror (DM), and emission filter (EmF)), optics lenses (achromatic L4 and plane-concave lens L5), and electrowetting lens (EWL).

The LFOV Miniscope interfaces with the open-source Miniscope DAQ Software to stream, visualize, and record fluorescence and behavioral data. The software enables multiple miniscope and behavioral camera video streams, allowing for multi-animal neural and behavioral recording. The data acquisition (DAQ) device hardware and software are based on "Miniscope" project (http:// miniscope.org/index.php/Main_Page), with updated firmware and software to enable the video streaming and I2C controlling on the large FOV Miniscope, including LED brightness adjustment, focus change by the electrowetting lens, frame rate selection, and setting the gain of the sensor.

Accessories of the Miniscope also include a reinforced 3D printed baseplate, attached to the skull with dental/bone cement which allows consistent mounting of the Miniscope, as well as a protective cap to protect the brain and GRIN lens after experiments.

3.2.2 Optics performance

The optics of the system was designed and optimized using OpticsStudio (Zemax). The layout of optical components and the imaging path are shown in Fig. 3.2.2.1a, d e and eg. The optics path includes excitation path and emission path. The excitation path and emission path are separated by a Dichroic mirror (T500spxr, Chroma), and an Emission filter (ET525/50m, Chroma) is placed in the emission path to filter the possible leakage from the excitation path. The high resolution of the system and large Field of view are achieved by using 5 off-the-shelf lenses from Edmund optics (3 achromatic convex lens, 1 aspherical achromatic lens and 1 concave lens), by optimizing the distance and sequence between them. The achromatic lenses are adopted to minimize the non-chromatic aberrations. The optical path is folded by a dichroic mirror in the middle to lower the center of mass (Fig. 3.2.2a , g, and e). The designed field curvature of the optics in objective space throughout 3mm FOV is around 130 µm. The optical system also enables an adjustable WD with +/- 150 µm in the object space with an electrowetting lens (Corning Arctic 58N), driven by (MAX14515, Maxim), placed before the sCMOS sensor. The WD of the system is designed to be 1.8mm (Fig. 3.2.2d, e). The 3.5mm configuration (Fig. 3.2.2.1f, g) uses L1, L2-2, and L3-2. 3.5mm WD is designed for imaging the ROI which is further away from the Miniscope, such as the cortex imaging through a cranial window. The related OTF reaches zero when x axis gets around 450 cycles/mm, i.e., 1.4 µm in the object space. 3.5mm WD (right) has RMS radius 2.486 µm at the center and 3.009 µm at (0, -1.5mm) and (0, 1.5mm). The magnification is around 1.57.
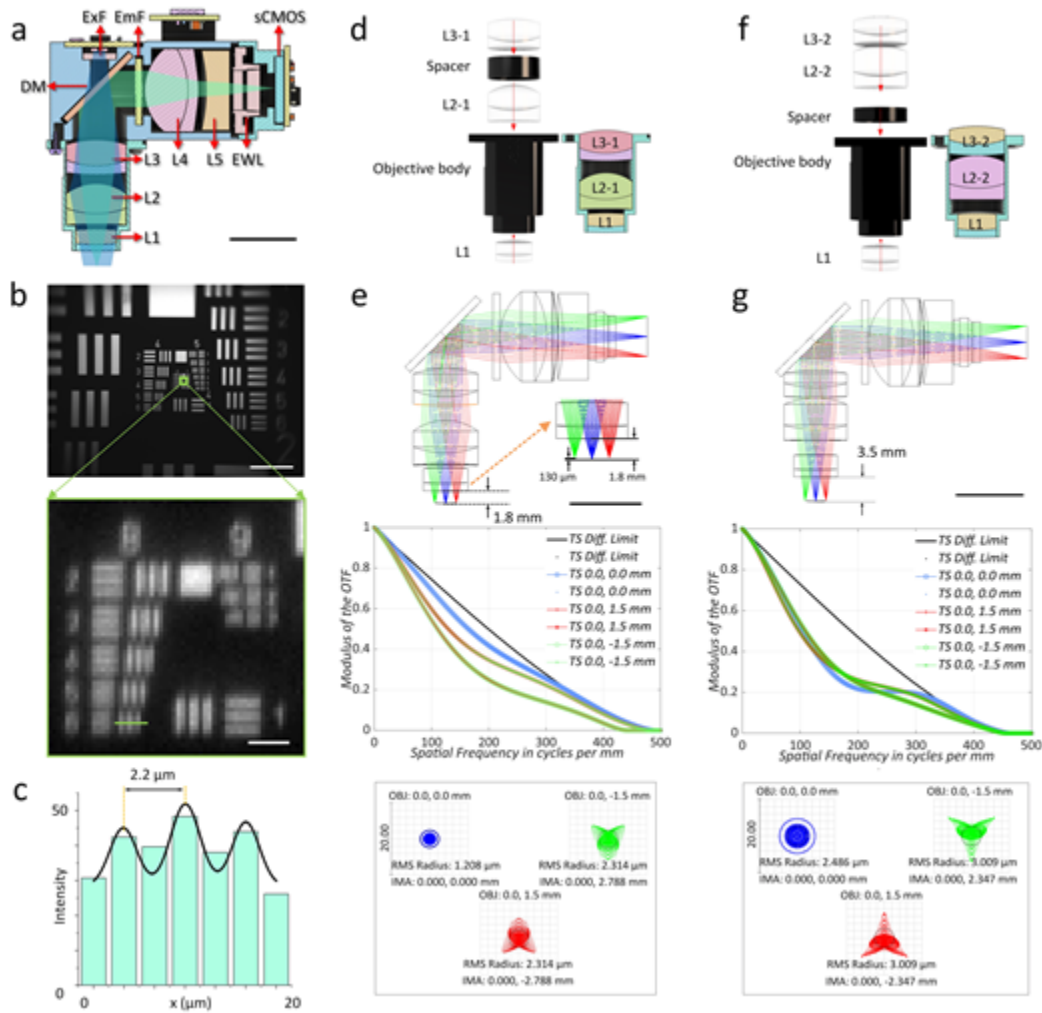
Figure 3.2.2.1 Optics design and Large FOV Miniscope and optical performance. (a) Cross section of the miniscope assembly, showing the optical components inside the body, including an objective module with 3 achromatic lenses (L1-L3), emission module with 1 achromatic lens (L4), 1 concave lens (L5), and 1 electrowetting lens (EWL). It also includes an excitation filter (ExF), Dichroic mirror (DM), and emission filter (EmF). Excitation path from 2 leds is highlighted with blue color and emission path by green color. Scale bar: 1mm. (b) The FOV, i.e., ~3.25 mm×2.5 mm is tested with Negative Combined Resolution and Distortion Test Target (R1L1S1N, Thorlabs). Scale bar: 500 µm(top), and 10 µm(bottom). (c) 2.2 µm or 456 lines pair per mm can be resolved by experimentally testing it with the Test Target. (d) 1.8 mm WD is used for deep braining imaging, in which the miniscope can be placed closer to the relay optics to lower the center of mass, reducing the difficulty when the rats are carrying the device. (e) Zemax simulation of emission path shows the WD (1.85 mm) with 130 µm field curvature in the object space (top), modulus of the OTF of the three potions on the image plane (middle), and spot diagram of the optics (bottom). The value of this function reaches zero when x gets 500 cycles/mm, i.e., 2 µm, at the image plane, which predicts the resolution of the system, ~1.1 µm in the object space. As shown in the spot diagram of the optics at the image plane, RMS radius is 1.208 µm at the center and 2.134 µm at (0, -1.5mm) and (0, 1.5mm). The magnification of the optics is given by 2.788/1.5=1.86 three object points, (0, -1.5mm), (0, 0mm), and (0, 1.5mm) along y axis. The images of the points are focused at (0, 2.788mm),(0, 0mm), and (0, -2.788 mm) on the sCMOS sensor. (f) 3.5mm WD is designed for imaging the ROI which is further away from the miniscope, such as the cortex imaging through a cranial window. It is configured by using the same L1, and two new achromatic lenses, i.e., L2-2, and L3-2,. (g)) Zemax simulation of emission path shows the 3.5mm WD (top). The OTF reaches zero when x axis gets around 450 cycles/mm, i.e., 1.4 µm in the object space (middle). 3.5mm WD (right) has RMS radius 2.486 µm at the center and 3.009 µm at (0, -1.5mm) and (0, 1.5mm). The magnification is calculated by 2.348/1.5=1.57 (bottom).

In order to collect the enlarged FOV, a commercial 5M monochromatic sCMOS sensor (On Semiconductor MT9P031) with 2592 × 1944 pixels of 2.2 µm pixel size. The optics of the system enables 3.2 mm FOV in diameter, but the FOV is limited by the row number of the sensor, achieving 3.2 mm × 2.5 mm instead, validated by imaging the Negative USAF 1951 Hi-Resolution Target (#55-622, Edmund optics)fluorescence brain slide in hippocampus (Fig. 3.2.2.1b). Drived with a 66.667 MHz clock oscillator (EPSON), the sensor runs at 10fps 11fps at full resolution, running around 23fps after binning and summing the pixels 2×2, and it also enables 30fps with 96MHz clock oscillator.

With a magnified configuration, i.e., M=1.86 (Fig. 3.2.2.1e), the system aims for Ca^{2+} imaging with high resolution performance. The theoretical NA is chosen to be 0.25 at the object space. As shown in Fig. 3.2.2.1e, the MTF curves and spot diagram, at the image plane, the optics can resolve ≤2 µm throughout the whole FOV (3 mm in diameter) theoretically, which highly fits the requirement for resolving single neurons in the brain of rodents. The actual resolution is compromised with the pixels size of the sensor with the magnification of the system considered. The measurable resolution is given to be 2.2 µm, or 456 lines pair per mm (Fig. 3.2.2.1b, c), tested using a Negative USAF 1951 Hi-Resolution Target (#55-622, Edmund optics). In order to excite large FOV with unreduced light power to activate Ca^{2+} indicators, two LUXEON Z BLUE LED (470 nm, LXZ1-PB01), driven by 2 led drivers, are adopted in the excitation path with an Excitation Filter (ET470/40x, Chroma) placed right below the LEDs to narrow their spectral band. This design also permits the potential of the system for two-color fluorescence excitation. The LFOV Miniscope weights around 14 grams, therefore we expect two LFOV Miniscopes (28 grams) can be mounted onto the brain for multi-region imaging simultaneously on rats or bigger animals. Power, communication, and data transmission are achieved through a flexible coaxial cable (50Ω, CW2040-3650SR, Cooner Wire) in communicating with the supporting hardware (TI DS90UB913A/DS90UB914A). With a total

cable diameter down to 0.3 mm (Molex 100065-0023) and compatibility with passive, low torque

commutators, this design minimizes the impact of cabling on animal behavior. Details of the

coaxial cables are given in (U.FL Coax Cable Soldering,

https://github.com/Aharoni-Lab/Miniscope-v4/wiki/Assembly).

3.2.3 Imaging place cells in CA1 hippocampus

Studies of the neural representations of space have been prominent ever since the

discovery of place cells in the 1970s. Pyramidal neurons within the dorsal hippocampus of rats

respond when the animal occupies a particular location within the environment (J. O'Keefe and

Dostrovsky 1971; John O'Keefe 1976). The CA1 cells were then called place cells, which

motivated the proposal that the hippocampus makes an internal map of space, are considered

crucial for spatial memory in freely moving animals (Ziv et al. 2013; John O'Keefe and Nadel

1978). This map is specific to a context, and when an animal is moved to a different

environment these place cells will alter their place fields, a phenomenon known as "remapping".

The capability of fluorescence microscopy to record cells consistently across weeks

demonstrated that remapping occurs within the same static environment (Ziv et al. 2013) and

serves as a means of separating memories that occur within the same context but at different

times (Cai et al. 2016; Mau, Hasselmo, and Cai 2020).

Current miniaturized microscopy techniques enable imaging ≤1mm^2 FOV, but in animal

models larger than mice this size tends to limit the total number of recorded cells. This small

population sampling would not be as bad of a problem if the function of cells within a region is

homogenous. However, place cells represent different locations within a context, and recent

studies of hippocampal activity have further demonstrated unique properties within certain

subsets of place cells which were only possible to detect with large population recordings

(Geiller et al. 2017; Gauthier and Tank 2018; Soltesz and Losonczy 2018). Furthermore, any

function that depends upon recording the same cell across long timescales (such as remapping among place cells) benefits from a larger cell yield since this increases the intersecting population of cells across sessions.

3.2.3.1 Linear track behavior

Recordings took place in a rectangular linear maze, as described previously in Chapter 2 (2.5m × 1.5m; Fig. 2e), with two reward feeders on two corners of the track, controlled by a computer running Neuralynx Cheetah software feeding position information to custom MATLAB scripts which controlled pellet delivery as the rat ran from one reward zone to the opposite. Rats performed a two-armed bandit task, where two paths (2.5 and 5 meters total) connect the two reward zones. Since each path is equally rewarded, rats quickly learn to choose the short path preferentially over the long path to maximize reward. Since the short path has the best sampling for all sessions presented here, the long path data is omitted. Since place cells along a track are directionally specific, place fields are presented as a function of position and movement direction.

3.2.3.2 Surgical procedure

15 Rats (7M, 8F, Charles river) were used starting at 3 months of age. Rats for this experiment were also used in Chapter 2. In order to record place cell activity from the dorsal CA1 region, 1.2 uL of AAV9-Syn- GCaMP7s was injected just below the pyramidal layer (-3.6 AP, 2.5 ML, 2.6DV). A week later, two stacked quarter-pitch Gradient Refractive Index (GRIN) lenses (1.8mm diameter, NA 0.55, #64-519, Edmund optics) are surgically implanted above CA1 region after aspiration of the overlying cortex to generate a half pitch relay optics from CA1 region to the position above the surface of the second GRIN lens on the top outside the brain (Fig. 3.2.3.1a). Three weeks later, that rat was again placed under anesthesia and the LFOV Miniscope was mounted in the baseplate with two set screws, then positioned above the

implanted lenses and cemented in place with bone cement (Fig. 3.2.3.1b). The baseplate body

is 3D printed (by 20mm × 20mm outer dimensions) with 2 set screw holes on the side for set

screws (4-40 x 1/4"). The two Stainless set screws (4-40 x 1/4") are used to hold the cap in the

baseplate when not recording (protecting the GRIN lens and surgical region), and the Miniscope

body during experiments. An overview of installing and removing the Miniscope is shown in

Supplementary Fig. S3. With around 20 grams weight with Miniscope, baseplate, and the

cement, the rats can easily wear the whole device without any difficulty when they are running

(Fig. 3.2.3.1b). A red tracking LED is attached on top of the Miniscope body for tracking the

position of the rats during experiments.

3.2.3.3 Recordings with LFOV on a linear track

For the experiment, we imaged Ca^{2+} dynamics in GCaMP7s-expressing neurons in

dorsal CA1 of 15 rats while they performed a dual choice linear maze task. Fig. 3.2.3.1c shows

the maximum projection image from 15-mins motion corrected video of CA1 captured by

Miniscope of one rat where. The raw video is 972×1296 pixels after binning the pixels 2×2, then

further cropped to the ROI surrounding the GRIN lenses (around 761×761 pixels). During this

session on one rat for 15 mins recording, a total number of 1326 cells are detected and

extracted from CNMF-e analysis via CaImAn pipeline (Zhou et al. 2018; Friedrich, Zhou, and

Paninski 2017), color coded according to preferred trajectory within the environment, see Fig.

3.2.3.1d. The behavioral data in terms of positions on the track (Fig. 3.2.3.1f) and the head

orientations (Fig. 3.2.3.1g) of the rat on the track are extracted from the behavioral camera and

head orientation chip, which can be synchronized to give more accurate estimations of the

behavioral activities of the animals for further data analysis with the neural activities. 25

example cells are chosen to show the neural traces (Fig. 3.2.3.1h).
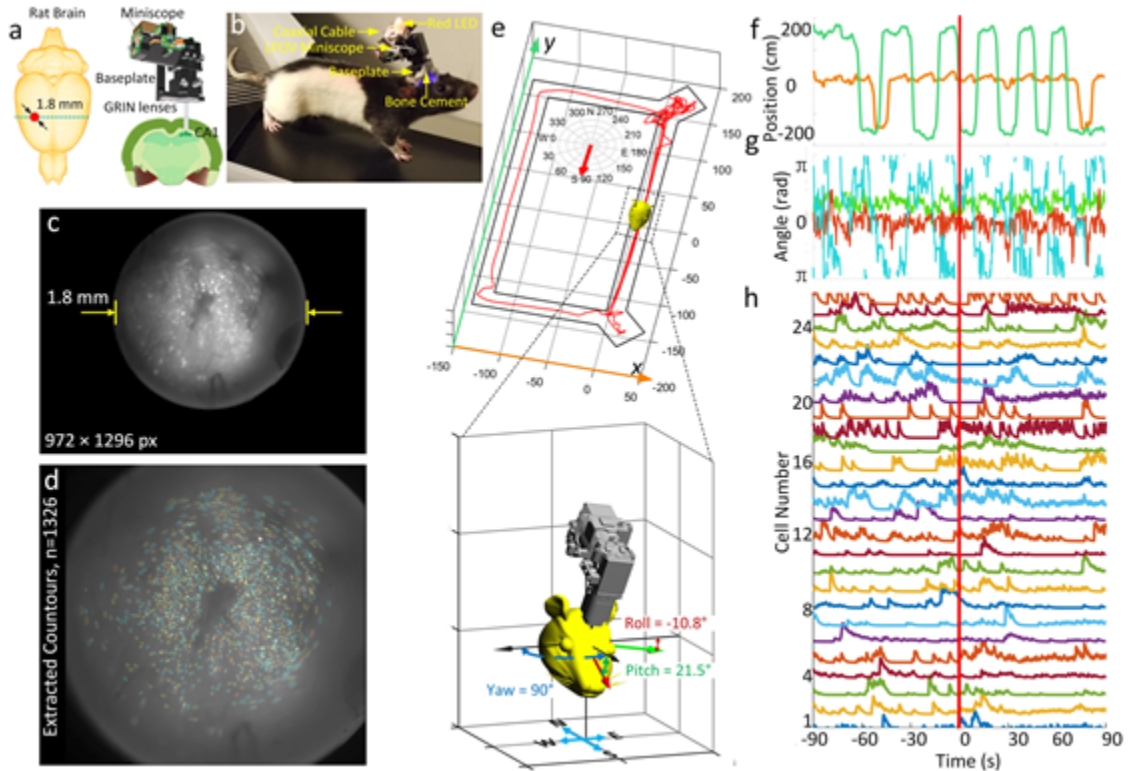
Figure 3.2.3.1. Strategy for imaging Hippocampus CA1 region in rats. (**a**) Schematic of the imaging area on the rat brain. Two GRIN lenses (quarter pitch, 1.8 mm in diameter) are implanted into the brain to relay the fluorescence expression from CA1 to the intermediate image plane under the LFOV miniscope. (**b**) Rat with LFOV miniscope mounted on its brain via a baseplate, for the duration of the recording session. (**c**) Max projection from a 15 minute recording session after motion correction. (**d**) Contours of extracted cells from CNMF-e analysis via CaImAn, colored according to preferred trajectory within the environment. (**e**) A rat with LFOV miniscope mounted running on a Rectangular track with two reward feeders. Zoomed-in figures show the Roll, Pitch, and Yaw values when the rat is passing y=0, running from north to the south. (**f**) X and Y position components as the rat runs in a 2D environment (**g**) Head orientation in terms of the Roll, Pitch, and Yaw values. Top: X and Y position components as the rat runs in a 2D environment. (**h**) calcium traces for 26 example cells recorded during the session within dorsal CA1.

As expected from recordings of place cells within a linear track environment, we found

that a significant population of the recorded cells were spatially tuned along at least one

direction of the track (McNaughton, Barnes, and O'Keefe 1983; Ziv et al. 2013; Sun, Unnithan,

and French 2021). Place cells were defined by having greater spatial information, given by its

bits/transient (Skaggs et al. 1993), then 500 resampled randomly shuffled transients for each

cell, and that each cell fired on at least 20% of all passes along the trajectory. Place fields along

each direction are shown for these 2131 place cells, sorted by their peak firing location (Fig.

3.2.3.2a). Spatial information content for 3455 recorded cells (2131 place cells, 1324 non-place

cells) is given in Fig. 3.2.3.2c. Within session place field correlations of the same cells are

shown in Fig. 3.2.3.2d, which is the correlation of place fields computed from randomly splitting

half the journeys along a trajectory and correlating these place fields. This demonstrates the first

recording of place cells from the rat hippocampus using in-vivo single-photon endoscopy.
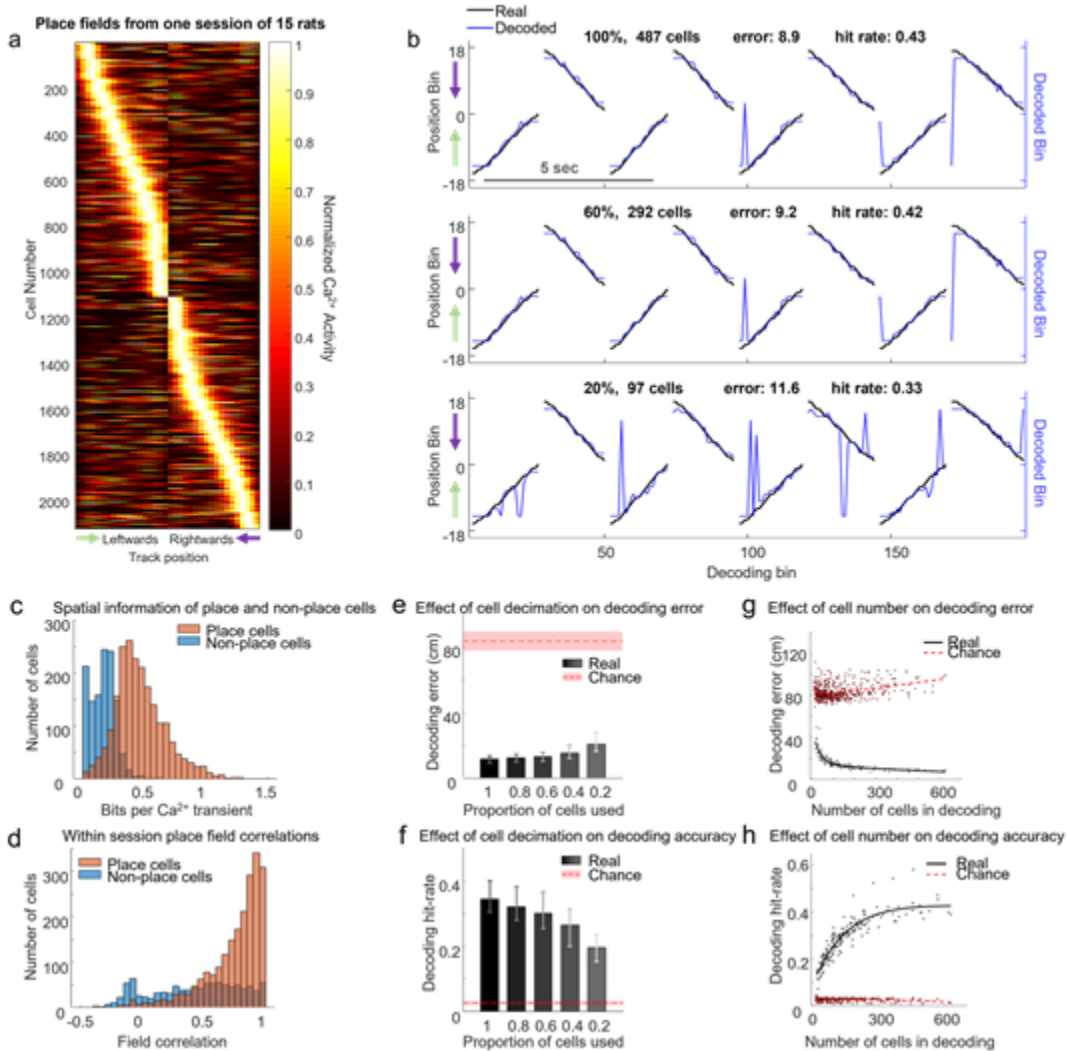
Figure 3.2.3.2. LFOV Miniscope single session performance. (a) Place fields of place cells from one session across 15 rats (n = 2131). (b) Demonstration of how the number of cells used in decoding affects accuracy from one animal using (top) 100% of recorded cells, (middle) 60%, or (bottom) 20%. (c) Spatial information content for 3455 recorded cells (2131 place cells, 1324 non-place cells). (d) Within session place field correlations of the same cells as in c. (e) Average error in centimeters from a Bayesian decoder using varying proportions of recorded cells. (f) Hit-rate of the Bayesian decoder using varying proportions of recorded cells. (g) Average error in centimeters from a Bayesian decoder as a function of cell number used. (h) Hit-rate of the Bayesian decoder as a function of cell number used.

61

Next, we sought to demonstrate the benefit this LFOV system has from recording large cell populations and how this benefits decoding accuracy. We performed positional decoding using a naïve Bayesian approach from one session across 15 rats (n = 2131, Fig. 3.2.3.2a). Fig. 3.2.3.2b shows the decoding accuracy from one animal using (top) 100% of recorded cells, (middle) 60%, or (bottom) 20% of cells respectively. Across all animals, decoded position was always better than expected from chance. Higher decoding error and low hit rate are found when a smaller number of cells are used for decoding, and this performance improves with greater cell inclusion (Fig. 3.2.3.2e-h). This data demonstrates how this imaging system is capable of improving experimental efficacy by yielding more cells, broadening the horizon of potential hypotheses for researchers.

3.2.4 Imaging CA1 hippocampus across sessions

Next, we sought to demonstrate that the LFOV miniscope is capable of consistently recording activity from the same population of cells across multiple sessions. Three imaging sessions were performed in the same task as above with two days separating each recording. Rats had previous in the task, and sessions were taken from when behavior performance was stable. Mean frame projection is shown in Fig. 3.2.4a for one rat, and extracted contours from this rat across the 3 sessions are shown in Fig. 3.2.4b. Contours from these sessions were first manually aligned using contours and vasculature, then processed with CellReg to register cells across all sessions based on their centroid distances and spatial contour correlations (Sheintuch et al. 2017). The distribution of centroids of all possible cell pairs within 24 microns are given in Fig. 3.2.4c, showing a large population of cell pairs within the same location after across-day alignment. Distributions of centroid distances and spatial correlation for all cell pairs within 24 microns were computed, yielding a two-dimensional distribution that can be modeled and given a probability threshold to match cell pairs. Cell pairs with a probability >.5 for both the

centroid and correlation distributions were matched (low centroid distance and high spatial

correlation), which is expected when recording the same cell.
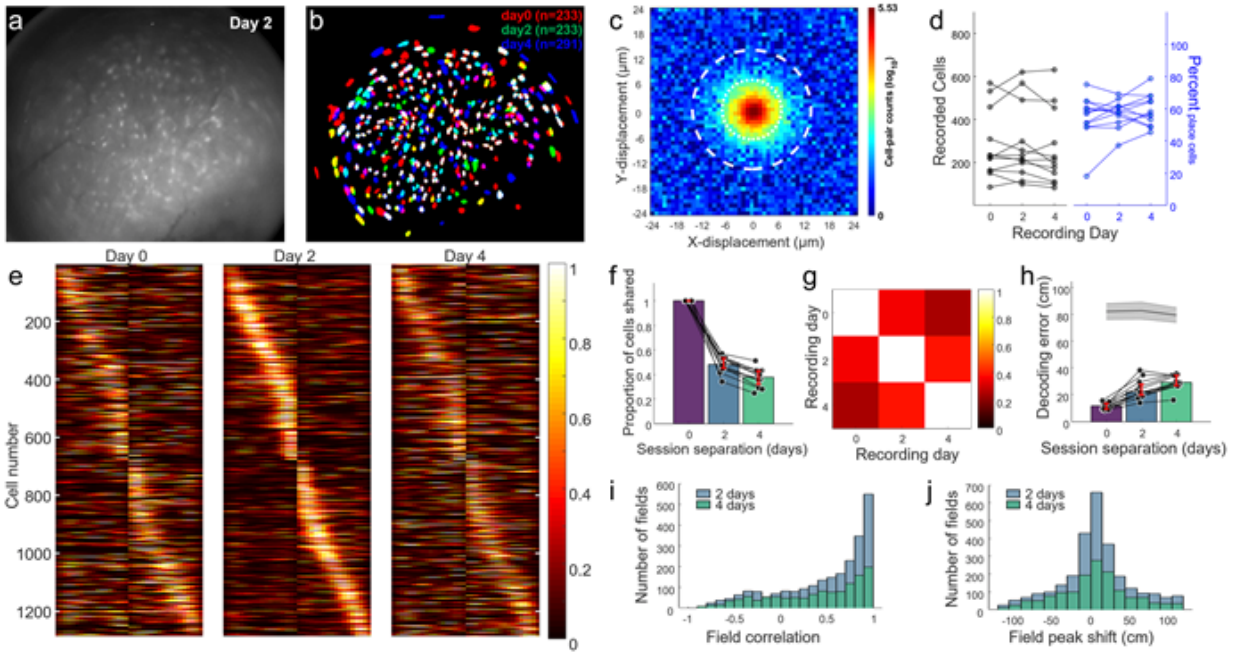
Figure 3.2.4. LFOV Miniscope can reliably record cells across multiple sessions. (a) Mean frame for day 2 recording for animal Hipp36. (b) Contours from all three recording days from animal Hipp36, colored by the recording day (0=red, 2=green, 4=blue). Cells which overlapped between sessions were matched as the same cell in both sessions. (c) Distribution of centroid displacements for all cell pairs within a 24 micron radius. (d) Number of cells (left) and percent place cells (right) on each recording day for all rats. (e) Place fields for 1295 cells from 12 rats across three recording days, sorted by their peak firing location on day 2. (f) Population overlap between recording sessions. (g) Average population vector correlation between recording days. (h) Bayesian decoding error as a function of recording separation; grey shaded area denotes mean+/-standard deviation of the random chance decoding performance. (i) Place field peak shifts of place cells in sessions recorded 2 (blue) and 4 (green) days apart. (j) Place field correlations for place cells in sessions recorded 2 (blue) and 4 (green) days apart.

  The number of recorded cells, and proportion of place cells, was consistent across these

recording sessions (Fig. 3.2.4d). Cells that were identified and matched on all three recordings,

and classified as a place cell on at least one session, shown in Fig. 3.2.4e, sorted by their peak

firing position on Day 2 and normalized by their maximal rate across all days. Population

overlap (the number of cells shared between sessions) and the average population correlation

vector between sessions decreased as a function of time (Fig. f-g). Decoding error increased

similarly, even when maintaining the same number of cells used in decoding , but was still much

better than would be expected from chance. However, many place cells still had high place field

correlation across both 2 and 4-day separations (Fig. 3.2.4i), and had low place field peak firing

distances (Fig. 3.2.4j).

3.2.5 Imaging cortical activity in head fixed mice

With 3.2 mm × 2.5 mm FOV and single cell resolution, this device is capable of cortical

imaging on head-fixed mice, freely moving rats, and bigger animals. Here, we validated the

capability of recording from the entire FOV by imaging the cortex region in head-fixed mice with

the 3.5mm WD configuration as shown in (Fig. 3.2.2.1f, g). The skull of the mice is replaced by a

4mm × 4mm cranial window during surgery and the head bar is affixed to the skull of the mice

with dental cement. During the experiment, the mice are placed on the running wheel (22.9 cm

in diameter) and then affixed to the head bar which is stabilized on the platform during

recording. The LFOV miniscope is attached to the miniscope holder with three translation

stages to adjust the lateral position and height of the miniscope above the cortex to get the best

ROI for imaging (Fig. 3.2.2.2a). A behavior camera (MiniCAM) is also developed with 16 red

LEDs (LTST-C190KRKT, Lite-On Inc.) on a LED Ring PCB board for behavioral recording46.

The brightness of the LEDs can be adjusted by the software for the best illumination in a dim

environment. MiniCAM runs at around 50fps with 1024×768 resolution (Fig. 3.2.2.2b). The

running wheel is 22.9cm in diameter with 1cm dark and white bars on the wheel (Fig. 3.2.2.2b)

for running speed estimation.
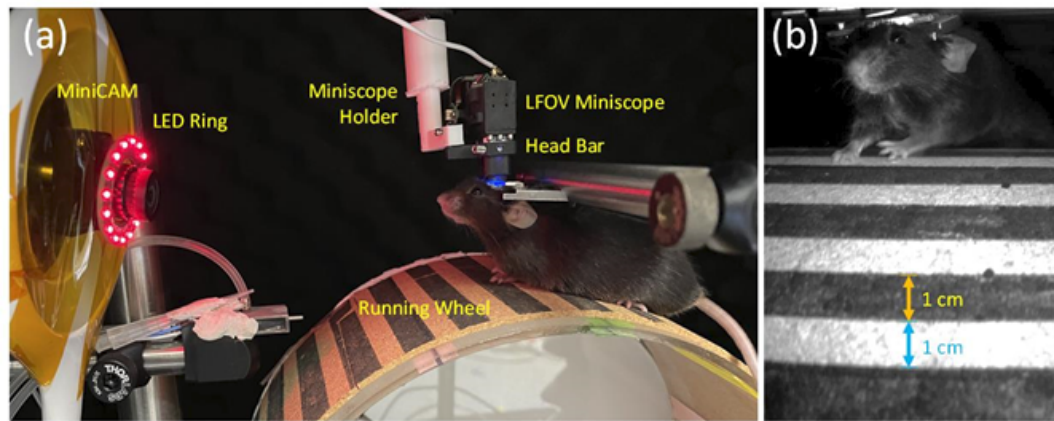
Figure 3.2.5.1 Ca+ imaging in Cortex through cranial window on head fixed mice. (a) Experimental setup. The mice are head fixed on the head bar with screws on a running wheel. The diameter of this wheel is 22.8cm and the distance between white and dark bars are 1cm. Miniscope is placed above the brain with an adjustable mount and adjusted to focus onto the cortical window. MiniCAM is used to capture the running speed of the mice with an LED ring for illumination in a dark environment. (b) Single frame taken by MiniCAM.
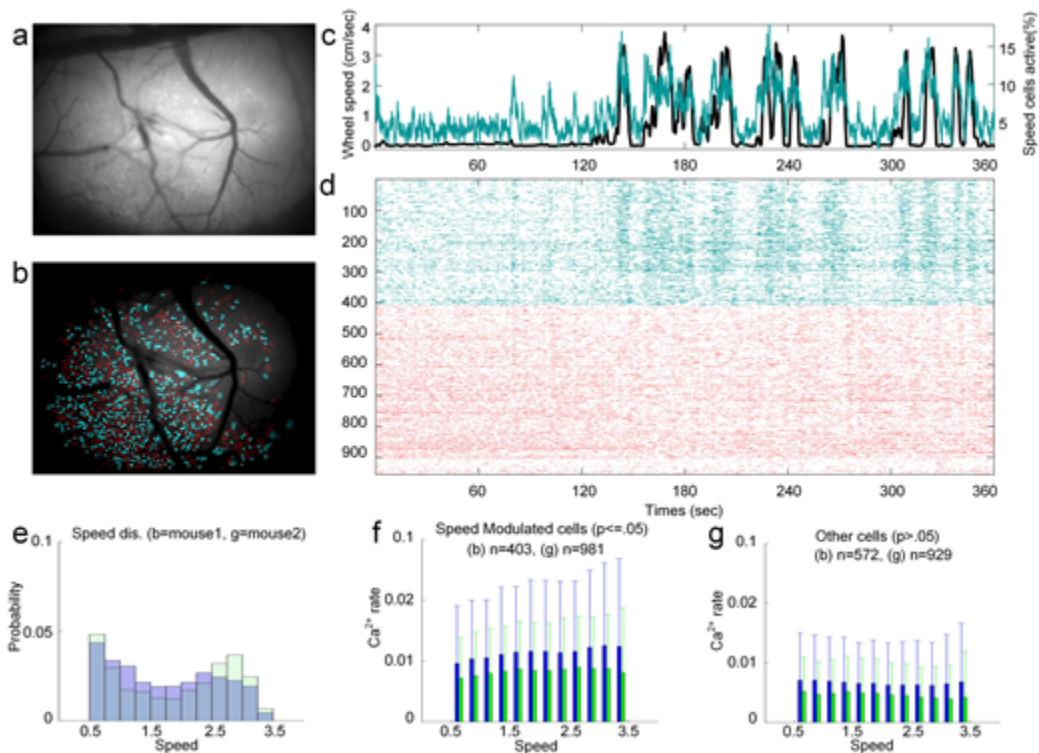
Figure 3.2.5.2. Ca+ imaging of cortex through cranial window on head-fixed mice. (a) Still image of the entire FOV from one mouse. (b) Contours from the same session in a, with extracted contours overlaid. Speed modulated cells are plotted in cyan, and others in red. (c) Movement speed of the running wheel (black) and percent of speed modulated cells active (cyan). (d) Raster plots of speed modulated cells (cyan) and others (red). (e) Distributions of wheel speeds for the two mice used in recordings. (f) Average transient rate of speed modulated cells by movement speed for each mouse. (g) same as f, but more non-speed modulated cells.

3.2.6 Wirefree recording in rats

This LFOV Miniscope system is also capable of recording neural activity without constraint of a wire tether. Wirefree configuration includes the novel wirefree DAQ (Fig. 7c, d) developed based on wirefree v3 Miniscope (Shuman et al. 2020), with a MicroSD card (64GB, Kingston) mounted on it for local data storage. The wirefree DAQ (4 g) is powered by a single-cell, 400 mAh lithium-polymer battery (7.5 g), and affixed to the wired LFOV Miniscope (Fig. 7b) during experiment sessions. During recording, the imaging data from the CMOS sensor is transmitted into the serializer chip on the Miniscope PCB and then goes into the deserializer chip on the wirefree DAQ through a short coaxial cable (50Ω, CW2040-3650SR, Cooner Wire), followed by going into the memory in SAM E70 MCU through DMA channel built for fast data transmission without the interface of CPU. The data is finally saved into the SD card from the memory by SD v2.0 interface. The wirefree DAQ sends and receives command and acknowledgement from Miniscope PCB through I2C protocol, including LED adjustment, EWL focusing, frame rate, and gain of the sCMOS sensor, etc (Fig. 7d). The commands for configuring the Miniscope are saved into SD card beforehand, as well as the cropped ROI position for recording within the FOV.
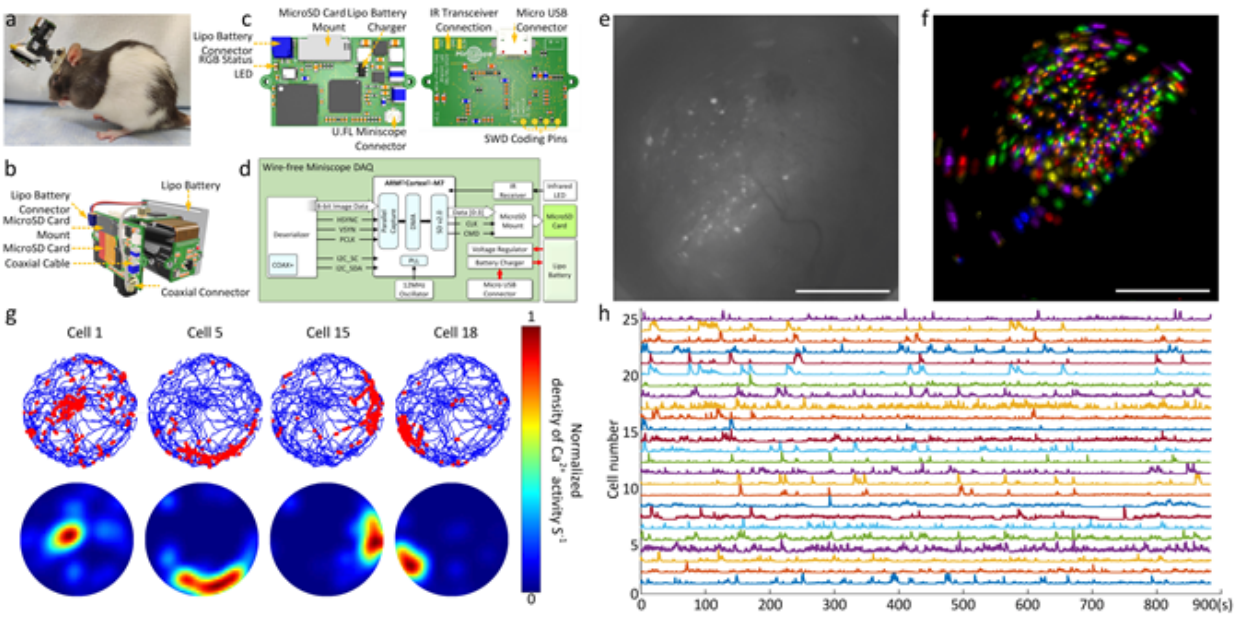
Figure 3.2.6. Imaging Hippocampus CA1 region in rats in circular maze with head mounted wirefree configuration. (a) Photograph of a rat wearing LFOV miniscope with wirefree DAQ and Lipo battery. (b) 3D rendering image of LFOV miniscope equipped with wirefree DAQ and Lipo battery. (c) Top and bottom PCB rendered layout images within Kicad. (d) Block schematic of the wire free daq. (e) Max projection from a 14 minute recording session after motion correction. Scale bar 500 µm. (f) Contours of extracted cells from CNMF-e analysis via CaImAn, colored randomly. Scale bar 500µm. (g) Spatial distributions of the rat's location during Ca^{2+} expression for four example cells when a rat is exploring four arenas in a circular maze. Top: rat's trajectory (blue lines) and its position during Ca^{2+} events (red dots). Bottom: gaussian-smoothed heatmaps of Ca^{2+} events, normalized by the rat's occupancy time per bin (2cm × 2cm) for the same example cells. (h) Extracted calcium activity from 25 example cells in f.

Before the beginning of each session record, the Miniscope is connected to a computer to check the imaging parameters and choose the imaging ROI. Considering the recording speed is limited by the oscillator and the writing speed of microSD card, we choose the recording window size to be 608×608 with 15fps frame rate, corresponding to 1.4×1.4 mm2 FOV in the object space (GRIN lenses is 1.8mm in diameter). Thus, around 5.5MB needs to be written into SD card per second, which is under the limitation (10MB/s), enabling 200 mins video recording with 64GB micro SD card. A status RGB LED (APHF1608SEEQBDZGKC, Kingbright) is integrated on the wirefree DAQ for status checking (Fig. 7c). At the beginning of each imaging session, the status LED is set with blue LED turned on for 5 seconds, and red LED for 2 second. This time stamp setup is also saved into an SD card which can be read by the MCU as a configuration before the recording. The moment when the red LED turns off indicates the

starting of recording, which is used to synchronize with the behavior camera overhead (Logitech C270). For testing the functionality of the wirefree configuration, the experiment is conducted by putting the rat into a circular maze, to record the behavior traces and the neuronal activities simultaneously. Small infrared light-emitting diode (LED) is attached to the rat's head for the behavior camera to track its position. The sampling frequency for the position-tracking signal was 48 Hz (IDIBAPS) and 46.875 Hz (UCL). Animals were food-deprived up to 85% of their original weight after which recordings commenced. Sucrose grain pellets (20mg) were thrown in the enclosed environment every 20 s at random locations within the open field, keeping the animal in continuous locomotion, thereby allowing a complete sampling of the environment47.

The max projection from a 15-minute recording session after motion correction is shown in Fig. 7e, and the colored extracted contours of 575 cells are shown in Fig. 7f. The gaussian-smoothed heatmaps of Ca^{2+} events, shown in Fig. 7g, are normalized by the rat's occupancy time per bin (2cm × 2cm), to show the preferred firing location of place cells within the open field in the circular maze. The contours of 25 extracted example cells from CNMF-e analysis via CaImAn are shown in Fig. 7h.

3.3 DISCUSSION

We present a large field of view (FOV), open-source Miniscope platform aimed at extending the capabilities of microendoscopy imaging approaches in large rodents and non-human primates, such as rats, marmosets, and macaque monkeys. The system can image around 3.2 mm × 2.5 mm FOV with single cell resolution (≤ 2 μm) at 23 Hz, has an electrically adjustable WD of 1.85 mm +/-150μm using an electrowetting lens, incorporates an absolute head-orientation sensor, and weighs only 14 grams. This system is capable of multiple imaging configurations including cortical imaging through a cranial window and deep brain imaging using one or multiple implanted optical probes. It provides a low-cost and highly configurable imaging methodology for recording neural activity in the cortex and deeper brain structures in multiple animal models.

Our large FOV Miniscope has been validated in freely behaving rats by imaging GCaMP7s expressing neurons in the CA1 layer of the hippocampus, and is the first demonstration of recordings of place cells in freely behaving rats using calcium imaging. Previous recordings of this method in our lab had been severely limited by the number of recorded cells compared to mice, typically yielding around 100 cells or fewer (Hart et al. 2020). With the presented LFOV Miniscope, we can now attain cell numbers greater than 1000 within the GRIN lens FOV in a single rat (Fig. 3.2.3.1 and Fig. 3.2.4), and even greater numbers when utilizing the entire FOV (Fig. 3.2.5.2). This development now allows calcium imaging in larger animal models than just mice so that researchers can evaluate what neural signatures are common across species. Additionally, this Miniscope platform has also been extended for use in wirefree operation. This reduces behavior interference (such as cable tangling and biting the coaxial cable) as enables recordings during flight (Yartsev and Ulanovsky 2013; Omer et al. 2018) or from two animals socially interacting (Kingsbury et al. 2019). Performance of three configurations of the LFOV Miniscope, i.e., 1.8mm WD, 3.5mm WD, and wirefree, are listed in

Table 1. With a greater than 10 fold increase in FOV and detectable neurons than previous generation Miniscopes, we expect this imaging platform for freely behaving animals to generate qualitatively and quantitatively new data for neuroscience applications.
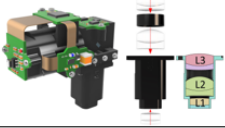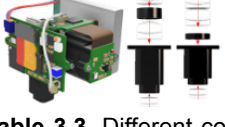
Configurations	Specifications								
	Weight (g)	FOV (mm²)	Resolution (µm)	WD (mm)	M	Pixel	Frame rate (fps)	Clock (MHz)	Time
Wire/WD:1.8 mm	~15	3.2×2.5	<=2	1.8	1.86	1296×972	23	66.67	Long
Wire/WD:3.5 mm	~15	3×2.5	<=2	3.5	1.56	1296×972	23	66.67	Long
Wirefree	~26	1.4×1.4 1.7×1.7	<=2	1.8 3.5	1.86 1.56	608×608	20	24	~1 hour

Table 3.3. Different configurations of the LFOV Miniscope. We present three different configurations: 2 configurations with different focal lengths (1.8mm working distance (WD) and 3.5mm WD), and a wirefree module that is compatible with either optical setup.

3.4 Development of real-time analysis methods

In addition to these described hardware developments, I have also worked towards advancing methods for analyzing calcium data in real time. In this collaboration with Dr. Zhe Cen and Dr. Jason Cong (Cong lab), we have developed methods of implementing motion correction (Z. Chen, Blair, and Cong 2019) and calcium trace extraction (Z. Chen et al. 2020) onto Field-Programmable Gate Array (FPGA) hardware for developing real-time applications for calcium imaging. Processing of calcium imaging videos is particularly computationally intensive, and both offline and online methods utilize high-performance CPU and GPUs to accelerate the process (Pnevmatikakis and Giovannucci 2017; Pnevmatikakis et al. 2016; Zhou et al. 2018; J. Lu et al. 2018; Giovannucci et al. 2019). However, applications for implantable or wearable neurofeedback devices necessite low weight and limited temperature range. These limitations are especially true on smaller animals (such as rats, bats, and mice) where most calcium imaging studies are performed (Aharoni et al. 2019; Mau, Hasselmo, and Cai 2020; Rubin et al. 2019; Hart et al. 2020; Schuette et al. 2020). Furthermore, recording studies often benefit by employing wireless recordings, since this reduces limits on behaviors and increases addressable hypotheses (Yartsev and Ulanovsky 2013; Liberti et al. 2017; Omer et al. 2018; Topalovic et al. 2020).

To address this need for a low energy cost, small size, computational method capable of performing calcium imaging studies in real-time, we developed a hardware implementation of a non-rigid motion correction algorithm, "NoRMCorre" (Pnevmatikakis and Giovannucci 2017). This is implemented on a Field Programmable Gate Array (FPGA) and utilizes Long Short-Term Memory (LSTM) learning algorithm to predict and correct the motion artifact inherent in calcium imaging. An LSTM is a recurrent neural network model that can be used to solve time-series prediction tasks, and performs comparably to offline methods (Figure 3.4.1) while reducing computational costs by 95%. Implementation of this method for motion correction onto a small

FPGA (Ultra96) achieves 80 μs latency (outperforming a Xeon E5-2860 CPU by 82x) while getting about 4 orders of energy efficiency gain.
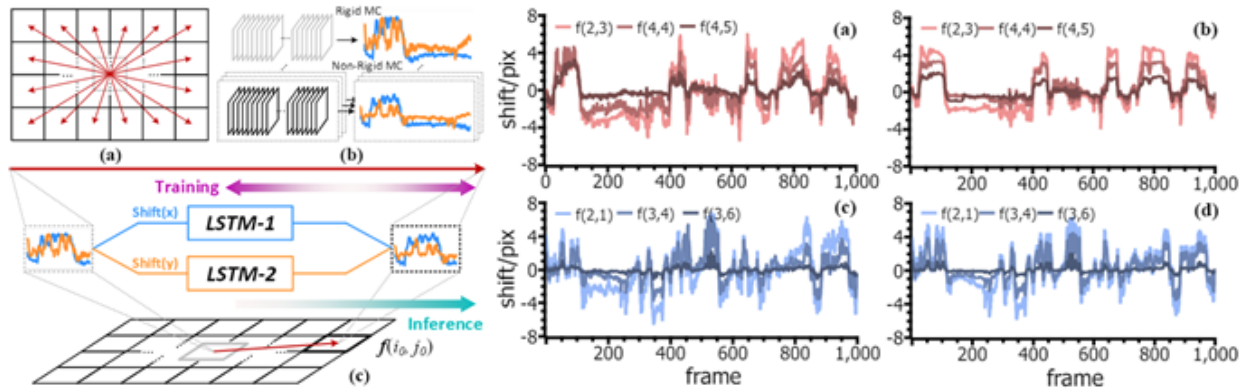
Figure 3.4.1 Development of real-time motion correction using artificial intelligence. [Left Half] (a) Proposed LSTM-assisted non-rigid motion correction. (b) Motion vector extraction for the central region and all image patches. (c) LSTM inference on one patch. [Right half] Extracted motion vectors in horizontal/vertical direction from three different image patches by using the (offline) NoRMCorre method (a)/(c) and the (real-time) LSTM inference (b)/(d).

But motion correction is only the first (though very necessary) step for performing calcium imaging in real-time. In addition to being computationally demanding, most offline calcium imaging analytic methods are also acausal, meaning the interpretation of a given data point is influenced by ones that occur later in time. For calcium imaging, this affects the deconvolution approach to spike detection, where a sudden large increase in fluorescence, then followed by a slow decay, is inferred to be spike-related because it conforms to how the fluorescent protein responds to spike bursts. This acausality imposes a delay between receiving the data (sudden flash) and labelling that frame (spike vs. no-spike), which is not ideal for real-time applications. Therefore, the goal of developing this real-time trace extraction method was to reduce this acausal delay, as well as implement this method on a small, low energy cost device suitable for neurofeedback applications.

This method consists of 4 main features to achieve sub-millisecond latency while being able to track calcium activity from 1024 cells simultaneously (Figure 3.4.2). First, motion correction is performed from the FPGA implementation described above. Next we perform

frame-wise background subtraction, where we perform a small 3x3 pixel smoothing followed by a morphological opening function that removes most of the background fluorescence while sparing the punctate fluorescence of the individual cells (J. Lu et al. 2018; Hart et al. 2020). Third, we used pre-established contours from a previous recording that has been processed offline using Constrained Non-negative Matrix Factorization (Zhou et al. 2018) to act as template and extract fluorescence from each contour. Finally we use a separate LSTM model on these real-time calcium traces. This LSTM is trained on the traces produced by the offline analysis data set and used to improve the spike detection and remove the acausal delay. A novel bit-sparse data representation was also developed to improve the accuracy of the LSTM model while maintaining low energy cost. These combined methods enabled calcium imaging in real-time from 1024 possible cells, but kept energy and computational costs lower than that of typical CPU/GPU workstations.
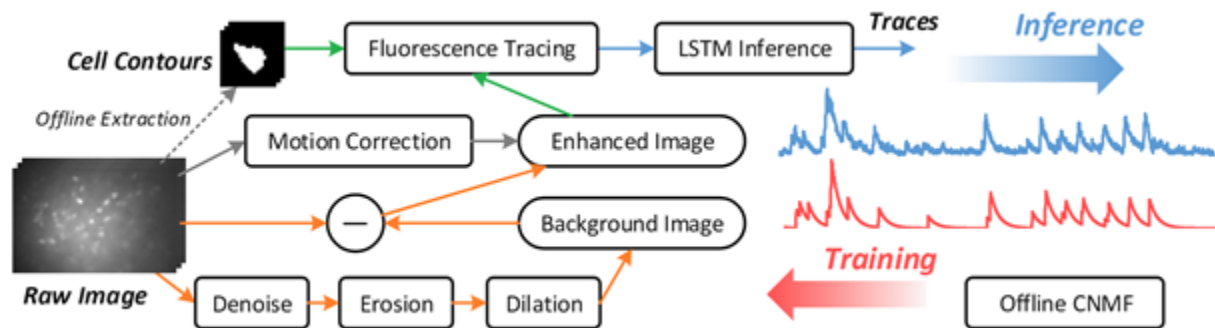
Figure 3.4.2 Development of real-time calcium trace extraction. Proposed LSTM-based calcium image processing flow. Motion correction and background subtraction is performed on each frame in real-time. System is implemented on FPGA hardware to accelerate performance to achieve sub millisecond latency with low-energy cost.

CHAPTER 4: Effortful Decision Making in ACC

Note: Chapter 4 has been published (Hart, Blair et al. 2020; DOI: 10.1523/jneurosci.2548-19.2020) and its contents have been copied here for ease of access.

The ACC is implicated in effort exertion and choices based on effort cost, but it is still unclear how it mediates this cost-benefit evaluation. Here, male rats were trained to exert effort for a high-value reward (sucrose pellets) in a progressive ratio lever-pressing task. Trained rats were then tested in two conditions: a no-choice condition where lever-pressing for sucrose was the only available food option, and a choice condition where a low-value reward (lab chow) was freely available as an alternative to pressing for sucrose. Disruption of ACC, via either chemogenetic inhibition or excitation, reduced lever-pressing in the choice, but not in the no-choice, condition. We next looked for value coding cells in ACC during effortful behavior and reward consumption phases during choice and no-choice conditions. For this, we used in vivo miniaturized fluorescence microscopy to reliably track responses of the same cells and compare how ACC neurons respond during the same effortful behavior where there was a choice versus when there was no-choice. We found that lever-press and sucrose-evoked responses were significantly weaker during choice compared with no-choice sessions, which may have rendered them more susceptible to chemogenetic disruption. Together, findings from our interference experiments and neural recordings suggest that a mechanism by which ACC mediates effortful decisions is in the discrimination of the utility of available options. ACC regulates these choices by providing a stable population code for the relative value of different options.

4.1 INTRODUCTION

Real-world decisions rarely involve choosing between unambiguously favorable versus unfavorable options. Often, options must be evaluated along multiple dimensions that

incorporate an evaluation of the rewards themselves as well as the actions or efforts to procure them (Skvortsova et al., 2014). For example, we typically make decisions between options in comparison, where one outcome may be more costly (i.e., more effortful) yet more preferred than the other.

Outside of the striatum, which has been the major region of study in such effort-based decision-making studies (J. D. Salamone et al. 1991; John D. Salamone, Cousins, and Bucher 1994; J. D. Salamone et al. 2003; J. D. Salamone et al. 2007; M.S. Cousins et al. 1996; Nowend et al. 2001; Ghods-Sharifi and Floresco 2010), the ACC is also involved in the evaluation of both physical and cognitive effort costs (Walton et al. 2003; Schweimer and Hauber 2005; Floresco and Ghods-Sharifi 2007; Hillman and Bilkey 2010; Hillman and Bilkey 2012; Cowen, Davis, and Nitz 2012; Hosking, Cocker, and Winstanley 2014; Winstanley and Floresco 2016). Neurons in both rat and primate ACC signal value during economic decision-making (Lapish et al. 2008; Azab and Hayden 2017; Hunt and Hayden 2017; Mashhoori et al. 2018). Neural responses in this region also track trial-by-trial outcomes of choices (Procyk, Tanaka, and Joseph 2000; Shidara and Richmond 2002; Seo and Lee 2007; Akam et al. 2020), reward history (Bernacchia et al. 2011), reward prediction errors (Hayden, Pearson, and Platt 2009; Kennerley, Behrens, and Wallis 2011; Hyman, Holroyd, and Seamans 2017), and counterfactual options ("rewards not taken") (Hayden, Pearson, and Platt 2009; Mashhoori et al. 2018). Indeed, both anatomic and functional evidence supports the idea that ACC activity supports representations of reward value and action outcomes (Shenhav, Botvinick, and Cohen 2013; Heilbronner and Hayden 2015).

A paradigm that involves selecting between qualitatively different reinforcers may closely model human decisions where we encounter options that are more/less preferred, not more/ less of the same reward identity (J. D. Salamone et al. 1991; J. D. Salamone et al. 2007; John D Salamone et al. 2017; Michael S. Cousins and Salamone 1994; Nowend et al. 2001; Randall et

al. 2012; Randall et al. 2014; Randall et al. 2015; Nunes et al. 2013; Yohn, Errante, et al. 2016; Yohn, Lopez-Cruz, et al. 2016; Yohn, Gogoj, et al. 2016). The majority of the seminal rodent studies probing ACC in effort-based choice (Walton, Bannerman, and Rushworth 2002; Walton et al. 2003; Floresco and Ghods-Sharifi 2007; Hauber and Sommer 2009; Winstanley and Floresco 2016) have used traditional pharmacological, lesion, and electrophysiological approaches, so a fine-grained analysis involving cell type-specific, temporally restricted targeting of ACC in effort choice has not yet been reported.

Here, we tested the effects of inhibitory (hM4Di, or Gi) and excitatory (hM3Dq, or Gq) designer receptors exclusively activated by designer drugs (DREADDs) (Armbruster et al. 2007; Alexander et al. 2009; Roth 2016) in ACC on the same effortful choice task that we previously probed following lesions (Hart et al. 2017) and pharmacological inactivations (Hart and Izquierdo 2017). Briefly, our task required rats to choose between working for a preferred reward (sucrose) versus consuming a concurrently and freely available, but less preferred reward (standard chow). We assessed the role of ACC on (1) progressive ratio (PR) lever-pressing for sucrose pellets (i.e., general motivation), and (2) PR lever-pressing with choice (PRC) of a freely available alternative (i.e., effortful decision-making: choosing between working for sucrose pellets vs concurrently available laboratory chow). We also tested the effects of ACC inhibition and excitation on the choice between sucrose pellets versus chow when these reinforcers were both freely available (i.e., "free choice"). Finally, in a separate cohort of animals, we looked for value coding cells in ACC during effortful behavior and reward consumption phases. For this, we used in vivo miniaturized fluorescence microscopy (University of California at Los Angeles "miniscopes") (Ghosh et al. 2011; Aharoni et al. 2019) to reliably track responses of the same cells and compare how ACC neurons respond during the same effortful behavior in separate sessions where there was a choice (PRC) versus when there was no choice (PR).

76

4.2 MATERIALS AND METHODS

4.2.1 Subjects

Subjects were N = 44 adult male Long-Evans rats (n = 12 Gi DREADD experiment, n = 12 Gq DREADD experiment, n = 10 GFP [null virus] control experiment, n = 4 calcium imaging experiment, n = 6 acute slice recording for validation of DREADDs). Rats were obtained from Charles River Laboratories, were postnatal day 60 at the time of arrival to the University of California at Los Angeles vivarium, and were singly housed for all phases of experiments, with the exception of the acclimation period and handling, during which they were pair-housed. All rats were handled for 10 min in pairs for 5 d after a brief acclimation period (3 d). Rats weighed an average of 309.1 g at the beginning of experiments. Three subjects were not included in the final data analyses: 1 from Gi experiment and 1 from Gq experiment due to unilateral (not bilateral) viral expression, and 1 from the GCaMP experiments due to poor stability of imaging over days.

The vivarium was maintained under a 12/12 h reverse light cycle at 22°C, and lab chow and water were available ad libitum before behavioral testing. Rats were food restricted 1 d before behavioral testing to ensure motivation to work for rewards. Given the sensitivity of the behavioral tests on motivation, special care was taken to maintain consistent food rations throughout the experiment. This was 12 g/d at the beginning of testing but then decreased to 8 g/d at the beginning of the choice phase (details below). Rats were monitored every other day for their body weight, and were never permitted to drop below their 85% free feeding baseline weight. Training and testing were conducted during the early portion of the dark cycle (;0800-1200 h). Experiments were conducted 5-7 d per week, and rats were fed once daily on weekends (12 g) when testing was not conducted. All procedures were reviewed and approved by the Chancellor's Animal Research Committee at the University of California, Los Angeles. Food restriction. One day before behavioral testing began, rats were singly housed, the amount

of chow given to each rat was reduced to 12 g/d, and rats were given ;10 sucrose pellets (45 mg

dustless precision sucrose pellets; Bio-Serv) in their home cage to acclimate them to the food

rewards. Rats were maintained on 12 g of food daily and were each fed within 30 min of

completing the daily testing. Once rats progressed to the choice task, they were given 8 g of

chow per d, in addition to the food they consumed during testing. At the time of death, rats

weighed an average of 356.5 g.

4.2.2 Stereotaxic surgery

General surgical procedures were the same as those recently published (Hart and

Izquierdo 2017). Rats were anesthe-tized with isoflurane (5% induction, 2% maintenance in 2

L/min O2).Burr holes were drilled bilaterally on the skull for insertion of 26-gauge guide

cannulae (PlasticsOne), after which 33-gauge internal cannulae(PlasticsOne) were inserted.

Rats were infused with 0.5ml of virus at a flow rate of 0.1ul/minute, and injectors were

subsequently left in place for 5 additional minutes to allow for diffusion of solution. In the Gi

experiment, the virus used was AAV8-CaMKIIa-hM4D(Gi)-mCherry (Addgene, viral prep

#50477-AAV8). In the Gq experiment, the virus used was AAV8-CaMKIIa-hM3D(Gq)-mCherry

(Addgene, viral prep #50476-AAV8). In the GFP (null virus) control, the virus used was

AAV8-CaMKIIa-eGFP (Addgene). In the imaging experiment, the virus used was

AAV9-CaMKIIa-GCaMP6f (Addgene). The coordinates used for the guide cannulae targeting

area 24 of ACC (van Heukelum et al.,2020) in the Gi, Gq, and GFP control experiments were as

follows: AP 2.0 mm, ML 0.7 mm, DV 1.9 mm from bregma. Four of 12 rats in the Gi experiment

received infusions in more anterior ACC (area 32) to compare with other laboratory experiments

on decision confidence (Stolyarova et al. 2019), at AP 3.7 mm, ML 0.8 mm, DV 1.6 mm from

bregma. Since no differences emerged from this differential target-ing, we combined the ACC

groups. In the imaging experiment, coordinates were as follows: AP 2.0mm, ML 0.7 mm, DV

-1.4 mm (0.5ul) from bregma, and a second 0.5ul bolus of virus was injected at DV -0.9mm.

Injectors extended 1 mm beyond the tip of the cannula. Followingthe 5 min diffusion time, the

cannulae and injectors were removed, inci-sions were stapled closed, and the rats were placed

on a heating pad and kept in recovery until ambulatory before being returned to the vivarium.

Three days following viral infusions in the subset of rats receivingAAV9-CaMKIIa-GCaMP6f (for

calcium imaging), rats were implanted with 1.8-mm-diameter 0.25 pitch GRIN lenses (Edmund

optics part 64-519). Following similar surgical procedures, four anchor screws were secured to

the skull, after which a 2.0 mm craniotomy was drilled 0.2mm lateral to the center of the viral

infusion hole. The dura was cleared and ~0.5 mm of tissue was aspirated, after which the lens

was placed 2.0mm ventral from the surface of the skull and secured in place with cyanoacrylate

glue and bone cement. The lens was protected with Kwik-Sil (World Precision Instruments).

Postoperative care for all rats consisted of five daily injections of carprofen (5 mg/kg,

s.c.) and oral sulfamethoxazole/trimethoprim solution. Two to 3 weeks following lens

implantation, a small aluminum baseplate was attached to the animal's head and secured with

bone cement. The exposed lens was cleaned with 100% ethanol, and the baseplate was

secured in a position where cells in the FOV and vasculature were in focus. A 3D printed cover

was secured to the baseplate with an anchor screw at all times when recording was not

occurring. Rats were allowed a 5 d free feeding recovery period following viral infusion (Gi, Gq,

and GFP experiments) or GRIN lens implantation (imaging experiment) after which they were

food-restricted and behavioral testing began.

4.2.3 Apparatus

All behavioral testing was conducted in chambers outfitted with a house light, internal

stimulus lights, a food-delivery magazine, and 2 retractable levers positioned to the left and right

of the chamber wall, opposite the magazine. All hardware was controlled by a PC running Med-PC IV (Med Associates).

4.2.4 Miniaturize microscope data collection

Microscopes were custom built according to plans available at www.Miniscope.org. Images were acquired with a CMOS imaging sensor (Labmaker) attached to custom data acquisition (DAQ) electronics via a 1.5 mm coaxial cable. Data was transferred to a PC running custom-written DAQ software over USB 3.0. DAQ software was written in C++ and used Open Computer Vision (OpenCV) for image acquisition; 480x752 pixel images were acquired at 30 Hz and written to .avi files. DAQ software simultaneously recorded and time-stamped behavioral data and image data, allowing for offline alignment. All hardware design files and assembly instructions are available at www.Miniscope.org. Calcium signals were extracted using modified constrained non-negative matrix factorization scripts in MATLAB (The MathWorks, version 2016) (Pnevmatikakis et al. 2016; Zhou et al. 2018).

4.2.5 Lever press training

Rats were first given fixed-ratio 1 training where each lever press earned a single sucrose pellet (Bioserv). They were kept on this schedule until they earned at least 30 pellets within30 min. Following this, rats where shifted to a PR schedule where the required number of presses for each pellet increased according to the fol-lowing formula:

$$n_i = 5e^{(i/5)} - 5$$

where n_i is equal to the number of presses required on the ith ratio, rounded to the nearest whole number (Richardson and Roberts 1996), after 5 successive schedule completions. No timeout was imposed. Rats were tested on the PR schedule until they earned at least 30 pellets on any given day (~5 d) within 30 min. Upon meeting the PR performance criterion, a ceramic ramekin containing 18 g of lab chow was introduced (modified from (Randall

et al. 2012)) during testing. Rats were free to choose between consuming freely available but less preferred chow or lever-pressing for preferred sucrose pellets. Rats (Gi, Gq, and GFP experiments) were given at least 5 choice testing sessions before clozapine-N Oxide (CNO) or vehicle (VEH) injections began (details below).

4.2.6 Drug treatment during different types of test sessions

Rats in the Gi, Gq, and GFP control experiments were given either VEH (95% saline, 5% DMSO, 1 ml/kg) or CNO (3.0 mg/kg i.p. in 95% saline, 5% DMSO, 1 ml/kg) (Tocris Bioscience) in counterbalanced order, 45 min before test sessions. Three types of test sessions were given: (1) a PRC session during which rats lever pressed on the PR schedule in the presence of the ceramic ramekin containing lab chow so that they were free to choose between lever-pressing for sucrose versus free feeding on chow; (2) PR only sessions during which we omitted the ceramic ramekin (so that there was no freely available lab chow) to assess whether manipulations decreased lever-pressing in the absence of choice; and (3) a free choice consumption test where there was free access to pre weighed amounts of sucrose pellets and lab chow (18 g) in empty cages (different from their home cages). Following this, any remaining food was collected and weighed to determine rats' food preferences. All sessions were 30 min in duration. In a repeated-measures design, VEH or CNO was administered before a PRC testing session, a PR only testing session, and a free availability choice testing session, in that order, for each rat. The order of VEH versus CNO administration was counterbalanced for baseline choice performance. Rats were given at least 48 h between injections, and testing never occurred on consecutive days.

4.2.7 Death

Following behavioral testing, rats were killed by sodium pentobarbital overdose (Euthasol, 0.8 ml, 390 mg/ml pentobarbital, 50 mg/ ml phenytoin; Virbac) and perfused

transcardially with 0.9% saline followed by 10% buffered formalin acetate. Brains were postfixed in 10% buffered formalin acetate for 24 h followed by 30% sucrose cryoprotection for 5 d; 50 mm sections were coverslipped with DAPI mounting medium (Prolong Gold, Invitrogen), and visualized using a BZ-X710 microscope (Keyence).

4.2.8 DREADD quantification

Fifty micrometer sections taken from each animal were visualized at seven AP coordinates relative to bregma: 4.2, 3.7, 3.2, 2.7, 2.2, 1.7, and 1.6 mm. No fluorescence was observed beyond these coordinates. mCherry fluorescence was drawn by a blind experimenter on a GNU Image Manipulation Program document containing a schematic of each of these seven sections, drawn to scale. Spread was quantified as total pixel count across all seven sections.

4.2.9 Electrophysiological confirmation of DREADDs

Separate rats were prepared with ACC DREADDs using identical surgical procedures to the main experiments. Slice recordings did not begin until at least 4 weeks following surgery to allow sufficient hM receptor expression. Slice recording methods were similar to those previously published (Babiec et al., 2017). Six rats were deeply anesthetized with isoflurane and decapitated. The brain was rapidly removed and submerged in ice-cold, oxygenated (95% O_2/5% CO_2) ACSF containing (in mM) as follows: 124 NaCl, 4 KCl, 25 $NaHCO_3$, 1 NaH_2PO_4, 2 $CaCl_2$, 1.2 $MgSO_4$, and 10 glucose (Sigma Millipore); 400-mm-thick slices containing the ACC were then cut using a Campden 7000SMZ-2 vibratome. Slices from the site of viral infusion were used for validation. Expression of mCherry was confirmed after recordings were performed, and ACC slices with no transfection were used as control slices. Slices were maintained (at 30°C) in interface-type chambers that were continuously perfused (2-3 ml/min) with ACSF and allowed to recover for at least 2 h before recordings. Following recovery, slices

were perfused in a submerged-slice recording chamber (2-3 ml/min) with ACSF containing 100 mM picrotoxin to block GABAA receptor-mediated inhibitory synaptic currents. A glass microelectrode filled with ACSF (resistance = 5-10 MV) was placed in layer 2/3 ACC to record fEPSPs and postsynaptic responses elicited by layer 1 stimulation delivered using a bipolar, nichrome-wire stimulating electrode placed near the medial wall in ACC. Inhibitory validation in ACC with identical coordinates, reagents, and virus was previously performed by our laboratory, with the methods and data appearing elsewhere (Stolyarova et al., 2019), and so these experiments were not needlessly repeated. Briefly, we first recorded for 2 min without synaptic stimulation to measure spontaneous levels of activity. Presynaptic fiber stimulation (0.2 ms duration pulses delivered at 0.33 Hz) was then delivered, and the stimulation intensity was varied in 0.2 V increments to generate an input/output curve and identify the threshold for generation of postsynaptic responses. Stimulation strength was then set to the minimum level required to induce postsynaptic responses in ACC. Once stable responses (measured as the area of responses over a 4 s interval) were detected, baseline measures were taken for at least 10 min, followed by 20 min bath application of 10 mM CNO. In slices where CNO failed to elicit spontaneous activity, we generated a second input/output in the presence of CNO to test for CNO-induced changes in postsynaptic responses evoked by synaptic stimulation. Unless noted otherwise, all chemicals were obtained from Sigma Millipore.

4.2.10 Behavioral analyses

Behavioral data were analyzed using GraphPad Prism version 7 (GraphPad Software), SPSS version 25 (IBM), and MATLAB (The MathWorks, version R2017a). An a level for significance was set to 0.05. A mixed ANOVA with between-subject factor of virus (Gi, Gq, eGFP null) and within-subject factor of effort condition and injection (PRC, PR; VEH, CNO) was conducted on lever-pressing data as well as highest ratio achieved and number of pellets

earned. Subsequently, paired-samples t tests (reported as means +/- SEM) on data from the

PRC and PR tests were used to test for effects of CNO versus VEH. Because the dependent

measure was different in the free choice test (i.e., amount of food consumed, not lever presses),

a separate mixed ANOVA with between-subject factor of virus (Gi, Gq, eGFP null) and

within-subject factors of food type and injection (sucrose, chow; VEH, CNO) was conducted.

Following these group comparisons, which included virus as a factor, paired t tests were used to

test for effects of CNO on the total number of lever presses, highest ratio, and number of pellets

earned in each of the groups. Two-way ANOVA was used to analyze the effects of CNO on

temporal response patterns in each of the groups. Two-way ANOVA was used to test for effects

of CNO on total consumption during free consumption testing in each of the groups. Mixed

ANOVA was used to compare responding in the imaging and DREADDs animals, and

repeated-measures ANOVA was used to compare responding in the different session types

within the imaging group.

4.2.11 Calcium image analyses

Image analyses were performed using custom-written MATLAB (The MathWorks,

version R2017a) scripts. First, images were motion-corrected using functions based on the

Non-Rigid Motion Correction (NoRMCorre) package (Pnevmatikakis and Giovannucci 2017),

downsampled spatially by a factor of 2 (240x356pixels) and temporally by a factor of 4 (to a

frame rate of 7.5 fps). Inorder to remove background fluorescence, we performed a neural

enhancement processing step as in the min1pipe processing framework (J. Lu et al. 2018).

Briefly, from each frame, we constructed a background fluorescence estimate by performing a

neuron-sized morphological opening function, and subtracting this background frame from the

original frame. This removes large fluorescence artifacts inherent in single-pho-ton microscopy

while preserving neural components. This motion-cor-rected, downsampled, and enhanced

video was then processed using Constrained Non-negative Matrix Factorization for Endoscopic data (CNMF-E) (Pnevmatikakis et al. 2016; Zhou et al. 2018). This extracted individual neural segments, denoised their fluorescent signals, demixedcross-talk from nearby neighbors, and deconvolved the calcium transi-ents to estimate temporally constrained instances of calcium activity for each neuron (Friedrich et al. 2017). These estimated calcium event tim-ings were used to compare calcium activity time-locked to specific behavioral instances. Neurons were matched across recording sessions using CellReg (Sheintuch et al. 2017) by matching cells based on their contours and centroid locations.

4.2.12 Calcium response analysis

A cell's probability of generating calcium transients proximal to a trigger event (e.g., a lever press [LP] or magazine head entry [HE]) was compared against a baseline probability surrounding each event. LP bouts were defined by the first lever press within a ratio and HE bouts defined as the first time point where the infrared beam was broken via nosepoke, after completion of that ratio. LP and HE bouts where the last lever press and first head entry bout were separated by >30 s were excluded from analysis. We focused on HEs that occurred shortly after completion of LP bouts so that HE events during the chow consumption period before lever-pressing in PRC and CON sessions were excluded. This subsampling also excluded HE events with no sucrose delivery and LP events that were closely preceded by HE events (see Fig. 4.3.2.1J, bottom). This minimized contamination between LP and HE evoked calcium signals. For every cell recorded within a session, we created a 6.25 s (+/-3.125) perievent time histogram (PETH) divided into 47 equal time bins (bin size = 133 ms), with the 24th (middle) bin centered on the trigger events (which were either LP or HE bout starts). PETHs were constructed for LP and HE bouts from each session type, yielding 6 PETHs for

each cell of the average transient rate surrounding each trigger event. Only half of the

bout-centered PETH window (24 bins) was used as the ROI for statistical analysis.

To test whether a cell responded before LP events, we used a binomial test on each of

the first 24 bins compared with the average transient rate in the 23 bins following LPs. The

same procedure was applied to HE events, where a binomial test was applied to each of the last

24 bins compared with the average transient rate in the 23 bins preceding HEs. This pre-post

event approach is consistent with what others have defined as task-evoked calcium responses

(Jennings et al. 2015). These comparisons were used to identify cells modulated by each event

while minimizing overlap between LP and HE responses (see Fig. 4.3.2.1J). A cell was

classified as significantly responsive within the ROI if the transient rate within the ROI was

greater than baseline, and one or more of three probability criteria were met: at least 1 of 24

ROI bins beat $p<0.00125$, at least 2 of 24 ROI bins beat $p<0.0115$, or at least 3 of 24 ROI bins

beat $p<0.0285$. These p thresholds were chosen to yield an equal probability of each criterion

being met, and $p = 0.01$ for meeting one or more of the criteria by chance. Hence, the

probability of erroneously classifying a cell as responsive was 1%. Examples of LP and HE

responsive cells are shown in Figure 4.3.2.2A and Figure 4.8A, respectively.

To compare responses of each individual cell with LP and HE events during different

types of experimental sessions, we analyzed a subpopulation of cells that met two criteria: (1)

the cell responded significantly to the trigger event (LP or HE) during at least one session; and

(2) the cell fired (but did not necessarily respond to the trigger event) during at least one session

of all three imaging session types (PR, PRC, and CON). For each cell meeting these two criteria

for LP events, three PETHs were derived, one for each session type: PETHPR, PETHPRC,

PETHCON (see Fig. 4.3.2.2B). For cells meeting these criteria for HE events, an additional

PETH was computed for ramekin entries during PRC sessions (PETHR-PRC) to analyze

similarity of responses between sucrose and chow consumption (see Fig. 4.3.2.3B). However,

ramekin HEs within a session were few compared with sucrose HEs; thus, the PETHR-PRC is relatively undersampled. Each mean PETH was constructed by computing an unweighted average of session PETHs over all events from the same session type during which the cell was active. The averaged PETH was then smoothed by convolving it with a 5-bin Gaussian function of unit area. The smoothed PETH for each cell was normalized via division by a factor B, which was the value of the largest bin in any of the PETHs for that cell: B = max (PETHPR, PETHPRC, PETHCON). Finally, the frequency of responsive cells across session types for HE and LE events was compared against random number samples from a uniform distribution, analyzed using chi-square tests.

4.2.13 Satiety control condition

For a subset of calcium imaging sessions, we administered a satiety control condition, "CON." For these sessions, we capitalized on the fact that rats typically consume chow early in the test session, presented them with the lever and the chow initially, allowed them to consume chow, but then removed the chow once the rat began to lever press. This control condition allowed rats to reach a comparable motivational (more sated) state relative to the PR-only condition, and thus controlled for satiety differences between PR and PRC sessions. Lever-pressing behavior in these sessions was similar to during PR-only sessions (see Fig. 4.3.2.1I). The ramekin was removed after lever-pressing behavior commenced, so we could not construct ramekin response PETHs (PETHR-CON) since no ramekin HEs occurred after the fifth lever press (defined by our baseline calcium transient rate calculation).

4.3 RESULTS

4.3.1 Chemogenetic Manipulations

In favor of brevity, results of the chemogenetic manipulation of ACC activity will be briefly summarized so that the imaging results are understandable. For more comprehensive details concerning histological localization (Fig.

4.3.1.1 Effects of DREADDs inhibition and excitation of ACC

We found that chemogenetic inhibition of ACC significantly decreased lever-pressing during PRC but not PR sessions. Planned comparisons revealed CNO significantly reduced the total mean number of lever presses during 30 min PRC sessions (t(10) = 3.047, p = 0.01; VEH = 216.1 +/- 52.85 presses; CNO = 173.2 +/- 40.27 presses) (Fig. 4.3.1.1A). The total amount of chow consumed during 30 min PRC sessions was not affected by CNO treatment (t(10) = 1.048, p = 0.32; VEH = 7.79 +/- 0.33 g; CNO = 7.50 +/- 0.36 g) (Fig. 4.3.1.1E). CNO had no effect on PR responding in the absence of freely available chow (t(10) = 0.26, p = 0.80; VEH = 905.1 +/- 102.00 presses; CNO = 893.9 +/- 128.3 presses) (Fig. 4.3.1.1D).

Using identical procedures to the inhibition experiment, a separate group of rats was assessed on effortful choice following excitatory Gq DREADDs transfection in ACC. Similar to results for the Gi experiment, we found that chemogenetic excitation of ACC significantly decreased lever-pressing during PRC but not PR sessions. Planned comparisons revealed CNO significantly reduced the total mean number of lever presses during 30 min PRC sessions (t(10) = 2.31, p = 0.04; VEH = 210.7 +/- 49.44 presses; CNO = 166.6 +/- 40.4 presses) (Fig. 4.3.1.1A). The total amount of chow consumed during 30 min PRC sessions was not affected by CNO treatment (t(10) = 0.39, p = 0.71; VEH = 7.71 +/- 0.36 g; CNO = 7.81 +/- 0.42 g) (Fig. 4.3.1.1E). CNO had no effect on PR responding in the absence of freely available chow (t(10) = 1.15, p = 0.28; VEH = 1107.00 +/- 99.66 presses; CNO = 1209.00 +/- 156.3 presses) (Fig. 4.3.1.1D).

To test whether results for Gi and Gq DREADDs could be explained by virus exposure alone, a control virus carrying only GFP (but no DREADD receptors) was infused into ACC in a separate group of rats. A paired t test revealed no effect of CNO on the total mean number of

lever presses during 30 min PRC sessions (t(9) = 0.48, p = 0.64; VEH = 314.9 +/- 57.34 presses; CNO = 302.7 +/- 59.66 presses) (Fig. 4.3.1.1A). The total amount of chow consumed during 30 min PRC sessions was not affected by CNO treatment (t(9) = 0.26, p = 0.80; VEH = 6.65 +/- 0.99 g; CNO = 6.85 +/- 0.34 g) (Fig. 4.3.1.1E). CNO also had no effect on PR responding in the absence of freely available chow (t(9) = 0.73, p = 0.48; VEH = 1001.00 +/- 109.4 presses; CNO = 1043.00 +/- 120.00 presses) (Fig. 4.3.1.1D).

The same pattern was observed for conventional measures of PR responding, highest ratio, and number of pellets earned, dur- ing PRC sessions (Fig. 4.3.1.1B,C). In the Gi group, CNO reduced the highest ratio achieved (t(10) = 3.48, p = 0.0059; VEH = 14.91 +/- 2.63; CNO = 12.36 +/- 2.04) and number of pellets earned (t(10) = 4.209, p = 0.0018; VEH = 30.18 +/- 3.3 pellets; CNO = 27.45 +/- 3.2 pellets). In the Gq group, CNO reduced the highest ratio achieved (t(10) = 2.43, p = 0.0355; VEH = 14.36 +/- 2.68; CNO = 11.82; +/- 2.05) and number of pellets earned (t(10) = 2.70, p = 0.022; VEH = 29.36 +/- 3.71 pellets; CNO = 26.55 +/- 3.50 pellets). CNO had no effect on the highest ratio achieved (t(9) = 0.33, p = 0.75; VEH = 19.9 +/- 2.80; CNO = 20.5 +/- 3.06) or the number of pellets earned (t(9) = 0.29, p = 0.78; VEH = 35.2 +/- 3.69 pellets; CNO = 34.6 +/- 2.54 pellets) in the GFP control group.

As with lever-pressing, these measures were not affected dur- ing PR sessions. In the Gi group, CNO had no effect on highest ratio achieved (t(10) = 0.71, p = 0.49; VEH = 43.00 +/- 3.89; CNO = 44.36 +/- 4.47) or number of pellets earned (t(10) = 0.07, p = 0.95; VEH = 54.55 +/- 1.88 pellets; CNO = 54.45 +/- 2.43 pellets). In the Gq group, CNO had no effect on highest ratio achieved (t(10) = 1.04, p = 0.32; VEH = 54.91 +/- 4.47; CNO = 58.82 +/- 5.71) or number of pellets earned (t(10) = 0.87, p = 0.41; VEH = 59.09 +/- 1.77 pellets; CNO = 60.45 +/- 2.46 pellets). CNO also had no effect on the highest ratio achieved (t(9) = 0.72, p = 0.49; VEH = 49.7 +/- 4.56; CNO = 51.5 +/- 5.12) or the number of pellets earned (t(9) = 0.60, p = 0.56; VEH = 57.2 +/- 2.38 pellets; CNO = 57.8 +/- 2.59 pellets) in the GFP control group.
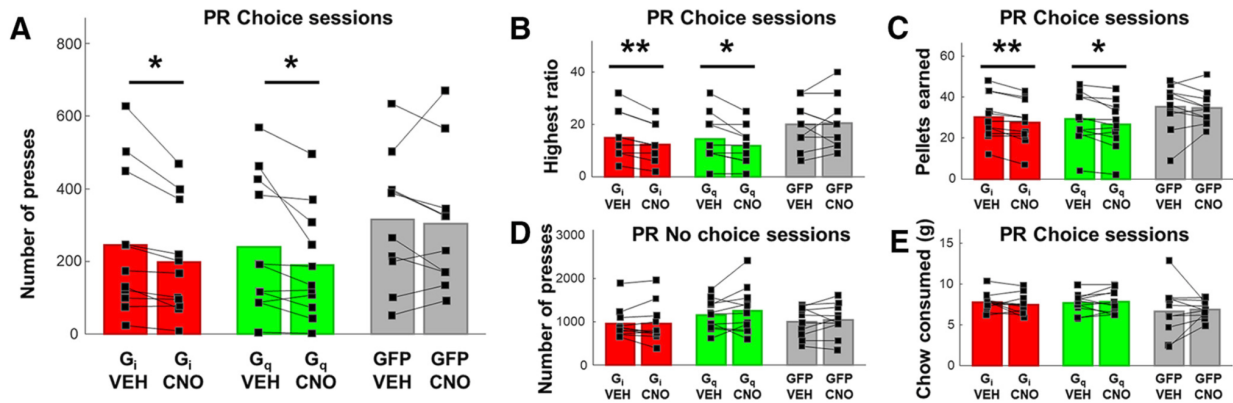
Figure 4.3.1.1. Effects on effortful choice behavior following DREADDs inhibition and excitation of ACC. **A**, Mean lever presses during PRC sessions, when rats were presented with both the possi- bility of lever-pressing under a PR schedule for sucrose pellets and freely available chow. Shown is within-subject, counterbalanced choice behavior under VEH and CNO. CNO significantly reduced the number of lever presses in the Gi and Gq conditions, but not in the GFP condition. **B**, Highest ratio achieved and (**C**) number of sucrose pellets earned during PRC sessions, when rats were presented with both options in the Gi, Gq, and GFP conditions, in rats receiving CNO compared with within-subject VEH. CNO significantly reduced these measures in the Gi and Gq conditions, but not in the GFP condition. **D**, There was no change in lever presses when chow was not available as an alternative option in Gi, Gq, and GFP conditions, in rats receiving CNO compared with within-subject VEH. **E**, Total chow consumed during choice testing was not different following VEH versus CNO in the Gi, Gq, or GFP condition. *$p < 0.05$, **$p < 0.01$.
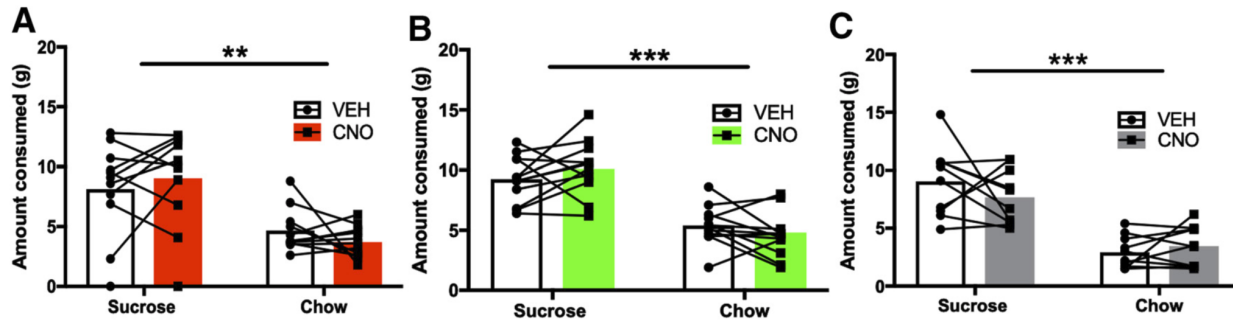
Figure 4.3.1.2. Free choice consumption in all three treatment groups following CNO administration. Mean consumption of sucrose and chow when rats were presented with both as freely avail- able options. Shown is within-subject, counterbalanced choice behavior under VEH and CNO, indicating that food preference was intact: rats preferred the sucrose over chow. **A**, CNO had no effect on either sucrose or chow consumed in the Gi condition. **B**, CNO had no effect on either sucrose or chow consumed in the Gq condition. **C**, CNO had no effect on either sucrose or chow consumed in the null virus (GFP) condition. **$p < 0.01$, ***$p < 0.001$.

4.3.1.2 Free choice consumption tests

In the Gi-group, a two-way ANOVA (food type: sucrose, chow; injection: VEH, CNO) on

the amount of sucrose and chow con-sumed during free choice consumption testing revealed a

signifi-cant main effect of food type (F(1,10)=12.02, p=0.006;sucrose = 8.59 +/- 0.83 g; chow = 4.19 +/- 0.34 g), but no significant food x type injection interaction (F(1,10)= 1.415, p= 0.26), ormain effect of injection (F(1,10)=0.01,p= 0.91) was found.Hence, food preference was intact and not affected by CNO injection. In the Gq-group, a two-way ANOVA (food type: sucrose, chow; injection: VEH, CNO) on the amount of sucrose and chow consumed during free choice consumption testing revealed a significant main effect of food type (F(1,10)= 47.63, p,0.001; sucrose = 9.68 +/- 0.47 g; chow = 5.10 +/- 0.37 g), but no significant food x type injection interaction (F(1,10)=2.27,p= 0.16) or main effect of injection (F(1,10)=0.06, p=0.81),indi-cating food preference was intact and unaffected by CNO.Similarly, in the GFP group, a two-way ANOVA (food type: su-crose, chow; injection: VEH, CNO) on the amount of sucrose and chow consumed during free choice consumption testing revealed a significant main effect of food type (F(1,9)=80.63, p,0.001; sucrose = 8.37 +/- 0.60 g; chow = 3.19 +/- 0.35 g), indicat-ing food preference was intact. No significant food x type injection interaction (F(1,9)=1.27, p=0.29), or effect of injection(F(1,9)=0.97, p= 0.35) was found (Fig. 4.3.1.2).

4.3.1.3 Time course of lever-pressing in PR and PRC

We found that the presence of an alternative option (chow) reduced lever-pressing in the PRC condition, and that both Gi and Gq DREADDs decreased lever-pressing in this PRC condition, but not in the PR condition where lever-pressing was more robust. Of course, reduced total lever-pressing over the course of 30 min does not necessarily indicate that lever-pressing was unaffected during PRC testing. It is possible that Gi- and Gq-transfected animals may have shown a different temporal pattern of lever-pressing behavior, despite showing a similar number of total presses. Likewise, it is possible that CNO did affect responding during PR testing, by altering the time course of presses rather than total number of presses. We therefore assessed the time course of lever-pressing in 5 min time bins, in PR and PRC session types, in Gi and Gq DREADDs, following CNO and VEH injections (Fig. 4.3.1.3).
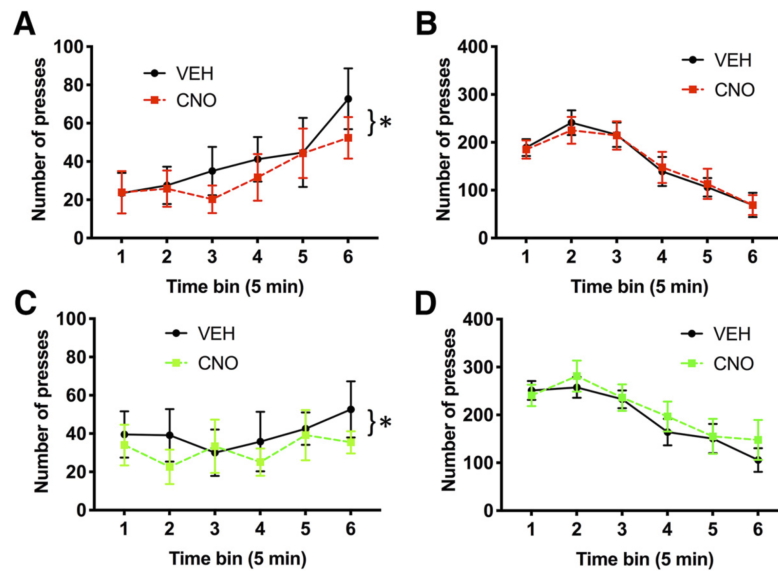
Figure 4.3.1.3. Time course of lever-pressing in different session types. Mean lever-pressing across 5 min time bins. **A**, Lever- pressing during PRC sessions, when rats were presented with both sucrose pellet and chow options in the Gi condition, in rats receiving CNO compared with within-subject VEH. **B**, Lever-pressing during PR sessions, when rats were presented with a single option in the Gi condition, in rats receiving CNO compared with VEH. **C**, Lever-pressing in PRC sessions, when rats were presented with both options in the Gq condition, in rats receiving CNO compared with VEH. **D**, Lever-pressing during PR sessions, when rats were presented with a single option in the Gq condition, in rats receiving CNO compared with VEH. Error bars indicate SEM. *p , 0.05.

As above, we first conducted a mixed ANOVA to test for group differences in temporal pressing patterns between the Gi- and Gq-DREADDs groups. Two separate mixed ANOVAs with virus as a between-subject factor, and injection and time bin as within-subject factors, were conducted on PRC and PR data. We were unable to include the GFP group here because these data were lost due to hardware failure. Virus groups did not differ in the timecourse of lever-pressing during PRC testing. A mixed ANOVA did not yield a significant main effect of virus on PRC pressing ($F_{(1,20)}=0.01$, p= 0.93). Responding increased across PRC sessions as revealed by a main effect of time bin ($F_{(5,100)}=3.17$, p=0.01), and CNO generally suppressed lever-pressing as revealed by a main effect of CNO ($F_{(1,20)}=14.30$, p= 0.001). There was no significant interaction between virus x injection ($F_{(1,20)}= 0.02$, p=0.88), virus x bin ($F_{(5,100)}=0.98$, p=0.43), or virus injection x bin ($F_{(5,100)}=0.72$, p= 0.61). Virus groups also did

not differ in the time course of lever-pressing during PR testing. A mixed ANOVA did not yield a significant main effect of virus on PR pressing ($F_{(1,20)}=2.11, p= 0.16$). Responding changed over the course of PR sessions as revealed by a main effect of time bin ($F_{(5,100)}= 32.729$, $p<0.0001$).In contrast to PRC testing, CNOhad no effect on the pattern of PR lever-pressing: there was no significant main effect of CNO ($F_{(1,20)}=0.84, p= 0.37$). There was no significant interaction between virus injection ($F_{(1,20)}=1.08, p=0.31$), virus x bin ($F_{(5,100)}=0.51, p=0.64$),or virus injection x bin ($F_{(5,100)}=0.42, p=0.83$) during PR testing.

4.3.2 *In vivo* calcium imaging

To further investigate why DREADD manipulations in ACC exerted their effects only in the choice condition, but not when PR lever-pressing was the only food option, we performed in vivo calcium imaging experiments to track responses of individual ACC cells and compare their activity during PR versus PRC sessions. Imaging rats were also given "satiety control" (CON) sessions, where rats were pre-fed with chow in the operant chamber, and then were allowed to lever press on a PR schedule in the absence of chow. This was to control for the possibility that neural encoding could be influenced by satiety from chow consumption, regardless of whether chow was freely available during lever-pressing. Behavior during imaging sessions was similar to behavior in VEH groups from the chemogenetics experiments (Fig. 4.3.2.1H,I), with the highest levels of responding occurring during the early portion of PR sessions (tapering off later in PR sessions), and steady low rates of responding throughout PRC sessions. A mixed ANOVA with experiment group (GCaMP, DREADDs) as a between-subject factor and session type (PR, PRC) and time bin (5 min) as within-subject factors revealed a significant main effect of time bin ($F_{(5,125)} = 5.27, p = 0.0002$). Not surprisingly, overall response rates were lower in the imaging group than in the VEH groups, as revealed by a significant main effect of experiment group

(F(1,113) = 21.04, p , 0.0001) (Fig. 4.3.2.1H). This is due to rats wearing the miniscope and being tethered by the coaxial cable, which inhibited pressing behavior.

But the effect of time on lever-pressing behavior across PR andPRC sessions did not depend on the experiment group; there was no significant interaction between time bin x experiment group (F(5,113)=1.10,p= 0.37). A one way repeated-measures ANOVA was used to test for differences in the total number of leverpresses, averaged across all imaging sessions, in the 4 rats included in our calcium analyses, during PR, PRC, and CON sessions. As expected, session type did affect the total number of presses as revealed by a significant main effect of session type (F(2,6) = 9.13, p = 0.02). Post hoc comparisons using Tukey's correction for familywise error revealed that the total number of presses was lower during PRC than PR sessions (p = 0.04) as well as CON sessions (p = 0.017). There was no significant difference between PR and CON sessions (p = 0.79). Imaging rats showed reduced pressing during PRC sessions, much like VEH rats (Fig. 4.3.2.1I).
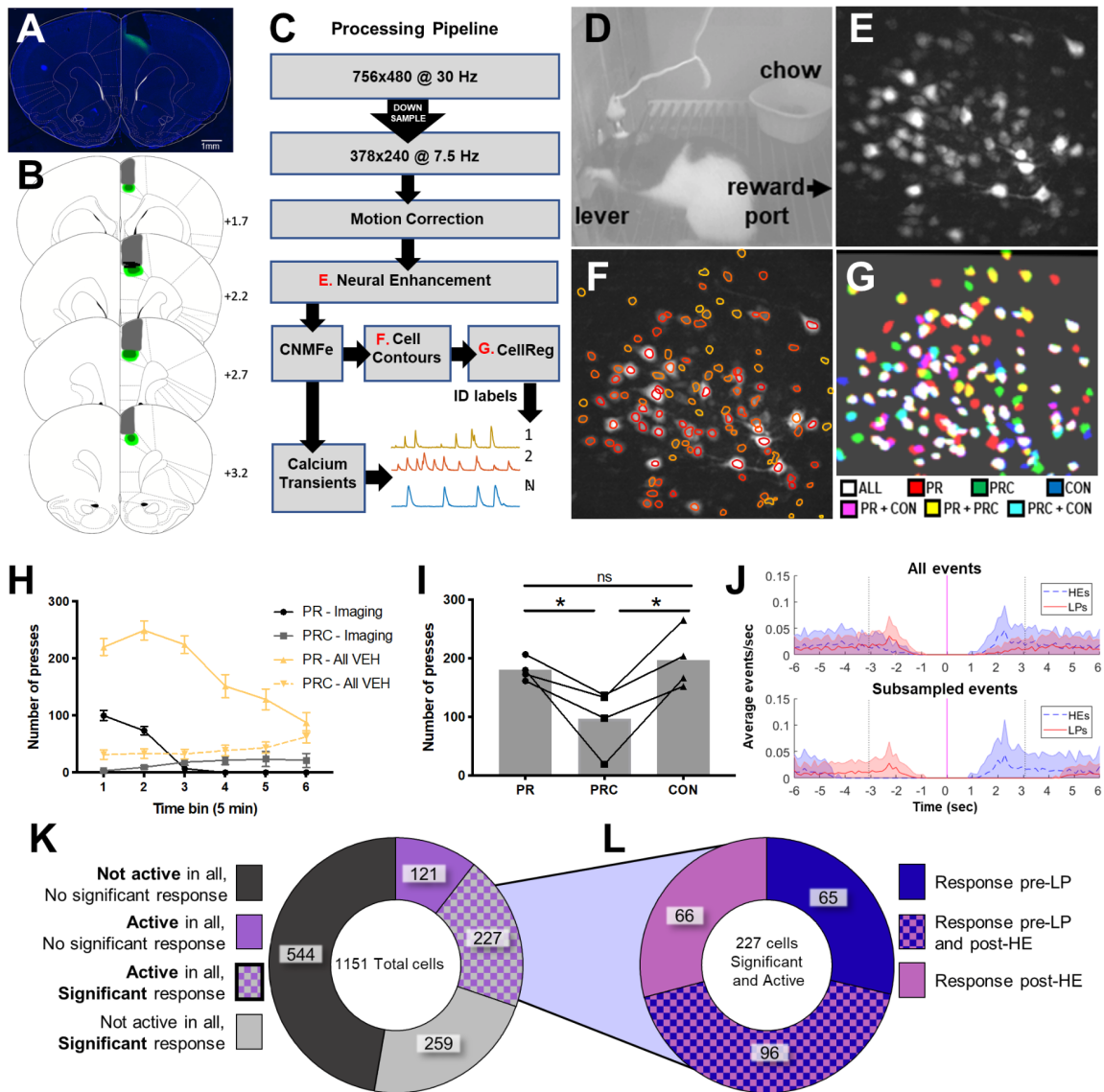
Figure 4.3.2.1. Calcium imaging during lever-pressing. **A**, Representative photomicrograph showing GCaMP6f expression and aspiration site for lens placement for ACC imaging. **B**, Schematic reconstruction of maximum (light green), minimum (dark green) viral spread, and maximum aspiration damage (gray). Black bars represent ACC recording sites. Numerals indicate AP level relative to bregma. Scale bar, 1 mm. **C**, Flow diagram for calcium imaging analysis pipeline. **D**, Example of PRC behavior session with the miniscope on the rat's head, and both sucrose and chow options available; reward port is on the right just out of view; chow is located in ramekin. **E**, Maximum projection image from the session in D after motion correction and neural enhancement. F, Same as in E, now with extracted cell contours overlaid. **G**, Contours matched across three different recording sessions, each taken 6 d apart. **H**, Number of presses during 5 min bins, averaged across all VEH sessions (gold) in the DREADDs groups and imaging group (greyscale). Pressing was reduced overall in the imaging group, but PR and PRC pressing exhibited similar patterns across time. **I**, Average number of total presses per session type during imaging sessions in the imaging group. Choice reduced lever-pressing in the imaging group, as in the DREADDs groups. **J**, On average, most HE events closely followed LP events (top). We excluded HE events that did not follow LP events and LP events that were very closely preceded by HE events, to avoid signal contamination (bottom). **K**, Proportions of cells that were active or responsive to stimuli. Cells that were active in at least one session of each type (PR, PRC, and CON) and had a significant response to either LP or HE events were included in further analysis. **L**, Proportions of cells that were responsive to LP and HE events. *p , 0.05. ns, not significant.

4.3.2.1 Calcium imaging in rat ACC

A group of 4 rats received infusions of AAV9-CaMKIIa-GCaMP6f and was subsequently implanted with 1.8-mm-diameter 0.25 pitch GRIN lenses in area 24 of ACC (Fig. 4.3.2.1). Rats were then trained on lever-pressing and tested during PR and PRC sessions (identical to those described above for DREADD experiments), as well as CON sessions described above. We recorded a total of 1151 neurons from ACC from the 4 animals (136 from Rat 1, 567 from Rat 2, 254 from Rat 3, 194 from Rat 4). Each neuron's calcium events were extracted by deconvolving its denoised calcium trace (sampling rate = 7.5 Hz; see Materials and Methods). To analyze neural responses to LP and HE events, PETHs were generated by combining data from all sessions of a given type (PR, PRC, or CON) during which the cell exhibited at least one calcium event. Calcium event probabilities were computed in 133.33 ms time bins within 63 s of the trigger event (LP or HE). To analyze how neural activity varied with session type (PR, PRC, CON), we identified a subset of 227 neurons (20% of all recorded cells) that were as follows: (1) active during at least one session of each type (PR, PRC, and CON), and (2) significantly responsive to either LP or HE events (or both, see below for responsiveness criteria) in the session-averaged PETH for at least one of the three session types (Fig. 4.3.2.1G). Cells (n = 924) that did not meet these two criteria were excluded from further analyses.

4.3.2.2 Responses preceding LP bouts

We analyzed neural responses occurring before the onset of each bout of lever-pressing, under the assumption that this is a likely time window during which the decision to exert effort (i.e., press the lever) is made. The onset of an LP bout was defined as the first LP that occurred after a magazine head entry and was followed by a HE within 30 s after completion of the lever-press ratio trial. LP response PETHs were triggered only by these LP onset events, not by all LP events (Fig. 4.3.2.2A). A neuron was classified as LP-responsive if it

showed a significantly higher probability of generating calcium events compared with the baseline rate within that session (see Materials and Methods). Approximately 60% (96 of 161) of LP-responsive neurons were also responsive to magazine head entries (Fig. 4.3.2.1L), and these were included in the analyses of LP-responsive cells presented below. These cells (significantly responsive to LPs and HEs) were typically due to significant responding on separate sessions.

For every LP-responsive cell, three LP-triggered PETHs were generated (one for each session type: PR, PRC, CON; Fig. 4.3.2.2B). Each PETH plotted the mean calcium event rate per time bin, averaged over all sessions of a given type during which the cell was active. To normalize the response of each cell across session types, the bins of all three PETHs for the cell were divided by the maximum value observed in any bin from all three PETHs (Fig. 4.3.2.2A, bottom). A population-averaged LP response curve was computed by taking the mean of the normalized PETHs for each session type (Fig. 4.3.2.2C). To statistically compare the pre-LP responses of neurons in the population, we computed the mean normalized response 3 s before lever press bouts for LP-responsive cells (Fig. 4.3.2.2D). By this measure, it was found that pre-LP responses differed significantly in magnitude by session type (Friedman's nonparametric ANOVA: p = 2.90e-5). Post hoc comparisons revealed that the pre-LP response was significantly larger during PR and CON sessions compared with PRC sessions (Sign rank test: PR . PRC, p = 1.35e-05; PRC . CON, p = 0.0017), whereas PR and CON pre-LP responses were not significantly different after correcting for multiple comparisons (Sign rank test: PR = CON, p = 0.033). Hence, at the population level, ACC neurons were significantly less responsive before the onset of lever press bouts when the rat was offered the choice of free chow from the ramekin as an alternative to lever-pressing during PRC sessions, and this effect could not be accounted for by satiety. We next evaluated how significantly responding cells were distributed across the different session types, and found that 60% (100 of 161 cells) were only

responsive to LPs during one session type, which is not significantly different from what would be expected from a random allocation (expected: 102 of 161 cells; x^2 = 0.428, p = 0.52; Fig. 4.3.2.2E). However, we found that 21 cells were significantly responsive to LPs during all three session types, greater than would be expected from chance (expected: 8 of 161 cells; x^2 = 22.23, p , 0.0001).
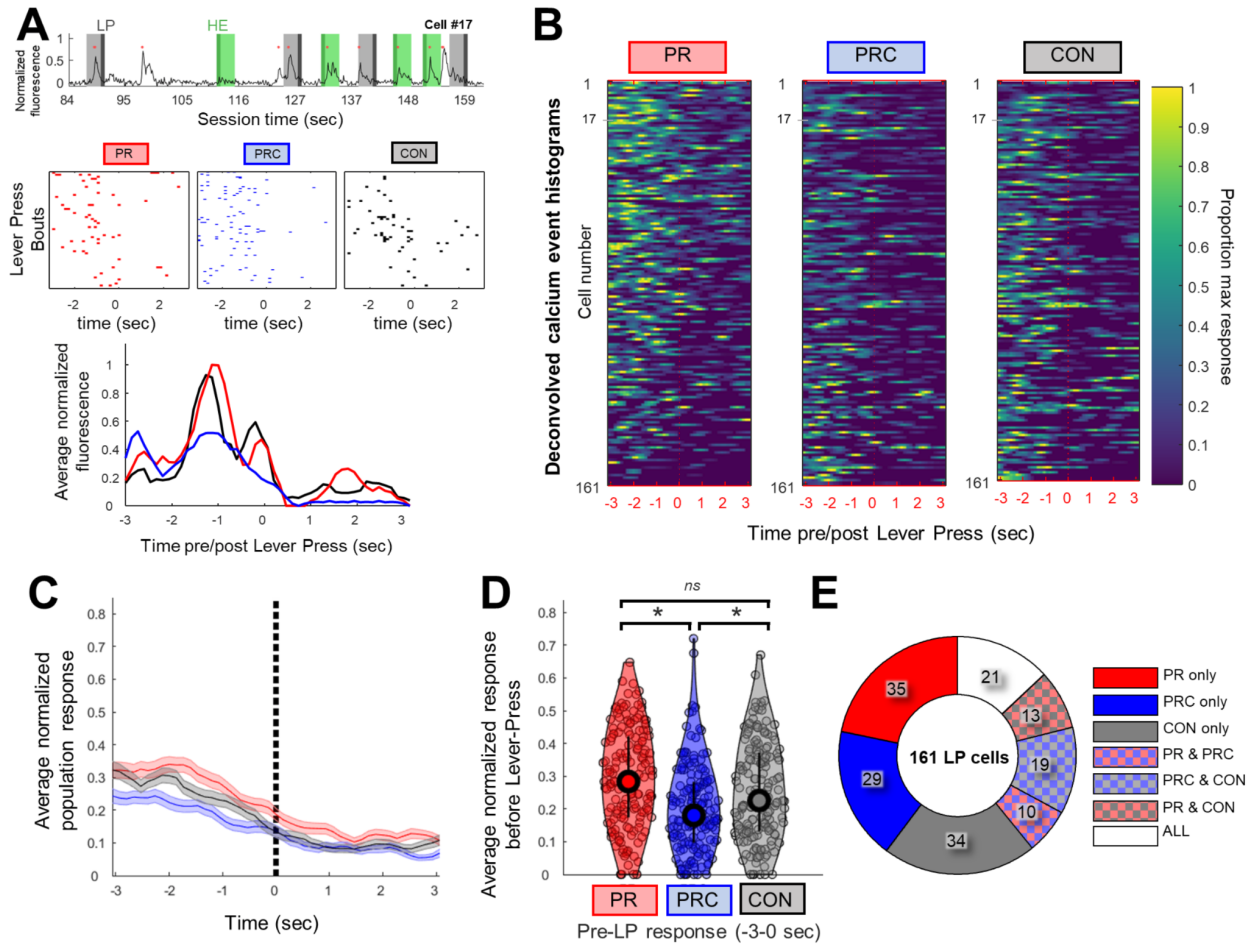
Figure 4.3.2.2. Neural responses in ACC before lever press bouts. **A**, Top, Example of raw fluorescence from an LP-responsive cell during a PR session. Light gray bands represent 3 s window before lever press bout begins. Dark gray represents the first lever press. Light green bands represent 3 s window after the first head entry following the lever press bout. Dark green represents the first head entry timestamp. Red dots indicate times at which deconvolved calcium transients occurred. Middle, Rastergrams of calcium events show that this cell often fired within ~3 s before lever presses during PR, PRC, and CON sessions. Bottom, Smoothed PETHs for this cell during each session type. **B**, Heat maps represent PETHs for all 161 cells that responded significantly before LP events. Color scale in each row is normalized to the maximum PETH bin value observed for the cell in that row across all three session types. **C**, Mean of PETHs for each session type in B. **D**, Mean normalized area under PETH curve for LP-responsive cells during the 3 s before LP events for PR, PRC, or CON sessions. **E**, Proportions of LP-responsive cells that were significantly responsive during all seven possible combinations of session types. Bars and shaded regions represent 6SEM. *p , 0.05. ns, Not significant after accounting for multiple comparisons.

We analyzed neural responses occurring immediately after magazine HE events, under the assumption that this is a likely time window during which signals encoding the value of the sucrose reward relative to the free alterative (chow) might be generated, as the reward is experienced (Fig. 4.3.2.3A). On average, most HE events followed LP bouts within several seconds (Fig. 4.3.2.1J, top). We focused our analyses on HE events that shortly followed LP bouts (Fig. 4.3.2.1J, bottom). A neuron was classified as HE-responsive if it exhibited a significantly higher probability of generating calcium events during the 3 s after HE compared with the baseline rate within that session (see Materials and Methods). Approximately 60% of HE-responsive neurons were also responsive to LP bout onset (Fig. 4.3.2.1L), and these were included in the analyses of HE-responsive cells presented below.

Three HE-triggered PETHs were generated for each cell (one for each session type: PR, PRC, CON), as well as an additional PETH triggered by head entries into the chow ramekin during PRC sessions (Fig. 4.3.2.3B). Head entries to the chow ramekin during CON sessions were not formally compared with sucrose HE. This was due to the fact that we sampled far fewer of these events compared with sucrose HE responses as shown in the individual data points in Figure 4.8D (right, plotted in purple). This also would not have been a fair comparison since these ramekin entries occurred before lever-pressing, during the time period that was excluded from analysis of HE responses. Nevertheless, on average, chow ramekin-evoked calcium responses were lower in magnitude than sucrose HE responses, during any of the session types (Fig. 4.3.2.3C,D, plotted in purple). Population-averaged responses to HE events were computed for each of the three session types (Fig. 4.3.2.3C), using the same methods described above for LP-triggered PETHs. It was found that post-HE responses differed significantly by session type (Friedman's nonparametric ANOVA: $p = 0.046$; Fig. 4.3.2.3D). Post hoc comparisons revealed that population responses during PR and CON sessions were not

significantly different from one another (Sign rank test: PR = CON, p = 0.32), whereas PRC sessions showed a significantly lower post-HE response than either of the other two session types (Sign rank test: PR > PRC, p = 0.0021; CON > PRC, p = 1.28e04). This pattern of results suggests that population-averaged responses of ACC neurons to rewarding outcomes were smaller in the presence of available alternative outcomes than when no alternative outcome was available, and this effect could not be explained by satiety. Additionally, we found that the distribution of significantly responding HE cells was different from for LP cells (Fig. 4.3.2.3E). More cells responded significantly to HEs in only a single session than would be expected from chance (80 of 162 cells, expected: 102 of 162; x^2 = 12.812, p = 0.0003), half of which (49%) were cells only responding during the CON sessions. Of the remaining population responding significantly in more than one session, 41 HE cells were responsive during all three session types, also greater than expected from chance (41 of 162 cells, expected: 9 of 162; x^2 = 120.47, p<0.00001).
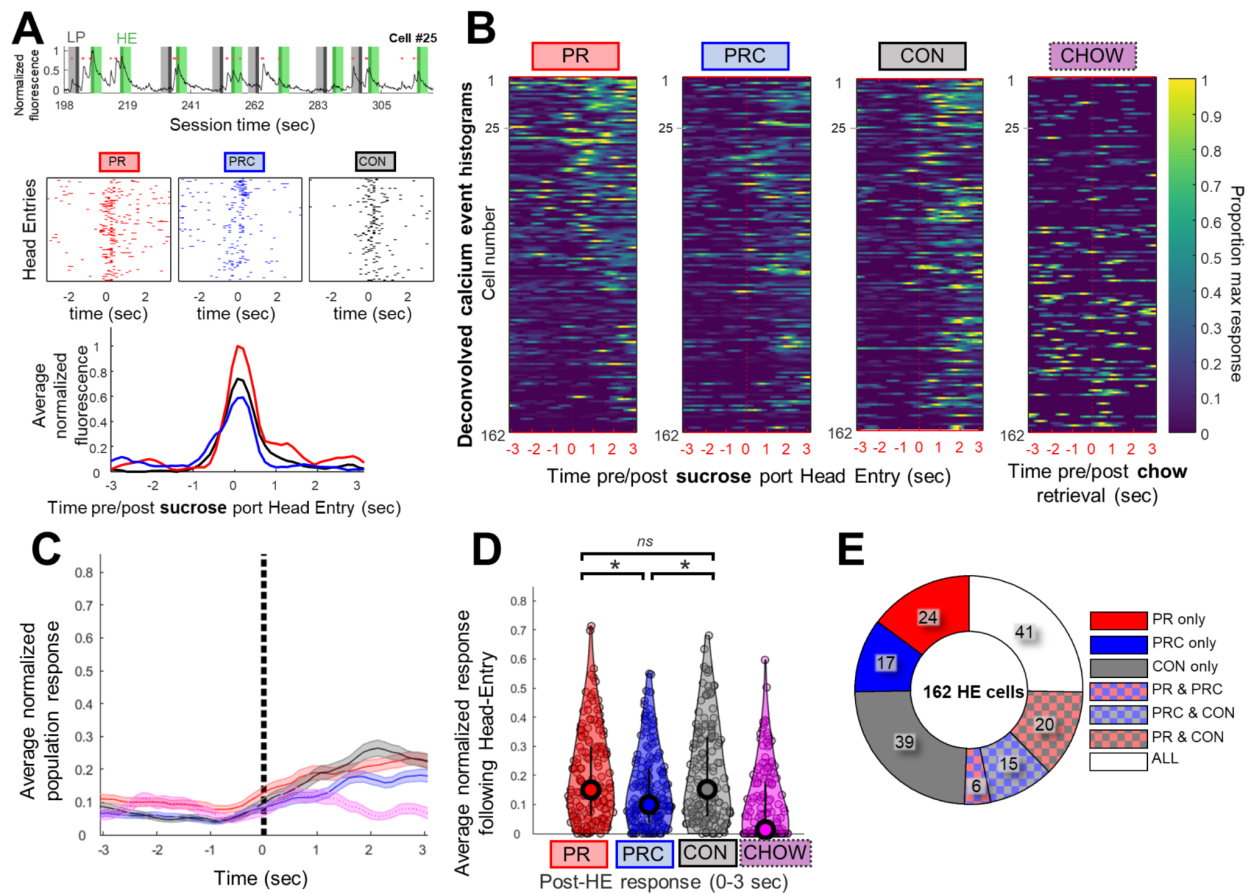
Figure 4.3.2.3. Neural responses in ACC following magazine head entry for sucrose reward. **A**, Top, Example of raw fluorescence from an HE-responsive cell during a PR session, plotted as in Figure 4.3.2.2A. Middle, Rastergram of calcium event times shows that this cell often fired just after HE events in PR, PRC, and CON sessions. Bottom, Smoothed PETHs for this cell during each session type. **B**, Heat maps represent PETHs for all 162 cells that responded significantly to HE events. For comparison, PETHs triggered by ramekin entries during PRC sessions are also shown (right). Color scale in each row is normalized to the maximum PETH bin value observed for the cell in that row across PR, PRC, and CON sessions. **C**, Mean of PETHs for each session type in B. Chow ramekin entries plotted in purple. **D**, Mean normalized area under PETH curve for HE-responsive cells during the 3 s following HE events for PR, PRC, or CON sessions. Head entry to chow ramekin plotted in purple (right). **E**, Proportions of HE-responsive cells that were significantly responsive during all seven possible combinations of session types. Bars and shaded regions represent +/-SEM. *p , 0.05. ns, Not significant after accounting for multiple comparisons.

4.4 DISCUSSION

We report that either chemogenetic silencing or stimulation of ACC excitatory neurons resulted in decreased effort for a qualitatively preferred option, and that this effect was only observed when a concurrently available, lower effort alternative was available, not when lever-pressing was the only response option. Chemogenetic manipulations had no effect on the ability to lever press for sucrose or on food preference. CNO administration also had no effect in rats lacking active DREADD (hM4D-Gi or hM3D-Gq) receptors. Slice electrophysiology confirmed robust inhibition (Stolyarova et al., 2019) and excitation in hM4D-Giand hM3D-Gq-transfected slices, respectively. Finally, using single-photon imaging, we found that ACC neurons showed differential task-evoked activity during lever-pressing and reward retrieval behavior that depended on the availability of another food option. In the same way that interference only affected choice lever-pressing, we found that tracked ACC neurons exhibited different response profiles during PR and PRC sessions. Together, these findings support a role for ACC in the evaluation of effortful behavior, consistent with recent evidence from single-unit recordings (Porter et al., 2019) and human fMRI (Arulpragasam et al., 2018).

4.4.1 ACC chemogenetic silencing

The earliest studies probing rat ACC in effort-based choice made use of T-maze tasks where rats selected between the same food option but of different magnitudes (Walton et al., 2002, 2003; Schweimer and Hauber, 2006). Investigations where rats chose between qualitatively different options following ACC lesions have yielded mixed results with reports of both null effects (Schweimer and Hauber, 2005) and decreased effort in the context of choice (Hart et al., 2017).

Here, hM3Dq and hM4Di receptors were expressed under a CaMKIIa promoter, putatively targeting primarily excitatory pyramidal neurons (Nathanson et al., 2009; Wang et al.,

2013), in contrast with prior studies using lesions or inactivations that silence all neural activity. ACC likely exerts its effects on choice behavior via projections to downstream targets, the densest of which are to dorsal striatum and mediodorsal thalamus (Vogt and Paxinos, 2014), although ACC also sends sparser efferents to ventral striatum and amygdala (Gabbott et al., 2005).

Though reliable, the magnitude of effect observed here with DREADDs was smaller than what we previously observed following lesions (Cohen's d = 1.39 lesions vs d = 0.28 Gi vs d = 0.29 Gq) (Hart et al., 2017), and also smaller than effects we have previously reported following pharmacological inactivation (Hart and Izquierdo, 2017) and drug exposure (Thompson et al., 2017; Hart et al., 2018). The smaller effect obtained with DREADDs could be due to different factors. First, DREADD receptors target only cells that recognize the CaMKIIa promoter (putative excitatory projection neurons). Second, although our slice experiments have shown that DREADD receptors modulate neural activity in ACC, these changes in neural activity may have weaker effects on behavior than complete pharmacological inactivation of ACC, or following chronic psychostimulant exposure (Hart et al., 2018). Nevertheless, the DREADD manipulations were enough to significantly bias behavior away from the preferred, effortful option during choice sessions.

4.4.2 ACC calcium imaging

ACC interference affected lever-pressing only during choice sessions. We used in vivo calcium imaging to observe how ACC neurons responded to lever-pressing and reward retrieval during such PR, PRC, and CON sessions. A total of 227 neurons from 4 rats were successfully recorded during at least one session of each type and had a significant response to lever-pressing or head entry. Over two-thirds of these neurons (161 of 227) were lever-press responsive in at least one of the three session types. Many of these cells (96 of 161 cells) were

also significantly responsive to head entries in other sessions, indicating some cells maintain encoding properties while others alter response characteristics during different sessions. Calcium trace activity during prelever responses was not significantly different in CON compared with PR sessions. However, calcium activity during the prelever period was lower during PRC than both PR and CON sessions, suggesting that free chow availability, not satiety from chow, attenuated prelever calcium activity.

More than two-thirds of recorded ACC neurons (162 of 227) were reward-responsive. These sucrose responses were similar in magnitude during CON and PR sessions, indicating that satiety from prior chow consumption had little effect on ACC responses to sucrose. By contrast, sucrose-related calcium activity was significantly lower during PRC sessions than during PR and CON sessions, demonstrating that, independently of satiety state, free chow availability attenuated sucrose responses of ACC neurons below the levels seen when sucrose was earned in the absence of free chow.

We next evaluated whether single-cell responses reflected the overall population average but found very few cells that individually responded accordingly in their PETHs (i.e., PR > PRC, CON > PRC, PRC = CON). This implies that the population signal that disambiguates effortful contexts is an emergent property of many cells functioning independently, rather than as a homogeneous population. This finding is not surprising given ACC's role in diverse behaviors and in line with recent single unit recordings within an effortful task demonstrating robust heterogeneity of response characteristics (Porter, Hillman, and Bilkey 2019). We further looked to see whether individual neurons were evenly distributed among condition types (PR, PRC, and CON). For both LP- and HE-responsive cells, we found that many cells responded significantly in all three session types. Therefore, while individual average responses do not reflect the same population profile, individual cells are preferentially active across similar contexts and serve to disambiguate relative reward value through coordinated population

activity. It has been theorized that such mixed selectivity in cortical regions is important in generating high dimensional representations for complex, adaptive behavior (Fusi, Miller, and Rigotti 2016). This type of heterogeneous population code would be more susceptible to perturbation by either bulk inhibition or excitation, as demonstrated in the results of our DREADD manipulations.

These findings converge on the idea that activity of ACC ensembles during sucrose consumption encodes the difference between the value of the sucrose versus the value of other available reward options. If no other options are available (as during PR and CON sessions), then the value of other options is zero, and thus nothing is subtracted from the value of the sucrose reward. But if a lower value reward option (e.g., lab chow during PRC sessions) is available while the rat is working for sucrose, then the nonzero value of the other option may be subtracted from the value of the sucrose reward, reducing the magnitude of ACC responses during sucrose delivery. If this relative value signal for sucrose in ACC is involved in driving motivated effort to work for sucrose, then it would be expected that the rat should exert less effort for sucrose under conditions where the ACC responses to sucrose are smaller. This is exactly what we observed: sucrose responses of ACC neurons were lower during PRC sessions (where lab chow was available as a competing reward option) than during PR or CON sessions (where sucrose was the only reward option).

In summary, neural activity associated with sucrose pellet collection in ACC is strongest when sucrose is the only available option, and weakened by the presence of the counterfactual choice (Blanchard and Hayden 2014; Mashhoori et al. 2018), or the value of leaving a patch in pursuit of another option (Hayden, Pearson, and Platt 2011). We add here the novel mechanism that ACC modulates this evaluation of options with a subpopulation of stable coding neurons, which we harnessed the power of calcium imaging to reliably track. Overall, ACC responses to lever-pressing and reward-retrieval were lower during PRC sessions; therefore, a plausible

explanation of our interference experiments would be that this lower, heterogeneous population activity is more susceptible to interference, thus explaining why CNO reduced lever-pressing selectively in PRC sessions.

4.4.3 ACC inhibition vs stimulation

If ACC activity encodes relative value signals that are involved in deriving an animal's motivation to exert effort, then it is natural to predict that disrupting ACC activity at the neural level would alter effort exertion at the behavioral level. We also expected that bidirectional manipulations of neural activity might yield bidirectional effects on motivated effort, such as manipulations of dopamine (Farrar et al. 2010; Nunes et al. 2013; Randall et al. 2014; Yohn, Thompson, et al. 2015; Yohn, Santerre, et al. 2015). Enhancing dopamine transmission with major psychostimulants (Yohn, Errante, et al. 2016), dopamine transporter blockers (Randall et al. 2015; Yohn, Santerre, et al. 2015), adenosine A2A receptor antagonists (Randall et al. 2012), or 5HT2C ligands (Bailey et al. 2016; Bailey et al. 2018) can increase effort output in otherwise untreated rats.

We applied a similar rationale for our Gq and Gi DREADD experiments and tested whether ACC chemogenetic inhibition versus stimulation yielded bidirectional effects on behavioral responding. This was not the case: lever-pressing behavior during PRC sessions was similarly attenuated by both Gq and Gi DREADDs. Indeed, the contributions of ACC and other frontocortical regions to effort may be more complex: pharmacological stimulation of orbitofrontal cortex decreases PR responding (Münster and Hauber 2017), and GABA antagonism of infralimbic cortex similarly decreases high-effort choice (Piantadosi et al. 2016). Therefore, in frontal cortex, there may be an optimal excitatory/inhibitory ratio for computing relative cost-benefit and, consequently, sending appropriate output to downstream targets. The results of ACC stimulation here are consistent with our manipulation introducing noise to

otherwise normal neural computations (Mainen and Sejnowski 1995; Stein, Gossen, and Jones 2005), thus impairing behavior in a manner similar to when neural activity is inhibited. Lever-pressing rates and task-evoked activity levels in ACC were both lower during PRC sessions than PR or CON sessions. Consequently, disruptions in decision-making may occur via changes in signal-to-noise ratio in this region: either by decreases in the signal (i.e., Gi DREADDs) or by increases in background noise (i.e., Gq DREADDs).

In conclusion, our findings suggest that the role of ACC in effort-based choice may be to discriminate the utility of available choice options by providing a stable population code for the relative value of different reward options. A better understanding of ACC contributions to effort-based choice may yield insight into the mechanisms underlying motivational symptoms in depression (Nunes et al. 2013) and addictions (M. J. F. Robinson, Robinson, and Berridge 2013).

REFERENCES

Acharya, Lavanya, Zahra M. Aghajan, Cliff Vuong, Jason J. Moore, and Mayank R. Mehta. 2016. "Causal Influence of Visual Cues on Hippocampal Directional Selectivity." Cell 164 (1–2): 197–207. doi:10.1016/j.cell.2015.12.015.

Aghajan, Zahra M, Lavanya Acharya, Jason J Moore, Jesse D Cushman, Cliff Vuong, and Mayank R Mehta. 2015. "Impaired Spatial Selectivity and Intact Phase Precession in Two-Dimensional Virtual Reality." Nature Neuroscience 18 (1): 121–128. doi:10.1038/nn.3884.

Aghajan, Zahra M., Diane Villaroman, Sonja Hiller, Tyler J. Wishard, Uros Topalovic, Leonardo Christov-Moore, Nader Shaterian, et al. 2019. "Modulation of Human Intracranial Theta Oscillations during Freely Moving Spatial Navigation and Memory." BioRxiv, 738807. doi:10.1101/738807.

Aharoni, Daniel, and Tycho M. Hoogland. 2019. "Circuit Investigations With Open-Source Miniaturized Microscopes: Past, Present and Future." Frontiers in Cellular Neuroscience 13: 141. doi:10.3389/fncel.2019.00141.

Aharoni, Daniel, Baljit S. Khakh, Alcino J. Silva, and Peyman Golshani. 2019. "All the Light That We Can See: A New Era in Miniaturized Microscopy." Nature Methods 16 (1): 11–13. doi:10.1038/s41592-018-0266-x.

Akam, Thomas, Ines Rodrigues-Vaz, Ivo Marcelo, Xiangyu Zhang, Michael Pereira, Rodrigo Freire Oliveira, Peter Dayan, and Rui M. Costa. 2020. "Anterior Cingulate Cortex Represents Action-State Predictions and Causally Mediates Model-Based Reinforcement Learning in a Two-Step Decision Task." BioRxiv, 126292. doi:10.1101/126292.

Alex, Hill. 1893. "The Hippocampus." Philosophical Transactions of the Royal Society of London. B 184: 389. http://www.jstor.org/stable/91761.

Alexander, Georgia M., Sarah C. Rogan, Atheir I. Abbas, Blaine N. Armbruster, Ying Pei, John A. Allen, Randal J. Nonneman, et al. 2009. "Remote Control of Neuronal Activity in Transgenic Mice Expressing Evolved G Protein-Coupled Receptors." Neuron 63 (1): 27–39. doi:10.1016/j.neuron.2009.06.014.

Alvernhe, Alice, Etienne Save, and Bruno Poucet. 2011. "Local Remapping of Place Cell Firing in the Tolman Detour Task." European Journal of Neuroscience 33 (9): 1696–1705. doi:10.1111/j.1460-9568.2011.07653.x.

Anagnostaras, Stephan G., Stephen Maren, and Michael S. Fanselow. 1995. "Scopolamine Selectively Disrupts the Acquisition of Contextual Fear Conditioning in Rats." Neurobiology of Learning and Memory 64 (3): 191–194. doi:10.1006/nlme.1995.0001.

Anagnostaras, Stephan G, Stephen Maren, Jennifer R Sage, Stacy Goodrich, and Michael S Fanselow. 1999. "Scopolamine and Pavlovian Fear Conditioning in Rats: Dose-Effect Analysis." Neuropsychopharmacology 21 (6): 731–744. doi:10.1016/s0893-133x(99)00083-4.

Angelaki, Dora E., Julia Ng, Amada M. Abrego, Henry X. Cham, Eftihia K. Asprodini, J. David Dickman, and Jean Laurens. 2020. "A Gravity-Based Three-Dimensional Compass in the Mouse Brain." Nature Communications 11 (1): 1855. doi:10.1038/s41467-020-15566-5.

Armbruster, Blaine N., Xiang Li, Mark H. Pausch, Stefan Herlitze, and Bryan L. Roth. 2007. "Evolving the Lock to Fit the Key to Create a Family of G Protein-Coupled Receptors Potently Activated by an Inert Ligand." Proceedings of the National Academy of Sciences 104 (12): 5163–5168. doi:10.1073/pnas.0700293104.

Aronov, Dmitriy, Rhino Nevers, and David W. Tank. 2017. "Mapping of a Non-Spatial Dimension by the Hippocampal–Entorhinal Circuit." Nature 543 (7647): 719–722. doi:10.1038/nature21692.

Atri, Alireza, Seth Sherman, Kenneth A. Norman, Brenda A. Kirchhoff, Marlene M. Nicolas, Michael D. Greicius, Steven C. Cramer, Hans C. Breiter, Michael E. Hasselmo, and Chantal E. Stern. 2004. "Blockade of Central Cholinergic Receptors Impairs New Learning and Increases Proactive Interference in a Word Paired-Associate Memory Task." Behavioral Neuroscience 118 (1): 223–236. doi:10.1037/0735-7044.118.1.223.

Azab, Habiba, and Benjamin Y. Hayden. 2017. "Correlates of Decisional Dynamics in the Dorsal Anterior Cingulate Cortex." PLOS Biology 15 (11): e2003091. doi:10.1371/journal.pbio.2003091.

Bailey, Matthew R., Olivia Goldman, Estefanía P. Bello, Muhammad O. Chohan, Nuri Jeong, Vanessa Winiger, Eileen Chun, et al. 2018. "An Interaction between Serotonin Receptor Signaling and Dopamine Enhances Goal-Directed Vigor and Persistence in Mice." Journal of Neuroscience 38 (9): 2149–2162. doi:10.1523/jneurosci.2088-17.2018.

Bailey, Matthew R., Cait Williamson, Chris Mezias, Vanessa Winiger, Rae Silver, Peter D. Balsam, and Eleanor H. Simpson. 2016.

"The Effects of Pharmacological Modulation of the Serotonin 2C Receptor on Goal-Directed Behavior in Mice." Psychopharmacology 233 (4): 615–624. doi:10.1007/s00213-015-4135-3.

Barbera, Giovanni, Bo Liang, Lifeng Zhang, Charles R. Gerfen, Eugenio Culurciello, Rong Chen, Yun Li, and Da-Ting Lin. 2016. "Spatially Compact Neural Clusters in the Dorsal Striatum Encode Locomotion Relevant Information." Neuron 92 (1): 202–213. doi:10.1016/j.neuron.2016.08.037.

Barbera, Giovanni, Bo Liang, Lifeng Zhang, Yun Li, and Da-Ting Lin. 2019. "A Wireless MiniScope for Deep Brain Imaging in Freely Moving Mice." Journal of Neuroscience Methods 323: 56–60. doi:10.1016/j.jneumeth.2019.05.008.

Bass, Cher, Pyry Helkkula, Vincenzo De Paola, Claudia Clopath, and Anil Anthony Bharath. 2017. "Detection of Axonal Synapses in 3D Two-Photon Images." PLOS ONE 12 (9): e0183309. doi:10.1371/journal.pone.0183309.

Berger, TW, B Alger, and RF Thompson. 1976. "Neuronal Substrate of Classical Conditioning in the Hippocampus." Science 192 (4238): 483–485. doi:10.1126/science.1257783.

Bernacchia, Alberto, Hyojung Seo, Daeyeol Lee, and Xiao-Jing Wang. 2011. "A Reservoir of Time Constants for Memory Traces in Cortical Neurons." Nature Neuroscience 14 (3): 366–372. doi:10.1038/nn.2752.

Bir, Shyamal C, Sudheer Ambekar, Sunil Kukreja, and Anil Nanda. 2015. "Julius Caesar Arantius (Giulio Cesare Aranzi, 1530–1589) and the Hippocampus of the Human Brain: History behind the Discovery." Journal of Neurosurgery 122 (4): 971–975. doi:10.3171/2014.11.jns132402.

Blanchard, Tommy C., and Benjamin Y. Hayden. 2014. "Neurons in Dorsal Anterior Cingulate Cortex Signal Postdecisional Variables in a Foraging Task." The Journal of Neuroscience 34 (2): 646–655. doi:10.1523/jneurosci.3151-13.2014.

Blokland, Arjan, Wiel Honig, and Wijnand G. M. Raaijmakers. 1992. "Effects of Intra-Hippocampal Scopolamine Injections in a Repeated Spatial Acquisition Task in the Rat." Psychopharmacology 109 (3): 373–376. doi:10.1007/bf02245886.

Bollimunta, Anil, Samantha R. Santacruz, Ryan W. Eaton, Pei S. Xu, John H. Morrison, Karen A. Moxon, Jose M. Carmena, and Jonathan J. Nassi. 2021. "Head-Mounted Microendoscopic Calcium Imaging in Dorsal Premotor Cortex of Behaving Rhesus Macaque." Cell Reports 35 (11): 109239. doi:10.1016/j.celrep.2021.109239.

Bonhoeffer, Tobias, and Amiram Grinvald. 1991. "Iso-Orientation Domains in Cat Visual Cortex Are Arranged in Pinwheel-like Patterns." Nature 353 (6343): 429–431. doi:10.1038/353429a0.

Bradfield, Laura A., Beatrice K. Leung, Susan Boldt, Sophia Liang, and Bernard W. Balleine. 2020. "Goal-Directed Actions Transiently Depend on Dorsal Hippocampus." Nature Neuroscience 23 (10): 1194–1197. doi:10.1038/s41593-020-0693-8.

Brazhnik, Elena, Ramie Borgnis, Robert U. Muller, and Steven E. Fox. 2004. "The Effects on Place Cells of Local Scopolamine Dialysis Are Mimicked by a Mixture of Two Specific Muscarinic Antagonists." The Journal of Neuroscience 24 (42): 9313–9323. doi:10.1523/jneurosci.1618-04.2004.

Buccafusco, Jerry J., Sharon R. Letchworth, Merouane Bencherif, and Patrick M. Lippiello. 2005. "Long-Lasting Cognitive Improvement with Nicotinic Receptor Agonists: Mechanisms of Pharmacokinetic–Pharmacodynamic Discordance." Trends in Pharmacological Sciences 26 (7): 352–360. doi:10.1016/j.tips.2005.05.007.

Cai, Denise J., Daniel Aharoni, Tristan Shuman, Justin Shobe, Jeremy Biane, Weilin Song, Brandon Wei, et al. 2016. "A Shared Neural Ensemble Links Distinct Contextual Memories Encoded Close in Time." Nature 534 (7605): 115–118. doi:10.1038/nature17955.

Chen, Qian, Joseph Cichon, Wenting Wang, Li Qiu, Seok-Jin R. Lee, Nolan R. Campbell, Nicholas DeStefino, et al. 2012. "Imaging Neural Activity Using Thy1-GCaMP Transgenic Mice." Neuron 76 (2): 297–308. doi:10.1016/j.neuron.2012.07.011.

Chen, Tsai-Wen, Trevor J. Wardill, Yi Sun, Stefan R. Pulver, Sabine L. Renninger, Amy Baohan, Eric R. Schreiter, et al. 2013. "Ultrasensitive Fluorescent Proteins for Imaging Neuronal Activity." Nature 499 (7458): 295–300. doi:10.1038/nature12354.

Chen, Zhe, Garrett J Blair, Hugh T Blair, and Jason Cong. 2020. "BLINK: Bit-Sparse LSTM Inference Kernel Enabling Efficient Calcium Trace Extraction for Neurofeedback Devices." Edited by David Atienza Alonso, Qinru Qiu, Sherief Reda, and Yiran Chen. Proceedings of the ACM/IEEE International Symposium on Low Power Electronics and Design, 217–222. doi:10.1145/3370748.3406552.

Chen, Zhe, Hugh T Blair, and Jason Cong. 2019. "LANMC: LSTM-Assisted Non-Rigid Motion Correction on FPGA for Calcium Image Stabilization." Edited by Kia Bazargan and Stephen Neuendorffer. Proceedings of the 2019 ACM/SIGDA International Symposium on Field-Programmable Gate Arrays, 104–109. doi:10.1145/3289602.3293919.

Cohen, Neil J., and Larry R. Squire. 1980. "Preserved Learning and Retention of Pattern-Analyzing Skill in Amnesia: Dissociation of

109

Knowing How and Knowing That." Science 210 (4466): 207–210. doi:10.1126/science.7414331.

Cohen, Sarah J., and Robert W. Stackman. 2015. "Assessing Rodent Hippocampal Involvement in the Novel Object Recognition Task. A Review." Behavioural Brain Research 285: 105–117. doi:10.1016/j.bbr.2014.08.002.

Cousins, Michael S., and John D. Salamone. 1994. "Nucleus Accumbens Dopamine Depletions in Rats Affect Relative Response Allocation in a Novel Cost/Benefit Procedure." Pharmacology Biochemistry and Behavior 49 (1): 85–91. doi:10.1016/0091-3057(94)90460-x.

Cousins, M.S., A. Atherton, L. Turner, and J.D. Salamone. 1996. "Nucleus Accumbens Dopamine Depletions Alter Relative Response Allocation in a T-Maze Cost/Benefit Task." Behavioural Brain Research 74 (1–2): 189–197. doi:10.1016/0166-4328(95)00151-4.

Cowen, Stephen L, Glen A Davis, and Douglas A Nitz. 2012. "Anterior Cingulate Neurons in the Rat Map Anticipated Effort and Reward to Their Associated Action Sequences." Journal of Neurophysiology 107 (9): 2393–2407. doi:10.1152/jn.01012.2011.

Cressant, Arnaud, Robert U. Muller, and Bruno Poucet. 2002. "Remapping of Place Cell Firing Patterns after Maze Rotations." Experimental Brain Research 143 (4): 470–479. doi:10.1007/s00221-002-1013-0.

Dalmay, Tamas, Elisabeth Abs, Rogier B. Poorthuis, Jan Hartung, De-Lin Pu, Sebastian Onasch, Yave R. Lozano, et al. 2019. "A Critical Role for Neocortical Processing of Threat Memory." Neuron 104 (6): 1180-1194.e7. doi:10.1016/j.neuron.2019.09.025.

Dana, Hod, Yi Sun, Boaz Mohar, Brad K. Hulse, Aaron M. Kerlin, Jeremy P. Hasseman, Getahun Tsegaye, et al. 2019. "High-Performance Calcium Sensors for Imaging Activity in Neuronal Populations and Microcompartments." Nature Methods 16 (7): 649–657. doi:10.1038/s41592-019-0435-6.

Decker, Michael W., Thuy Tran, and James L. McGaugh. 1990. "A Comparison of the Effects of Scopolamine and Diazepam on Acquisition and Retention of Inhibitory Avoidance in Mice." Psychopharmacology 100 (4): 515–521. doi:10.1007/bf02244005.

Denk, W, JH Strickler, and WW Webb. 1990. "Two-Photon Laser Scanning Fluorescence Microscopy." Science 248 (4951): 73–76. doi:10.1126/science.2321027.

Denk, Winfried, and Karel Svoboda. 1997. "Photon Upmanship: Why Multiphoton Imaging Is More than a Gimmick." Neuron 18 (3): 351–357. doi:10.1016/s0896-6273(00)81237-4.

Deshmukh, Sachin S., and James J. Knierim. 2011. "Representation of Non-Spatial and Spatial Information in the Lateral Entorhinal Cortex." Frontiers in Behavioral Neuroscience 5: 69. doi:10.3389/fnbeh.2011.00069.

Dombeck, Daniel A, Christopher D Harvey, Lin Tian, Loren L Looger, and David W Tank. 2010. "Functional Imaging of Hippocampal Place Cells at Cellular Resolution during Virtual Navigation." Nature Neuroscience 13 (11): 1433–1440. doi:10.1038/nn.2648.

Douchamps, Vincent, Ali Jeewajee, Pam Blundell, Neil Burgess, and Colin Lever. 2013. "Evidence for Encoding versus Retrieval Scheduling in the Hippocampus by Theta Phase and Acetylcholine." The Journal of Neuroscience 33 (20): 8689–8704. doi:10.1523/jneurosci.4483-12.2013.

Dupret, David, Joseph O'Neill, Barty Pleydell-Bouverie, and Jozsef Csicsvari. 2010. "The Reorganization and Reactivation of Hippocampal Maps Predict Spatial Memory Performance." Nature Neuroscience 13 (8): 995–1002. doi:10.1038/nn.2599.

Düring, Daniel N., Falk Dittrich, Mariana D. Rocha, Ryosuke O. Tachibana, Chihiro Mori, Kazuo Okanoya, Roman Boehringer, et al. 2020. "Fast Retrograde Access to Projection Neuron Circuits Underlying Vocal Learning in Songbirds." Cell Reports 33 (6): 108364. doi:10.1016/j.celrep.2020.108364.

Ebina, Teppei, Yoshito Masamizu, Yasuhiro R. Tanaka, Akiya Watakabe, Reiko Hirakawa, Yuka Hirayama, Riichiro Hira, et al. 2018. "Two-Photon Imaging of Neuronal Activity in Motor Cortex of Marmosets during Upper-Limb Movement Tasks." Nature Communications 9 (1): 1879. doi:10.1038/s41467-018-04286-6.

Echeverria, Valentina, and Ross Zeitlin. 2012. "Cotinine: A Potential New Therapeutic Agent against Alzheimer's Disease." CNS Neuroscience & Therapeutics 18 (7): 517–523. doi:10.1111/j.1755-5949.2012.00317.x.

Everitt, Barry J., and Trevor W. Robbins. 1997. "Central Cholinergic Systems and Cognition." Annual Review of Psychology 48 (1): 649–684. doi:10.1146/annurev.psych.48.1.649.

Fanselow, Michael S., and Kate M. Wassum. 2016. "The Origins and Organization of Vertebrate Pavlovian Conditioning." Cold Spring Harbor Perspectives in Biology 8 (1): a021717. doi:10.1101/cshperspect.a021717.

Farrar, A.M., K.N. Segovia, P.A. Randall, E.J. Nunes, L.E. Collins, C.M. Stopper, R.G. Port, et al. 2010. "Nucleus Accumbens and Effort-Related Functions: Behavioral and Neural Markers of the Interactions between Adenosine A2A and Dopamine D2 Receptors." Neuroscience 166 (4): 1056–1067. doi:10.1016/j.neuroscience.2009.12.056.

Floresco, Stan B., and Sarvin Ghods-Sharifi. 2007. "Amygdala-Prefrontal Cortical Circuitry Regulates Effort-Based Decision Making." Cerebral Cortex 17 (2): 251–260. doi:10.1093/cercor/bhj143.

Fortin, Norbert J., Sean P. Wright, and Howard Eichenbaum. 2004. "Recollection-like Memory Retrieval in Rats Is Dependent on the Hippocampus." Nature 431 (7005): 188–191. doi:10.1038/nature02853.

Frank, Loren M., Garrett B. Stanley, and Emery N. Brown. 2004. "Hippocampal Plasticity across Multiple Days of Exposure to Novel Environments." The Journal of Neuroscience 24 (35): 7681–7689. doi:10.1523/jneurosci.1958-04.2004.

Friedrich, Johannes, Weijian Yang, Daniel Soudry, Yu Mu, Misha B. Ahrens, Rafael Yuste, Darcy S. Peterka, and Liam Paninski. 2017. "Multi-Scale Approaches for High-Speed Imaging and Analysis of Large Neural Populations." PLOS Computational Biology 13 (8): e1005685. doi:10.1371/journal.pcbi.1005685.

Friedrich, Johannes, Pengcheng Zhou, and Liam Paninski. 2017. "Fast Online Deconvolution of Calcium Imaging Data." PLOS Computational Biology 13 (3): e1005423. doi:10.1371/journal.pcbi.1005423.

Fusi, Stefano, Earl K Miller, and Mattia Rigotti. 2016. "Why Neurons Mix: High Dimensionality for Higher Cognition." Current Opinion in Neurobiology 37: 66–74. doi:10.1016/j.conb.2016.01.010.

Gauthier, Jeffrey L., and David W. Tank. 2018. "A Dedicated Population for Reward Coding in the Hippocampus." Neuron 99 (1): 179-193.e7. doi:10.1016/j.neuron.2018.06.008.

Geiller, Tristan, Mohammad Fattahi, June-Seek Choi, and Sébastien Royer. 2017. "Place Cells Are More Strongly Tied to Landmarks in Deep than in Superficial CA1." Nature Communications 8 (1): 14531. doi:10.1038/ncomms14531.

Gerlei, Klara, Jessica Passlack, Ian Hawes, Brianna Vandrey, Holly Stevens, Ioannis Papastathopoulos, and Matthew F. Nolan. 2020. "Grid Cells Are Modulated by Local Head Direction." Nature Communications 11 (1): 4228. doi:10.1038/s41467-020-17500-1.

Ghods-Sharifi, Sarvin, and Stan B. Floresco. 2010. "Differential Effects on Effort Discounting Induced by Inactivations of the Nucleus Accumbens Core or Shell." Behavioral Neuroscience 124 (2): 179–191. doi:10.1037/a0018932.

Ghosh, Kunal K, Laurie D Burns, Eric D Cocker, Axel Nimmerjahn, Yaniv Ziv, Abbas El Gamal, and Mark J Schnitzer. 2011. "Miniaturized Integration of a Fluorescence Microscope." Nature Methods 8 (10): 871–878. doi:10.1038/nmeth.1694.

Giovannucci, Andrea, Johannes Friedrich, Pat Gunn, Jérémie Kalfon, Brandon L Brown, Sue Ann Koay, Jiannis Taxidis, et al. 2019. "CaImAn an Open Source Tool for Scalable Calcium Imaging Data Analysis." ELife 8: e38173. doi:10.7554/elife.38173.

Gonzalez, Walter G., Hanwen Zhang, Anna Harutyunyan, and Carlos Lois. 2019. "Persistence of Neuronal Representations through Time and Damage in the Hippocampus." Science 365 (6455): 821–825. doi:10.1126/science.aav9199.

Green, Amity, Kathryn A. Ellis, Julia Ellis, Cali F. Bartholomeusz, Susan Ilic, Rodney J. Croft, K. Luan Phan, and Pradeep J. Nathan. 2005. "Muscarinic and Nicotinic Receptor Modulation of Object and Spatial N-Back Working Memory in Humans." Pharmacology Biochemistry and Behavior 81 (3): 575–584. doi:10.1016/j.pbb.2005.04.010.

Grewe, Benjamin F., Jan Gründemann, Lacey J. Kitch, Jerome A. Lecoq, Jones G. Parker, Jesse D. Marshall, Margaret C. Larkin, et al. 2017. "Neural Ensemble Dynamics Underlying a Long-Term Associative Memory." Nature 543 (7647): 670–675. doi:10.1038/nature21682.

Groot, Andres de, Bastijn JG van den Boom, Romano M van Genderen, Joris Coppens, John van Veldhuijzen, Joop Bos, Hugo Hoedemaker, et al. 2020. "NINscope, a Versatile Miniscope for Multi-Region Circuit Investigations." ELife 9: e49987. doi:10.7554/elife.49987.

Gründemann, Jan, Yael Bitterman, Tingjia Lu, Sabine Krabbe, Benjamin F. Grewe, Mark J. Schnitzer, and Andreas Lüthi. 2019. "Amygdala Ensembles Encode Behavioral States." Science 364 (6437): eaav8736. doi:10.1126/science.aav8736.

Grutzendler, Jaime, and Wen-Biao Gan. 2006. "Two-Photon Imaging of Synaptic Plasticity and Pathology in the Living Mouse Brain." NeuroRX 3 (4): 489–496. doi:10.1016/j.nurx.2006.07.005.

Guzowski, John F., James J. Knierim, and Edvard I. Moser. 2004. "Ensemble Dynamics of Hippocampal Regions CA3 and CA1." Neuron 44 (4): 581–584. doi:10.1016/j.neuron.2004.11.003.

Han, Jin-Hee, Steven A. Kushner, Adelaide P. Yiu, Christy J. Cole, Anna Matynia, Robert A. Brown, Rachael L. Neve, John F. Guzowski, Alcino J. Silva, and Sheena A. Josselyn. 2007. "Neuronal Competition and Selection During Memory Formation." Science 316 (5823): 457–460. doi:10.1126/science.1139438.

Hart, Evan E., Garrett J. Blair, Thomas J. O'Dell, Hugh T. Blair, and Alicia Izquierdo. 2020. "Chemogenetic Modulation and Single-Photon Calcium Imaging in Anterior Cingulate Cortex Reveal a Mechanism for Effort-Based Decisions." Journal of Neuroscience 40 (29): JN-RM-2548-19. doi:10.1523/jneurosci.2548-19.2020.

Hart, Evan E., Julian O. Gerson, Yael Zoken, Marisella Garcia, and Alicia Izquierdo. 2017. "Anterior Cingulate Cortex Supports Effort Allocation towards a Qualitatively Preferred Option." European Journal of Neuroscience 46 (1): 1682–1688. doi:10.1111/ejn.13608.

Hart, Evan E., and Alicia Izquierdo. 2017. "Basolateral Amygdala Supports the Maintenance of Value and Effortful Choice of a Preferred Option." European Journal of Neuroscience 45 (3): 388–397. doi:10.1111/ejn.13497.

Harvey, Christopher D., Philip Coen, and David W. Tank. 2012. "Choice-Specific Sequences in Parietal Cortex during a Virtual-Navigation Decision Task." Nature 484 (7392): 62–68. doi:10.1038/nature10918.

Hasselmo, Michael E. 2006. "The Role of Acetylcholine in Learning and Memory." Current Opinion in Neurobiology 16 (6): 710–715. doi:10.1016/j.conb.2006.09.002.

Hasselmo, Michael E., and Jill McGaughy. 2004. "High Acetylcholine Levels Set Circuit Dynamics for Attention and Encoding and Low Acetylcholine Levels Set Dynamics for Consolidation." Progress in Brain Research 145: 207–231. doi:10.1016/s0079-6123(03)45015-2.

Hauber, Wolfgang, and Susanne Sommer. 2009. "Prefrontostriatal Circuitry Regulates Effort-Related Decision Making." Cerebral Cortex 19 (10): 2240–2247. doi:10.1093/cercor/bhn241.

Hayden, Benjamin Y., John M. Pearson, and Michael L. Platt. 2009. "Fictive Reward Signals in the Anterior Cingulate Cortex." Science 324 (5929): 948–950. doi:10.1126/science.1168488.

Hayden, Benjamin Y, John M Pearson, and Michael L Platt. 2011. "Neuronal Basis of Sequential Foraging Decisions in a Patchy Environment." Nature Neuroscience 14 (7): 933–939. doi:10.1038/nn.2856.

Heilbronner, Sarah R., and Benjamin Y. Hayden. 2015. "Dorsal Anterior Cingulate Cortex: A Bottom-Up View." Annual Review of Neuroscience 39 (1): 1–22. doi:10.1146/annurev-neuro-070815-013952.

Helmchen, Fritjof, Michale S. Fee, David W. Tank, and Winfried Denk. 2001. "A Miniature Head-Mounted Two-Photon Microscope High-Resolution Brain Imaging in Freely Moving Animals." Neuron 31 (6): 903–912. doi:10.1016/s0896-6273(01)00421-4.

Herrmann, Douglas J. 1982. "The Semantic-Episodic Distinction and the History of Long-Term Memory Typologies." Bulletin of the Psychonomic Society 20 (4): 207–210. doi:10.3758/bf03334817.

Herweg, Nora A., and Michael J. Kahana. 2018. "Spatial Representations in the Human Brain." Frontiers in Human Neuroscience 12: 297. doi:10.3389/fnhum.2018.00297.

Hill, A.J. 1978. "First Occurrence of Hippocampal Spatial Firing in a New Environment." Experimental Neurology 62 (2): 282–297. doi:10.1016/0014-4886(78)90058-4.

Hillman, Kristin L., and David K. Bilkey. 2010. "Neurons in the Rat Anterior Cingulate Cortex Dynamically Encode Cost–Benefit in a Spatial Decision-Making Task." The Journal of Neuroscience 30 (22): 7705–7713. doi:10.1523/jneurosci.1273-10.2010.

Hillman, Kristin L, and David K Bilkey. 2012. "Neural Encoding of Competitive Effort in the Anterior Cingulate Cortex." Nature Neuroscience 15 (9): 1290–1297. doi:10.1038/nn.3187.

Hosking, Jay G, Paul J Cocker, and Catharine A Winstanley. 2014. "Dissociable Contributions of Anterior Cingulate Cortex and Basolateral Amygdala on a Rodent Cost/Benefit Decision-Making Task of Cognitive Effort." Neuropsychopharmacology 39 (7): 1558–1567. doi:10.1038/npp.2014.27.

Huang, Zhen-Bo, Hao Wang, Xiu-Rong Rao, Gui-Fa Zhong, Wen-Hui Hu, and Guo-Qing Sheng. 2011. "Different Effects of Scopolamine on the Retrieval of Spatial Memory and Fear Memory." Behavioural Brain Research 221 (2): 604–609. doi:10.1016/j.bbr.2010.05.032.

Hunt, Laurence T., and Benjamin Y. Hayden. 2017. "A Distributed, Hierarchical and Recurrent Framework for Reward-Based Choice." Nature Reviews Neuroscience 18 (3): 172–182. doi:10.1038/nrn.2017.7.

Hyman, James Michael, Clay Brian Holroyd, and Jeremy Keith Seamans. 2017. "A Novel Neural Prediction Error Found in Anterior Cingulate Cortex Ensembles." Neuron 95 (2): 447-456.e3. doi:10.1016/j.neuron.2017.06.021.

Jacob, Alexander D., Adam I. Ramsaran, Andrew J. Mocle, Lina M. Tran, Chen Yan, Paul W. Frankland, and Sheena A Josselyn. 2018. "A Compact Head-Mounted Endoscope for in Vivo Calcium Imaging in Freely-Behaving Mice." BioRxiv, 252205. doi:10.1101/252205.

Jennings, Joshua H., Randall L. Ung, Shanna L. Resendez, Alice M. Stamatakis, Johnathon G. Taylor, Jonathan Huang, Katie Veleta, et al. 2015. "Visualizing Hypothalamic Network Dynamics for Appetitive and Consummatory Behaviors." Cell 160 (3): 516–527. doi:10.1016/j.cell.2014.12.026.

Jones, Matthew W, and Matthew A Wilson. 2005. "Theta Rhythms Coordinate Hippocampal–Prefrontal Interactions in a Spatial Memory Task." PLoS Biology 3 (12): e402. doi:10.1371/journal.pbio.0030402.

Josselyn, Sheena A., and Susumu Tonegawa. 2020. "Memory Engrams: Recalling the Past and Imagining the Future." Science 367 (6473): eaaw4325. doi:10.1126/science.aaw4325.

Keller, Philipp J, Misha B Ahrens, and Jeremy Freeman. 2015. "Light-Sheet Imaging for Systems Neuroscience." Nature Methods 12 (1): 27–29. doi:10.1038/nmeth.3214.

Kennerley, Steven W, Timothy E J Behrens, and Jonathan D Wallis. 2011. "Double Dissociation of Value Computations in Orbitofrontal and Anterior Cingulate Neurons." Nature Neuroscience 14 (12): 1581–1589. doi:10.1038/nn.2961.

Kim, Eun Joo, Earnest S. Kim, Mijeong Park, Jeiwon Cho, and Jeansok J. Kim. 2012. "Amygdalar Stimulation Produces Alterations on Firing Properties of Hippocampal Place Cells." The Journal of Neuroscience 32 (33): 11424–11434. doi:10.1523/jneurosci.1108-12.2012.

Kim, Eun Joo, Mijeong Park, Mi-Seon Kong, Sang Geon Park, Jeiwon Cho, and Jeansok J. Kim. 2015. "Alterations of Hippocampal Place Cells in Foraging Rats Facing a 'Predatory' Threat." Current Biology 25 (10): 1362–1367. doi:10.1016/j.cub.2015.03.048.

Kim, JJ, and MS Fanselow. 1992. "Modality-Specific Retrograde Amnesia of Fear." Science 256 (5057): 675–677. doi:10.1126/science.1585183.

Kingsbury, Lyle, Shan Huang, Jun Wang, Ken Gu, Peyman Golshani, Ye Emily Wu, and Weizhe Hong. 2019. "Correlated Neural Activity and Encoding of Behavior across Brains of Socially Interacting Animals." Cell 178 (2): 429-446.e16. doi:10.1016/j.cell.2019.05.022.

Kinsky, Nathaniel R., William Mau, David W. Sullivan, Samuel J. Levy, Evan A. Ruesch, and Michael E. Hasselmo. 2020. "Trajectory-Modulated Hippocampal Neurons Persist throughout Memory-Guided Navigation." Nature Communications 11 (1): 2443. doi:10.1038/s41467-020-16226-4.

Kinsky, Nathaniel R., David W. Sullivan, William Mau, Michael E. Hasselmo, and Howard B. Eichenbaum. 2018. "Hippocampal Place Fields Maintain a Coherent and Flexible Map across Long Timescales." Current Biology 28 (22): 3578-3588.e6. doi:10.1016/j.cub.2018.09.037.

Kondo, Takahiro, Risa Saito, Masaki Otaka, Kimika Yoshino-Saito, Akihiro Yamanaka, Tetsuo Yamamori, Akiya Watakabe, et al. 2018. "Calcium Transient Dynamics of Neural Ensembles in the Primary Motor Cortex of Naturally Behaving Monkeys." Cell Reports 24 (8): 2191-2195.e4. doi:10.1016/j.celrep.2018.07.057.

Kramis, R., C.H. Vanderwolf, and B.H. Bland. 1975. "Two Types of Hippocampal Rhythmical Slow Activity in Both the Rabbit and the Rat: Relations to Behavior and Effects of Atropine, Diethyl Ether, Urethane, and Pentobarbital." Experimental Neurology 49 (1): 58–85. doi:10.1016/0014-4886(75)90195-8.

Kropff, Emilio, James E. Carmichael, May-Britt Moser, and Edvard I. Moser. 2015. "Speed Cells in the Medial Entorhinal Cortex." Nature 523 (7561): 419–424. doi:10.1038/nature14622.

Lapish, Christopher C., Daniel Durstewitz, L. Judson Chandler, and Jeremy K. Seamans. 2008. "Successful Choice Behavior Is Associated with Distinct and Coherent Network States in Anterior Cingulate Cortex." Proceedings of the National Academy of Sciences 105 (33): 11963–11968. doi:10.1073/pnas.0804045105.

Leutgeb, Jill K., Stefan Leutgeb, Alessandro Treves, Retsina Meyer, Carol A. Barnes, Bruce L. McNaughton, May-Britt Moser, and Edvard I. Moser. 2005. "Progressive Transformation of Hippocampal Neuronal Representations in 'Morphed' Environments." Neuron 48 (2): 345–358. doi:10.1016/j.neuron.2005.09.007.

Leutgeb, Stefan, Jill K. Leutgeb, Carol A. Barnes, Edvard I. Moser, Bruce L. McNaughton, and May-Britt Moser. 2005. "Independent Codes for Spatial and Episodic Memory in Hippocampal Neuronal Ensembles." Science 309 (5734): 619–623. doi:10.1126/science.1114037.

Lever, Colin, Tom Wills, Francesca Cacucci, Neil Burgess, and John O'Keefe. 2002. "Long-Term Plasticity in Hippocampal Place-Cell Representation of Environmental Geometry." Nature 416 (6876): 90–94. doi:10.1038/416090a.

Levin, Edward D., F. Joseph McClernon, and Amir H. Rezvani. 2006. "Nicotinic Effects on Cognitive Function: Behavioral Characterization, Pharmacological Specification, and Anatomic Localization." Psychopharmacology 184 (3–4): 523–539. doi:10.1007/s00213-005-0164-7.

Liang, Bo, Lifeng Zhang, Giovanni Barbera, Wenting Fang, Jing Zhang, Xiaochun Chen, Rong Chen, Yun Li, and Da-Ting Lin. 2018. "Distinct and Dynamic ON and OFF Neural Ensembles in the Prefrontal Cortex Code Social Exploration." Neuron 100 (3): 700-714.e9. doi:10.1016/j.neuron.2018.08.043.

Liberti, William A, L Nathan Perkins, Daniel P Leman, and Timothy J Gardner. 2017. "An Open Source, Wireless Capable Miniature Microscope System." Journal of Neural Engineering 14 (4): 045001. doi:10.1088/1741-2552/aa6806.

Liu, Xu, Steve Ramirez, Petti T. Pang, Corey B. Puryear, Arvind Govindarajan, Karl Deisseroth, and Susumu Tonegawa. 2012. "Optogenetic Stimulation of a Hippocampal Engram Activates Fear Memory Recall." Nature 484 (7394): 381–385. doi:10.1038/nature11028.

Ljungberg, T., P. Apicella, and W. Schultz. 1992. "Responses of Monkey Dopamine Neurons during Learning of Behavioral Reactions." Journal of Neurophysiology 67 (1): 145–163. doi:10.1152/jn.1992.67.1.145.

Lombardo, Sylvia, and Uwe Maskos. 2015. "Role of the Nicotinic Acetylcholine Receptor in Alzheimer's Disease Pathology and Treatment." Neuropharmacology 96 (Pt B): 255–262. doi:10.1016/j.neuropharm.2014.11.018.

Lu, Jinghao, Chunyuan Li, Jonnathan Singh-Alvarado, Zhe Charles Zhou, Flavio Fröhlich, Richard Mooney, and Fan Wang. 2018. "MIN1PIPE: A Miniscope 1-Photon-Based Calcium Imaging Signal Extraction Pipeline." Cell Reports 23 (12): 3673–3684. doi:10.1016/j.celrep.2018.05.062.

Lu, Rongwen, Yajie Liang, Guanghan Meng, Pengcheng Zhou, Karel Svoboda, Liam Paninski, and Na Ji. 2020. "Rapid Mesoscale Volumetric Imaging of Neural Activity with Synaptic Resolution." Nature Methods 17 (3): 291–294. doi:10.1038/s41592-020-0760-9.

Mainen, ZF, and TJ Sejnowski. 1995. "Reliability of Spike Timing in Neocortical Neurons." Science 268 (5216): 1503–1506. doi:10.1126/science.7770778.

Mankin, Emily A., Fraser T. Sparks, Begum Slayyeh, Robert J. Sutherland, Stefan Leutgeb, and Jill K. Leutgeb. 2012. "Neuronal Code for Extended Time in the Hippocampus." Proceedings of the National Academy of Sciences 109 (47): 19462–19467. doi:10.1073/pnas.1214107109.

Mashhoori, Ali, Saeedeh Hashemnia, Bruce L McNaughton, David R Euston, and Aaron J Gruber. 2018. "Rat Anterior Cingulate Cortex Recalls Features of Remote Reward Locations after Disfavoured Reinforcements." ELife 7: e29793. doi:10.7554/elife.29793.

Mau, William, Michael E Hasselmo, and Denise J Cai. 2020. "The Brain in Motion: How Ensemble Fluidity Drives Memory-Updating and Flexibility." ELife 9: e63550. doi:10.7554/elife.63550.

Mau, William, David W. Sullivan, Nathaniel R. Kinsky, Michael E. Hasselmo, Marc W. Howard, and Howard Eichenbaum. 2018. "The Same Hippocampal CA1 Population Simultaneously Codes Temporal Information over Multiple Timescales." Current Biology 28 (10): 1499-1508.e4. doi:10.1016/j.cub.2018.03.051.

Maurer, Sara V., and Christina L. Williams. 2017. "The Cholinergic System Modulates Memory and Hippocampal Plasticity via Its Interactions with Non-Neuronal Cells." Frontiers in Immunology 8: 1489. doi:10.3389/fimmu.2017.01489.

McDonald, Robert J., and Norman M. White. 2013. "A Triple Dissociation of Memory Systems: Hippocampus, Amygdala, and Dorsal Striatum." Behavioral Neuroscience 127 (6): 835–853. doi:10.1037/a0034883.

McNaughton, Bruce L., Carol A. Barnes, and John O'Keefe. 1983. "The Contributions of Position, Direction, and Velocity to Single Unit Activity in the Hippocampus of Freely-Moving Rats." Experimental Brain Research 52 (1): 41–49. doi:10.1007/bf00237147.

Miller, Kevin J, Matthew M Botvinick, and Carlos D Brody. 2017. "Dorsal Hippocampus Contributes to Model-Based Planning." Nature Neuroscience 20 (9): 1269–1276. doi:10.1038/nn.4613.

Miyawaki, Atsushi, Juan Llopis, Roger Heim, J. Michael McCaffery, Joseph A. Adams, Mitsuhiko Ikura, and Roger Y. Tsien. 1997. "Fluorescent Indicators for Ca2+based on Green Fluorescent Proteins and Calmodulin." Nature 388 (6645): 882–887. doi:10.1038/42264.

Moita, Marta A. P., Svetlana Rosis, Yu Zhou, Joseph E. LeDoux, and Hugh T. Blair. 2004. "Putting Fear in Its Place: Remapping of Hippocampal Place Cells during Fear Conditioning." The Journal of Neuroscience 24 (31): 7015–7023. doi:10.1523/jneurosci.5492-03.2004.

Moita, Marta A.P., Svetlana Rosis, Yu Zhou, Joseph E. LeDoux, and Hugh T. Blair. 2003. "Hippocampal Place Cells Acquire Location-Specific Responses to the Conditioned Stimulus during Auditory Fear Conditioning." Neuron 37 (3): 485–497. doi:10.1016/s0896-6273(03)00033-3.

Morris, Richard G. M., P. Garrud, J. N. P. Rawlins, and J. O'Keefe. 1982. "Place Navigation Impaired in Rats with Hippocampal Lesions." Nature 297 (5868): 681–683. doi:10.1038/297681a0.

Moser, May-Britt, David C. Rowland, and Edvard I. Moser. 2015. "Place Cells, Grid Cells, and Memory." Cold Spring Harbor Perspectives in Biology 7 (2): a021808. doi:10.1101/cshperspect.a021808.

Moyer, James R., Richard A. Deyo, and John F. Disterhoft. 1990. "Hippocampectomy Disrupts Trace Eye-Blink Conditioning in Rabbits." Behavioral Neuroscience 104 (2): 243–252. doi:10.1037/0735-7044.104.2.243.

Münster, Alexandra, and Wolfgang Hauber. 2017. "Medial Orbitofrontal Cortex Mediates Effort-Related Responding in Rats." Cerebral Cortex 28 (12): 4379–4389. doi:10.1093/cercor/bhx293.

Muto, Akira, Masamichi Ohkura, Tomoya Kotani, Shin-ichi Higashijima, Junichi Nakai, and Koichi Kawakami. 2011. "Genetic Visualization with an Improved GCaMP Calcium Indicator Reveals Spatiotemporal Activation of the Spinal Motor Neurons in Zebrafish." Proceedings of the National Academy of Sciences 108 (13): 5425–5430. doi:10.1073/pnas.1000887108.

Muzzio, Isabel A. 2018. "Spatial Instability: The Paradox of Place Cell Remapping." Current Biology 28 (22): R1306–R1307. doi:10.1016/j.cub.2018.10.010.

Newman, Ehren L., Jason R. Climer, and Michael E. Hasselmo. 2014. "Grid Cell Spatial Tuning Reduced Following Systemic Muscarinic Receptor Blockade." Hippocampus 24 (6): 643–655. doi:10.1002/hipo.22253.

Newman, Ehren L., Sarah Jo C. Venditto, Jason R. Climer, Elijah A. Petter, Shea N. Gillet, and Sam Levy. 2017. "Precise Spike Timing Dynamics of Hippocampal Place Cell Activity Sensitive to Cholinergic Disruption." Hippocampus 27 (10): 1069–1082. doi:10.1002/hipo.22753.

Newman, L. A., and P. E. Gold. 2016. "Attenuation in Rats of Impairments of Memory by Scopolamine, a Muscarinic Receptor Antagonist, by Mecamylamine, a Nicotinic Receptor Antagonist." Psychopharmacology 233 (5): 925–932. doi:10.1007/s00213-015-4174-9.

Nowend, K.L., M. Arizzi, B.B. Carlson, and J.D. Salamone. 2001. "D1 or D2 Antagonism in Nucleus Accumbens Core or Dorsomedial Shell Suppresses Lever Pressing for Food but Leads to Compensatory Increases in Chow Consumption." Pharmacology Biochemistry and Behavior 69 (3–4): 373–382. doi:10.1016/s0091-3057(01)00524-x.

Nunes, Eric J., Patrick A. Randall, Evan E. Hart, Charlotte Freeland, Samantha E. Yohn, Younis Baqi, Christa E. Müller, Laura López-Cruz, Mercè Correa, and John D. Salamone. 2013. "Effort-Related Motivational Effects of the VMAT-2 Inhibitor Tetrabenazine: Implications for Animal Models of the Motivational Symptoms of Depression." The Journal of Neuroscience 33 (49): 19120–19130. doi:10.1523/jneurosci.2730-13.2013.

Oakley, David A., and I.Steele Russell. 1972. "Neocortical Lesions and Pavlovian Conditioning." Physiology & Behavior 8 (5): 915–926. doi:10.1016/0031-9384(72)90305-8.

O'Keefe, J., and J. Dostrovsky. 1971. "The Hippocampus as a Spatial Map. Preliminary Evidence from Unit Activity in the Freely-Moving Rat." Brain Research 34 (1): 171–175. doi:10.1016/0006-8993(71)90358-1.

O'Keefe, John. 1976. "Place Units in the Hippocampus of the Freely Moving Rat." Experimental Neurology 51 (1): 78–109. doi:10.1016/0014-4886(76)90055-8.

O'Keefe, John, and Lynn Nadel. 1978. "The Hippocampus as a Cognitive Map." Oxford University Press.

Omer, David B., Shir R. Maimon, Liora Las, and Nachum Ulanovsky. 2018. "Social Place-Cells in the Bat Hippocampus." Science 359 (6372): 218–224. doi:10.1126/science.aao3474.

Orbach, HS, LB Cohen, and A Grinvald. 1985. "Optical Mapping of Electrical Activity in Rat Somatosensory and Visual Cortex." Journal of Neuroscience 5 (7): 1886–1895. doi:10.1523/jneurosci.05-07-01886.1985.

Ozbay, Baris N., Gregory L. Futia, Ming Ma, Victor M. Bright, Juliet T. Gopinath, Ethan G. Hughes, Diego Restrepo, and Emily A. Gibson. 2018. "Three Dimensional Two-Photon Brain Imaging in Freely Moving Mice Using a Miniature Fiber Coupled Microscope with Active Axial-Scanning." Scientific Reports 8 (1): 8108. doi:10.1038/s41598-018-26326-3.

Pastalkova, Eva, Vladimir Itskov, Asohan Amarasingham, and György Buzsáki. 2008. "Internally Generated Cell Assembly Sequences in the Rat Hippocampus." Science 321 (5894): 1322–1327. doi:10.1126/science.1159775.

Pei, Ying, Sarah C. Rogan, Feng Yan, and Bryan L. Roth. 2008. "Engineered GPCRs as Tools to Modulate Signal Transduction." Physiology 23 (6): 313–321. doi:10.1152/physiol.00025.2008.

Piantadosi, Patrick T., Shahin Khayambashi, Magdalen G. Schluter, Agnes Kutarna, and Stan B. Floresco. 2016. "Perturbations in Reward-Related Decision-Making Induced by Reduced Prefrontal Cortical GABA Transmission: Relevance for Psychiatric Disorders." Neuropharmacology 101: 279–290. doi:10.1016/j.neuropharm.2015.10.007.

Pnevmatikakis, Eftychios A., and Andrea Giovannucci. 2017. "NoRMCorre: An Online Algorithm for Piecewise Rigid Motion Correction of Calcium Imaging Data." Journal of Neuroscience Methods 291: 83–94. doi:10.1016/j.jneumeth.2017.07.031.

Pnevmatikakis, Eftychios A., Daniel Soudry, Yuanjun Gao, Timothy A. Machado, Josh Merel, David Pfau, Thomas Reardon, et al. 2016. "Simultaneous Denoising, Deconvolution, and Demixing of Calcium Imaging Data." Neuron 89 (2): 285–299. doi:10.1016/j.neuron.2015.11.037.

Porter, Blake S, Kristin L Hillman, and David K Bilkey. 2019. "Anterior Cingulate Cortex Encoding of Effortful Behavior." Journal of Neurophysiology 121 (2): 701–714. doi:10.1152/jn.00654.2018.

Preston, Alison R., and Howard Eichenbaum. 2013. "Interplay of Hippocampus and Prefrontal Cortex in Memory." Current Biology 23 (17): R764–R773. doi:10.1016/j.cub.2013.05.041.

Procyk, E., Y. L. Tanaka, and J. P. Joseph. 2000. "Anterior Cingulate Activity during Routine and Non-Routine Sequential Behaviors in Macaques." Nature Neuroscience 3 (5): 502–508. doi:10.1038/74880.

Ramirez, Steve, Xu Liu, Pei-Ann Lin, Junghyup Suh, Michele Pignatelli, Roger L. Redondo, Tomás J. Ryan, and Susumu Tonegawa. 2013. "Creating a False Memory in the Hippocampus." Science 341 (6144): 387–391. doi:10.1126/science.1239073.

Ramirez, Steve, Xu Liu, Christopher J. MacDonald, Anthony Moffa, Joanne Zhou, Roger L. Redondo, and Susumu Tonegawa. 2015. "Activating Positive Memory Engrams Suppresses Depression-like Behaviour." Nature 522 (7556): 335–339. doi:10.1038/nature14514.

Randall, Patrick A., Christie A. Lee, Eric J. Nunes, Samantha E. Yohn, Victoria Nowak, Bilal Khan, Priya Shah, et al. 2014. "The VMAT-2 Inhibitor Tetrabenazine Affects Effort-Related Decision Making in a Progressive Ratio/Chow Feeding Choice Task: Reversal with Antidepressant Drugs." PLoS ONE 9 (6): e99320. doi:10.1371/journal.pone.0099320.

Randall, Patrick A., Christie A. Lee, Samantha J. Podurgiel, Evan Hart, Samantha E. Yohn, Myles Jones, Margaret Rowland, Laura López-Cruz, Mercè Correa, and John D. Salamone. 2015. "Bupropion Increases Selection of High Effort Activity in Rats Tested on a Progressive Ratio/Chow Feeding Choice Procedure: Implications for Treatment of Effort-Related Motivational Symptoms." International Journal of Neuropsychopharmacology 18 (2): pyu017–pyu017. doi:10.1093/ijnp/pyu017.

Randall, Patrick A., Marta Pardo, Eric J. Nunes, Laura López Cruz, V. Kiran Vemuri, Alex Makriyannis, Younis Baqi, Christa E. Müller, Mercè Correa, and John D. Salamone. 2012. "Dopaminergic Modulation of Effort-Related Choice Behavior as Assessed by a Progressive Ratio Chow Feeding Choice Task: Pharmacological Studies and the Role of Individual Differences." PLoS ONE 7 (10): e47934. doi:10.1371/journal.pone.0047934.

Ravassard, Pascal, Ashley Kees, Bernard Willers, David Ho, Daniel Aharoni, Jesse Cushman, Zahra M. Aghajan, and Mayank R. Mehta. 2013. "Multisensory Control of Hippocampal Spatiotemporal Selectivity." Science 340 (6138): 1342–1346. doi:10.1126/science.1232655.

Redondo, Roger L., Joshua Kim, Autumn L. Arons, Steve Ramirez, Xu Liu, and Susumu Tonegawa. 2014. "Bidirectional Switch of the Valence Associated with a Hippocampal Contextual Memory Engram." Nature 513 (7518): 426–430. doi:10.1038/nature13725.

Richardson, Nicole R., and David C.S. Roberts. 1996. "Progressive Ratio Schedules in Drug Self-Administration Studies in Rats: A Method to Evaluate Reinforcing Efficacy." Journal of Neuroscience Methods 66 (1): 1–11. doi:10.1016/0165-0270(95)00153-0.

Robinson, Mike J.F., Terry E. Robinson, and Kent C. Berridge. 2013. "Incentive Salience Transition to Addiction." In Biological Research on Addiction, 391–399. Section II: Neuroscience. doi:10.1016/b978-0-12-398335-0.00039-x.

Robinson, Nick T.M., Lucie A.L. Descamps, Lloyd E. Russell, Moritz O. Buchholz, Brendan A. Bicknell, Georgy K. Antonov, Joanna Y.N. Lau, Rebecca Nutbrown, Christoph Schmidt-Hieber, and Michael Häusser. 2020. "Targeted Activation of Hippocampal Place Cells Drives Memory-Guided Spatial Behavior." Cell 183 (6): 1586-1599.e10. doi:10.1016/j.cell.2020.09.061.

Roth, Bryan L. 2016. "DREADDs for Neuroscientists." Neuron 89 (4): 683–694. doi:10.1016/j.neuron.2016.01.040.

Roy, Dheeraj S., Takashi Kitamura, Teruhiro Okuyama, Sachie K. Ogawa, Chen Sun, Yuichi Obata, Atsushi Yoshiki, and Susumu Tonegawa. 2017. "Distinct Neural Circuits for the Formation and Retrieval of Episodic Memories." Cell 170 (5): 1000-1012.e19. doi:10.1016/j.cell.2017.07.013.

Rubin, Alon, Liron Sheintuch, Noa Brande-Eilat, Or Pinchasof, Yoav Rechavi, Nitzan Geva, and Yaniv Ziv. 2019. "Revealing Neural Correlates of Behavior without Behavioral Measurements." Nature Communications 10 (1): 4745. doi:10.1038/s41467-019-12724-2.

Rynes, Mathew L., Daniel A. Surinach, Samantha Linn, Michael Laroque, Vijay Rajendran, Judith Dominguez, Orestes

Hadjistamoulou, et al. 2021. "Miniaturized Head-Mounted Microscope for Whole-Cortex Mesoscale Imaging in Freely Behaving Mice." Nature Methods 18 (4): 417–425. doi:10.1038/s41592-021-01104-8.

Salamone, J. D., M. Correa, A. Farrar, and S. M. Mingote. 2007. "Effort-Related Functions of Nucleus Accumbens Dopamine and Associated Forebrain Circuits." Psychopharmacology 191 (3): 461–482. doi:10.1007/s00213-006-0668-9.

Salamone, J. D., M. Correa, S. Mingote, and S. M. Weber. 2003. "Nucleus Accumbens Dopamine and the Regulation of Effort in Food-Seeking Behavior: Implications for Studies of Natural Motivation, Psychiatry, and Drug Abuse." Journal of Pharmacology and Experimental Therapeutics 305 (1): 1–8. doi:10.1124/jpet.102.035063.

Salamone, J. D., R. E. Steinpreis, L. D. McCullough, P. Smith, D. Grebel, and K. Mahan. 1991. "Haloperidol and Nucleus Accumbens Dopamine Depletion Suppress Lever Pressing for Food but Increase Free Food Consumption in a Novel Food Choice Procedure." Psychopharmacology 104 (4): 515–521. doi:10.1007/bf02245659.

Salamone, John D, Mercè Correa, Samantha E Yohn, Jen-Hau Yang, Matthew Somerville, Renee A Rotolo, and Rose E Presby. 2017. "Behavioral Activation, Effort-Based Choice, and Elasticity of Demand for Motivational Stimuli: Basic and Translational Neuroscience Approaches." Motivation Science 3 (3): 208–229. doi:10.1037/mot0000070.

Salamone, John D., Michael S. Cousins, and Sherri Bucher. 1994. "Anhedonia or Anergia? Effects of Haloperidol and Nucleus Accumbens Dopamine Depletion on Instrumental Response Selection in a T-Maze Cost/Benefit Procedure." Behavioural Brain Research 65 (2): 221–229. doi:10.1016/0166-4328(94)90108-2.

Sanders, Honi, Matthew A Wilson, and Samuel J Gershman. 2020. "Hippocampal Remapping as Hidden State Inference." ELife 9: e51140. doi:10.7554/elife.51140.

Sarel, Ayelet, Arseny Finkelstein, Liora Las, and Nachum Ulanovsky. 2017. "Vectorial Representation of Spatial Goals in the Hippocampus of Bats." Science 355 (6321): 176–180. doi:10.1126/science.aak9589.

Sargolini, Francesca, Marianne Fyhn, Torkel Hafting, Bruce L. McNaughton, Menno P. Witter, May-Britt Moser, and Edvard I. Moser. 2006. "Conjunctive Representation of Position, Direction, and Velocity in Entorhinal Cortex." Science 312 (5774): 758–762. doi:10.1126/science.1125572.

Saucier, Deborah, Eric L. Hargreaves, Francis Boon, C. H. Vanderwolf, and Donald Peter Cain. 1996. "Detailed Behavioral Analysis of Water Maze Acquisition Under Systemic NMDA or Muscarinic Antagonism: Nonspatial Pretraining Eliminates Spatial Learning Deficits." Behavioral Neuroscience 110 (1): 103–116. doi:10.1037/0735-7044.110.1.103.

Schmaltz, Leonard W., and John Theios. 1972. "Acquisition and Extinction of a Classically Conditioned Response in Hippocampectomized Rabbits (Oryctolagus Cuniculus)." Journal of Comparative and Physiological Psychology 79 (2): 328–333. doi:10.1037/h0032531.

Schuette, Peter J., Fernando M.C.V. Reis, Sandra Maesta-Pereira, Meghmik Chakerian, Anita Torossian, Garrett Blair, Weisheng Wang, et al. 2020. "Long-Term Characterization of Hippocampal Remapping during Contextual Fear Acquisition and Extinction." Journal of Neuroscience 40 (43): 8329–8342. doi:10.1523/jneurosci.1022-20.2020.

Schultz, Wolfram. 2016. "Dopamine Reward Prediction-Error Signalling: A Two-Component Response." Nature Reviews Neuroscience 17 (3): 183–195. doi:10.1038/nrn.2015.26.

Schweimer, Judith, and Wolfgang Hauber. 2005. "Involvement of the Rat Anterior Cingulate Cortex in Control of Instrumental Responses Guided by Reward Expectancy." Learning & Memory 12 (3): 334–342. doi:10.1101/lm.90605.

Scoville, William Beecher, and Brenda Milner. 1957. "LOSS OF RECENT MEMORY AFTER BILATERAL HIPPOCAMPAL LESIONS." Journal of Neurology, Neurosurgery & Psychiatry 20 (1): 11. doi:10.1136/jnnp.20.1.11.

Seo, Hyojung, and Daeyeol Lee. 2007. "Temporal Filtering of Reward Signals in the Dorsal Anterior Cingulate Cortex during a Mixed-Strategy Game." The Journal of Neuroscience 27 (31): 8366–8377. doi:10.1523/jneurosci.2369-07.2007.

Sheintuch, Liron, Alon Rubin, Noa Brande-Eilat, Nitzan Geva, Noa Sadeh, Or Pinchasof, and Yaniv Ziv. 2017. "Tracking the Same Neurons across Multiple Days in Ca2+ Imaging Data." Cell Reports 21 (4): 1102–1115. doi:10.1016/j.celrep.2017.10.013.

Shenhav, Amitai, Matthew M. Botvinick, and Jonathan D. Cohen. 2013. "The Expected Value of Control: An Integrative Theory of Anterior Cingulate Cortex Function." Neuron 79 (2): 217–240. doi:10.1016/j.neuron.2013.07.007.

Shidara, Munetaka, and Barry J. Richmond. 2002. "Anterior Cingulate: Single Neuronal Signals Related to Degree of Reward Expectancy." Science 296 (5573): 1709–1711. doi:10.1126/science.1069504.

Shim, Sun B., Se H. Lee, Kab R. Chae, Chuel K. Kim, Dae Y. Hwang, Byoung G. Kim, Seung W. Jee, et al. 2008. "Nicotine Leads to Improvements in Behavioral Impairment and an Increase in the Nicotine Acetylcholine Receptor in Transgenic Mice." Neurochemical Research 33 (9): 1783–1788. doi:10.1007/s11064-008-9629-5.

Shimohama, Shun, Takashi Taniguchi, Motohatsu Fujiwara, and Masakuni Kameyama. 1986. "Changes in Nicotinic and Muscarinic Cholinergic Receptors in Alzheimer‐Type Dementia." Journal of Neurochemistry 46 (1): 288–293. doi:10.1111/j.1471-4159.1986.tb12960.x.

Shuman, Tristan, Daniel Aharoni, Denise J. Cai, Christopher R. Lee, Spyridon Chavlis, Lucia Page-Harley, Lauren M. Vetere, et al. 2020. "Breakdown of Spatial Coding and Interneuron Synchronization in Epileptic Mice." Nature Neuroscience 23 (2): 229–238. doi:10.1038/s41593-019-0559-0.

Skaggs, William E., Bruce L. McNaughton, Katalin M. Gothard, and Etan J. Markus. 1993. "An Information-Theoretic Approach for Deciphering the Hippocampal Code." Advances in Neural Information Processing Systems.

Skocek, Oliver, Tobias Nöbauer, Lukas Weilguny, Francisca Martínez Traub, Chuying Naomi Xia, Maxim I. Molodtsov, Abhinav Grama, et al. 2018. "High-Speed Volumetric Imaging of Neuronal Activity in Freely Moving Rodents." Nature Methods 15 (6): 429–432. doi:10.1038/s41592-018-0008-0.

Smith, Kyle S., David J. Bucci, Bryan W. Luikart, and Stephen V. Mahler. 2016. "DREADDs: Use and Application in Behavioral Neuroscience." Behavioral Neuroscience 130 (2): 137–155. doi:10.1037/bne0000135.

Sofroniew, Nicholas James. 2017. "Q&A: The Brain under a Mesoscope: The Forest and the Trees." BMC Biology 15 (1): 82. doi:10.1186/s12915-017-0426-y.

Solari, Nicola, and Balázs Hangya. 2018. "Cholinergic Modulation of Spatial Learning, Memory and Navigation." European Journal of Neuroscience 48 (5): 2199–2230. doi:10.1111/ejn.14089.

Solstad, Trygve, Charlotte N. Boccara, Emilio Kropff, May-Britt Moser, and Edvard I. Moser. 2008. "Representation of Geometric Borders in the Entorhinal Cortex." Science 322 (5909): 1865–1868. doi:10.1126/science.1166466.

Soltesz, Ivan, and Attila Losonczy. 2018. "CA1 Pyramidal Cell Diversity Enabling Parallel Information Processing in the Hippocampus." Nature Neuroscience 21 (4): 484–493. doi:10.1038/s41593-018-0118-0.

Squire, Larry R. 1986. "Mechanisms of Memory." Science 232 (4758): 1612–1619. doi:10.1126/science.3086978.

Squire, Larry R., Craig E.L. Stark, and Robert E. Clark. 2004. "The Medial Temporal Lobe." Annual Review of Neuroscience 27 (1): 279–306. doi:10.1146/annurev.neuro.27.070203.144130.

Stein, Richard B., E. Roderich Gossen, and Kelvin E. Jones. 2005. "Neuronal Variability: Noise or Part of the Signal?" Nature Reviews Neuroscience 6 (5): 389–397. doi:10.1038/nrn1668.

Stirman, Jeffrey N, Ikuko T Smith, Michael W Kudenov, and Spencer L Smith. 2016. "Wide Field-of-View, Multi-Region, Two-Photon Imaging of Neuronal Activity in the Mammalian Brain." Nature Biotechnology 34 (8): 857–862. doi:10.1038/nbt.3594.

Stolyarova, A., M. Rakhshan, E. E. Hart, T. J. O'Dell, M. A. K. Peters, H. Lau, A. Soltani, and A. Izquierdo. 2019. "Contributions of Anterior Cingulate Cortex and Basolateral Amygdala to Decision Confidence and Learning under Uncertainty." Nature Communications 10 (1): 4704. doi:10.1038/s41467-019-12725-1.

Stosiek, Christoph, Olga Garaschuk, Knut Holthoff, and Arthur Konnerth. 2003. "In Vivo Two-Photon Calcium Imaging of Neuronal Networks." Proceedings of the National Academy of Sciences 100 (12): 7319–7324. doi:10.1073/pnas.1232232100.

Sun, Dechuan, Ranjith Rajasekharan Unnithan, and Chris French. 2021. "Scopolamine Impairs Spatial Information Recorded With 'Miniscope' Calcium Imaging in Hippocampal Place Cells." Frontiers in Neuroscience 15: 640350. doi:10.3389/fnins.2021.640350.

Sutherland, R.J., I.Q. Whishaw, and B. Kolb. 1983. "A Behavioural Analysis of Spatial Localization Following Electrolytic, Kainate- or Colchicine-Induced Damage to the Hippocampal Formation in the Rat." Behavioural Brain Research 7 (2): 133–153. doi:10.1016/0166-4328(83)90188-2.

Svoboda, Karel, Winfried Denk, David Kleinfeld, and David W. Tank. 1997. "In Vivo Dendritic Calcium Dynamics in Neocortical Pyramidal Neurons." Nature 385 (6612): 161–165. doi:10.1038/385161a0.

Tian, Lin, S Andrew Hires, Tianyi Mao, Daniel Huber, M Eugenia Chiappe, Sreekanth H Chalasani, Leopoldo Petreanu, et al. 2009. "Imaging Neural Activity in Worms, Flies and Mice with Improved GCaMP Calcium Indicators." Nature Methods 6 (12): 875–881. doi:10.1038/nmeth.1398.

Tolman, Edward C. 1948. "Cognitive Maps in Rats and Men." Psychological Review 55 (4): 189–208. doi:10.1037/h0061626.

Topalovic, Uros, Zahra M. Aghajan, Diane Villaroman, Sonja Hiller, Leonardo Christov-Moore, Tyler J. Wishard, Matthias Stangl, et al. 2020. "Wireless Programmable Recording and Stimulation of Deep Brain Activity in Freely Moving Humans." Neuron 108 (2): 322-334.e9. doi:10.1016/j.neuron.2020.08.021.

Tulving, Endel. 1972. "Episodic and Semantic Memory." In Organization of Memory, by Endel Tulving and Wayne Donaldson, edited by Endel Tulving and Wayne Donaldson, 381–402.

Voleti, Venkatakaushik, Kripa B. Patel, Wenze Li, Citlali Perez Campos, Srinidhi Bharadwaj, Hang Yu, Caitlin Ford, et al. 2019. "Real-Time Volumetric Microscopy of in Vivo Dynamics and Large-Scale Samples with SCAPE 2.0." Nature Methods 16 (10): 1054–1062. doi:10.1038/s41592-019-0579-4.

Vorhees, Charles V., and Michael T. Williams. 2014. "Assessing Spatial Learning and Memory in Rodents." ILAR Journal 55 (2): 310–332. doi:10.1093/ilar/ilu013.

Wallenstein, Gene V., and David R. Vago. 2001. "Intrahippocampal Scopolamine Impairs Both Acquisition and Consolidation of Contextual Fear Conditioning." Neurobiology of Learning and Memory 75 (3): 245–252. doi:10.1006/nlme.2001.4005.

Walton, Mark E., David M. Bannerman, Karin Alterescu, and Matthew F. S. Rushworth. 2003. "Functional Specialization within Medial Frontal Cortex of the Anterior Cingulate for Evaluating Effort-Related Decisions." Journal of Neuroscience 23 (16): 6475–6479. doi:10.1523/jneurosci.23-16-06475.2003.

Walton, Mark E., David M. Bannerman, and Matthew F. S. Rushworth. 2002. "The Role of Rat Medial Frontal Cortex in Effort-Based Decision Making." Journal of Neuroscience 22 (24): 10996–11003. doi:10.1523/jneurosci.22-24-10996.2002.

Wang, Cheng, Xiaojing Chen, and James J Knierim. 2020. "Egocentric and Allocentric Representations of Space in the Rodent Brain." Current Opinion in Neurobiology 60: 12–20. doi:10.1016/j.conb.2019.11.005.

Wang, Dong V., and Satoshi Ikemoto. 2016. "Coordinated Interaction between Hippocampal Sharp-Wave Ripples and Anterior Cingulate Unit Activity." Journal of Neuroscience 36 (41): 10663–10672. doi:10.1523/jneurosci.1042-16.2016.

Wang, Jing W., Allan M. Wong, Jorge Flores, Leslie B. Vosshall, and Richard Axel. 2003. "Two-Photon Calcium Imaging Reveals an Odor-Evoked Map of Activity in the Fly Brain." Cell 112 (2): 271–282. doi:10.1016/s0092-8674(03)00004-7.

Wang, Melissa E., Ellen G. Wann, Robin K. Yuan, Manuel M. Ramos Álvarez, Squire M. Stead, and Isabel A. Muzzio. 2012. "Long-Term Stabilization of Place Cell Remapping Produced by a Fearful Experience." The Journal of Neuroscience 32 (45): 15802–15814. doi:10.1523/jneurosci.0480-12.2012.

Wang, Melissa E., Robin K. Yuan, Alexander T. Keinath, Manuel M. Ramos Álvarez, and Isabel A. Muzzio. 2015. "Extinction of Learned Fear Induces Hippocampal Place Cell Remapping." The Journal of Neuroscience 35 (24): 9122–9136. doi:10.1523/jneurosci.4477-14.2015.

Weible, Aldis P., David C. Rowland, Caitlin K. Monaghan, Nicholas T. Wolfgang, and Clifford G. Kentros. 2012. "Neural Correlates of Long-Term Object Memory in the Mouse Anterior Cingulate Cortex." The Journal of Neuroscience 32 (16): 5598–5608. doi:10.1523/jneurosci.5265-11.2012.

Weiss, Craig, and John F. Disterhoft. 2015. "The Impact of Hippocampal Lesions on Trace-Eyeblink Conditioning and Forebrain–Cerebellar Interactions." Behavioral Neuroscience 129 (4): 512–522. doi:10.1037/bne0000061.

Wills, Tom J., Colin Lever, Francesca Cacucci, Neil Burgess, and John O'Keefe. 2005. "Attractor Dynamics in the Hippocampal Representation of the Local Environment." Science 308 (5723): 873–876. doi:10.1126/science.1108905.

Wilson, MA, and BL McNaughton. 1993. "Dynamics of the Hippocampal Ensemble Code for Space." Science 261 (5124): 1055–1058. doi:10.1126/science.8351520.

Wiltgen, Brian J., Matthew J. Sanders, Nicholas S. Behne, and Michael S. Fanselow. 2001. "Sex Differences, Context Preexposure, and the Immediate Shock Deficit in Pavlovian Context Conditioning With Mice." Behavioral Neuroscience 115 (1): 26–32. doi:10.1037/0735-7044.115.1.26.

Winocur, Gordon, J. N. P. Rawlins, and J. A. Gray. 1987. "The Hippocampus and Conditioning to Contextual Cues." Behavioral Neuroscience 101 (5): 617–625. doi:10.1037/0735-7044.101.5.617.

Winstanley, Catharine A., and Stan B. Floresco. 2016. "Deciphering Decision Making: Variation in Animal Models of Effort- and Uncertainty-Based Choice Reveals Distinct Neural Circuitries Underlying Core Cognitive Processes." Journal of Neuroscience 36 (48): 12069–12079. doi:10.1523/jneurosci.1713-16.2016.

Wirt, Ryan A., and James M. Hyman. 2019. "ACC Theta Improves Hippocampal Contextual Processing during Remote Recall." Cell Reports 27 (8): 2313-2327.e4. doi:10.1016/j.celrep.2019.04.080.

Yartsev, Michael M. 2013. "Space Bats: Multidimensional Spatial Representation in the Bat." Science 342 (6158): 573–574. doi:10.1126/science.1245809.

Yartsev, Michael M., and Nachum Ulanovsky. 2013. "Representation of Three-Dimensional Space in the Hippocampus of Flying Bats." Science 340 (6130): 367–372. doi:10.1126/science.1235338.

Yohn, Samantha E., Emily E. Errante, Aaron Rosenbloom-Snow, Matthew Somerville, Margaret Rowland, Kristin Tokarski, Nadia Zafar, Merce Correa, and John D. Salamone. 2016. "Blockade of Uptake for Dopamine, but Not Norepinephrine or 5-HT, Increases Selection of High Effort Instrumental Activity: Implications for Treatment of Effort-Related Motivational Symptoms in Psychopathology." Neuropharmacology 109: 270–280. doi:10.1016/j.neuropharm.2016.06.018.

Yohn, Samantha E., Augustyna Gogoj, Aileen Haque, Laura Lopez-Cruz, Allison Haley, Philip Huxley, Patricia Baskin, Merce Correa, and John D. Salamone. 2016. "Evaluation of the Effort-Related Motivational Effects of the Novel Dopamine Uptake Inhibitor PRX-14040." Pharmacology Biochemistry and Behavior 148: 84–91. doi:10.1016/j.pbb.2016.06.004.

Yohn, Samantha E., Laura Lopez-Cruz, Peter H. Hutson, Merce Correa, and John D. Salamone. 2016. "Effects of Lisdexamfetamine and S-Citalopram, Alone and in Combination, on Effort-Related Choice Behavior in the Rat." Psychopharmacology 233 (6): 949–960. doi:10.1007/s00213-015-4176-7.

Yohn, Samantha E., Jessica L. Santerre, Eric J. Nunes, Rouba Kozak, Samantha J. Podurgiel, Mercè Correa, and John D. Salamone. 2015. "The Role of Dopamine D1 Receptor Transmission in Effort-Related Choice Behavior: Effects of D1 Agonists." Pharmacology Biochemistry and Behavior 135: 217–226. doi:10.1016/j.pbb.2015.05.003.

Yohn, Samantha E., Christian Thompson, Patrick A. Randall, Christie A. Lee, Christa E. Müller, Younis Baqi, Mercè Correa, and John D. Salamone. 2015. "The VMAT-2 Inhibitor Tetrabenazine Alters Effort-Related Decision Making as Measured by the T-Maze Barrier Choice Task: Reversal with the Adenosine A2A Antagonist MSX-3 and the Catecholamine Uptake Blocker Bupropion." Psychopharmacology 232 (7): 1313–1323. doi:10.1007/s00213-014-3766-0.

Zhang, Yiyao, Liang Cao, Viktor Varga, Miao Jing, Mursel Karadas, Yulong Li, and György Buzsáki. 2021. "Cholinergic Suppression of Hippocampal Sharp-Wave Ripples Impairs Working Memory." Proceedings of the National Academy of Sciences 118 (15): e2016432118. doi:10.1073/pnas.2016432118.

Zhou, Pengcheng, Shanna L Resendez, Jose Rodriguez-Romaguera, Jessica C Jimenez, Shay Q Neufeld, Andrea Giovannucci, Johannes Friedrich, et al. 2018. "Efficient and Accurate Extraction of in Vivo Calcium Signals from Microendoscopic Video Data." ELife 7: e28728. doi:10.7554/elife.28728.

Ziv, Yaniv, Laurie D Burns, Eric D Cocker, Elizabeth O Hamel, Kunal K Ghosh, Lacey J Kitch, Abbas El Gamal, and Mark J Schnitzer. 2013. "Long-Term Dynamics of CA1 Hippocampal Place Codes." Nature Neuroscience 16 (3): 264–266. doi:10.1038/nn.3329.

Zong, Weijian, Runlong Wu, Mingli Li, Yanhui Hu, Yijun Li, Jinghang Li, Hao Rong, et al. 2017. "Fast High-Resolution Miniature Two-Photon Microscopy for Brain Imaging in Freely Behaving Mice." Nature Methods 14 (7): 713–719. doi:10.1038/nmeth.4305.